

Copyright

by

Leslie Ann Bruce

2017

**The Thesis Committee for Leslie Ann Bruce
Certifies that this is the approved version of the following thesis:**

**Effects of magma chamber processes on water and H₂O/Ce ratios in
HIMU magmas from the Cook-Austral Islands: New insights from
clinopyroxene phenocrysts**

**APPROVED BY
SUPERVISING COMMITTEE:**

Supervisor:

John C. Lassiter

Jaime D. Barnes

James E. Gardner

**Effects of magma chamber processes on water and H₂O/Ce ratios in
HIMU magmas from the Cook-Austral Islands: New insights from
clinopyroxene phenocrysts**

by

Leslie Ann Bruce

Thesis

Presented to the Faculty of the Graduate School of

The University of Texas at Austin

in Partial Fulfillment

of the Requirements

for the Degree of

Master of Science in Geological Sciences

The University of Texas at Austin

August 2017

Dedication

To shadow and L.C., my furry little girls. Over the past two years, you two were there for so many endless cuddles. How happy the two of you get when I walk through the front door made every hard day disappear. Although you're a dog and a cat, and obviously can't read, just know that you put the biggest smile on my face and I love you to the moon and back.

Acknowledgements

This thesis was made possible by many people and various funding sources. I would first like to thank the Jackson School of geosciences for four semesters of funding as a TA. I would like to also thank NSF for summer funding as an RA. I would like to thank my advisor, John Lassiter, and my committee members, Jaime Barnes and Jim Gardner, for all of their expertise and guidance with this project.

I would like to thank Ed Marshall for the tremendous amount of time and effort he dedicated to helping me with this project. Ed did so much for this project and was the pioneer behind our sample preparation methods. Ed also took charge of securing us matrix-matched standards for SIMS analyses and taught me basically everything from how to calculate major element molar abundances to how to run a SIMS. Ed and I spent countless hours watching Gilmore Girls and polishing grains for sample analyses. We almost lost our minds after a week in the basement of the ASU geology building. Actually, strike that, we did lose our minds. One of the greatest things about geology is the bonding time you get when you're stuck doing fieldwork with someone for an extended period of time. In our case, we were stuck in a basement for ~22 hours a day for 5 days. Anyways, Ed has been a great mentor and a great friend.

I would like to thank everyone involved with the various analytical work involved with this project. I will start with Donggao Zhao and for all of his help with EPMA analysis at the University of Texas at Austin. I would like to thank Lynda Williams and Rick Hervig at Arizona State University for all of their help during our SIMS analyses and an additional thanks goes to Lynda for housing during those analyses. I would like to thank Nate Miller for all of his help conducting LA-ICP-MS analyses at the University of Texas at Austin.

Lastly, I would like to thank my friends and family for their endless support over the past two years. Mom and Dad, thank you for being the parents that came to just about every Science Fun Day at Stone and for telling my fifth grade teacher that there is no such things as teaching your child too much science. Thank you for building cookie volcanoes with me, for teaching me how to test soil pH, and simply for always supporting me (even when I went through my emo phase).

Abstract

Effects of magma chamber processes on water and H₂O/Ce ratios in HIMU magmas from the Cook-Austral Islands: New insights from clinopyroxene phenocrysts

Leslie Ann Bruce, M.S.

The University of Texas at Austin, 2017

Supervisor: John C. Lassiter

The HIMU mantle end member is characterized by a radiogenic Pb-isotopic composition and is thought to represent recycled oceanic crust. Therefore, the H₂O content of HIMU mantle sources can provide constraints on the amount of H₂O recycled into the deep mantle via subduction. Low H₂O/Ce ratios (<100) have been reported for EM-type submarine quenched glasses, suggesting a relatively “dry” source [Dixon et al., 2002]. Olivine-hosted melt inclusions in HIMU lavas from Mangaia, Cook Islands have H₂O/Ce ratios up to 245, suggesting a damp source [Cabral et al., 2014]. On the other hand, Jackson et al. [2015] reported low H₂O/Ce ratios (<100) in submarine glasses from Tuvalu seamount with HIMU-like isotopic signatures. Hydrogen diffusion is rapid in olivine and could result in H₂O loss or gain in olivine-hosted inclusions after entrapment. Hydrogen diffusion is slower in clinopyroxene than in olivine. Therefore, we measured H₂O, major and trace elements of clinopyroxene phenocrysts in a suite of lavas from the Cook-Austral Islands. Calculated H₂O concentrations and H₂O/Ce ratios of melts in

equilibrium with pyroxene phenocrysts range from 0.26 to 3.1 wt% and 78 to 304, respectively. H₂O concentrations of melts in equilibrium with pyroxene phenocrysts are systematically higher than most olivine-hosted melt inclusions from the same samples. These observations suggest that olivine-hosted melt inclusions often experience post-entrapment H₂O loss. Additionally, negative global correlations between H₂O/Ce and Ce show that low H₂O/Ce ratios are likely the result of high Ce rather than low H₂O. Although open and closed system degassing models show little H₂O loss at pressures greater than 10 to 50 MPa, there is a strong correlation between H₂O/Ce and entrapment pressure in global OIB data. We propose H₂O may be lost via “sparging” where CO₂-rich vapors generated at high-pressures percolate through magmas at lower pressures, resulting in degassing trends that approach isopleths of constant CO₂/H₂O. Because most samples previously used to constrain H₂O/Ce in different OIB mantle sources have low quench or entrapment pressures, previous estimates of H₂O/Ce ratios in EM and HIMU mantle may be too low.

Table of Contents

1. Introduction	1
2. Background.....	7
3. Sample Description	10
4. Methods	11
5. Results	13
5.1 Clinopyroxene Major Elements	13
5.2 Clinopyroxene H ₂ O Content	13
5.3 Clinopyroxene Trace Elements.....	14
6. Discussion.....	15
6.1 Calculation of magmatic compositions from pyroxene phenocrysts	15
6.2 Post-entrapment diffusive H ₂ O loss in olivine-hosted melt inclusions ...	18
6.3 Variations in magmatic H ₂ O and H ₂ O/Ce ratios calculated from pyroxene phenocrysts in the Cook-Austral Islands	22
6.4 Global H ₂ O/Ce ratios and possible variations in source lithology	28
6.5 Degassing models for global OIB melt inclusions and glasses	30
6.6 Estimating source H ₂ O content from pyroxene phenocrysts	34
7. Conclusions	36
Appendix A	61
References	131

List of Tables

Table 1: Average major element compositions of clinopyroxene phenocrysts..	52
Table 2: Average trace element compositions of clinopyroxene phenocrysts ...	55
Table 3: Average composition of melts calculated from pyroxene phenocrysts...	58
Table A1: Precision and accuracy of secondary standard Cr-Augite and Kakanui Horblende	79
Table A2: Blank corrected OH/Si intensities and known H ₂ O concentrations of standards used for SIMS analyses	80
Table A3: Individual and averaged calculated intensities of SIMS secondary standard PMR 53.....	85
Table A4: Average measured trace element composition of LA-ICP-MS secondary standrad BCR-2G compared to published values.....	86
Table A5: Individual clinopyroxene major, trace, and volatile compositions	87
Table A6: Individual major, trace, and volatile compositions of melts calculated from pyroxene phenocrysts	110

List of Figures

Figure 1:	(A) Cpx phenocryst Mg# vs. whole rock Mg#; (B) Cpx Mg# vs. host melt Mg#.....	37
Figure 2:	REE concentrations of measured pyroxene phenocrysts, melts calculated from pyroxene phenocrysts, whole rocks, and olivine hosted melt inclusions.....	38
Figure 3:	Average cpx Mg# vs. average olivine Mg#	39
Figure 4:	Average calculated cpx/whole rock K_D vs. average calculated cpx/melt K_D	40
Figure 5:	Average H ₂ O (wt%) of melts in equilibrium with cpx vs. average H ₂ O (wt%) of olivine-hosted melt inclusions.....	41
Figure 6:	(A) Whole rock ²⁰⁶ Pb/ ²⁰⁴ Pb vs. average H ₂ O/Ce ratios of melts in equilibrium with cpx, as well as global OIB and MORB data; (B) whole rock ⁸⁷ Sr/ ⁸⁶ Sr vs. average H ₂ O/Ce ratios of melts in equilibrium with cpx, as well as global OIB and MORB data.....	42
Figure 7:	(A) Calculated H ₂ O contents of melts in equilibrium with cpx vs. calculated Mg# of melts in equilibrium with cpx; (B) Calculated Ce contents vs. calculated Mg# of melts in equilibrium with cpx	43
Figure 8:	(A) Calculated H ₂ O contents of melts in equilibrium with cpx vs. calculated La/Sm ratios of melts in equilibrium with cpx; (B) Calculated Ce contents of melts in equilibrium with cpx vs. calculated La/Sm of melts in equilibrium with cpx	44

Figure 9: (A) Calculated H₂O of melts in equilibrium with cpx vs. calculated Sm of melts in equilibrium with cpx. (B) Calculated Ce contents of melts in equilibrium with cpx vs. calculated Sm of melts in equilibrium with cpx45

Figure 10: (A) H₂O (wt%) vs. Ce (ppm) of calculated melts from the Cook-Austral Islands, and their corresponding melt inclusions, as well as global OIB and MORB data; (B) H₂O (wt%) of calculated melts from the Cook-Austral Islands, and their corresponding melt inclusions, as well as calculated melts from the Canary Islands vs. corresponding whole-rock K₂O (wt%)46

Figure 11: H₂O/Ce vs. Ce (ppm) of calculated melts from the Cook-Austral Islands, and their corresponding melt inclusions, as well as global OIB and MORB data48

Figure 12: (A) H₂O/Ce vs. CaO/Al₂O₃ of calculated melts from the Cook-Austral Islands, and their corresponding melt inclusions, as well as global OIB and MORB data; (B) H₂O/Ce vs. Na/Ti of calculated melts from the Cook-Austral Islands, and their corresponding melt inclusions, as well as global OIB and MORB data49

Figure 13: (A) CO₂ (ppm) vs. H₂O (wt%) of melt inclusions from the Cook-Austral islands, as well as glasses and melt inclusions from other OIB..50

Figure 14: (A) Saturation pressure vs. H₂O/Ce ratios of melt inclusions from the Cook-Austral islands, as well as glasses and melt inclusions from other OIB.....51

Figure A1: (A) Measured H₂O vs. Mg# of clinopyroxene phenocrysts; (B) Measured Ce vs. Mg# of clinopyroxene phenocrysts67

Figure A2: (A) Measured H ₂ O vs. La/Sm ratios of clinopyroxene phenocrysts; (B) Measured Ce vs. La/Sm ratios of clinopyroxene phenocrysts	68
Figure A3: Average Ce concentrations of melts calculated from pyroxene and olivine-hosted melt inclusions from the same samples vs. whole-rock Ce concentrations	69
Figure A4: Cpx phenocrysts/Total phenocrysts vs. whole-rock ²⁰⁶ Pb/ ²⁰⁴ Pb	70
Figure A5: Calculated pyroxene/melt K _D values of a representative pyroxene grain at different temperatures	71
Figure A6: (A) Measured H ₂ O concentrations of pyroxene phenocrysts vs. calculated pyroxene/melt K _D (H ₂ O) values; (B) H ₂ O content of melts calculated from pyroxene phenocrysts vs. calculated pyroxene/melt K _D (H ₂ O) values	72
Figure A7: ΔH ₂ O (wt%) vs. calculated pyroxene/melt K _D (H ₂ O).....	73
Figure A8: H ₂ O (wt%) in melt inclusions vs. melt inclusion diameter (long axis)	74
Figure A9: Average phenocryst size (cm) vs. average phenocryst H ₂ O content (wt%)	75
Figure A10: Core to rim transects of H ₂ O content in six pyroxene phenocrysts	76
Figure A11: SIMS beam intensity (counts per second) vs. analysis time	77
Figure A12: Known H ₂ O concentrations of standards vs. blank corrected OH/Si intensity for all standards used for SIMS analysis	78

Chapter 1: Introduction

The amount of H₂O returned to the deep mantle via subduction is fundamental to our understanding of the mechanisms driving plate tectonics, mantle degassing, and mantle convection. Even small amounts of H₂O can significantly decrease the mantle solidus, and can have major effects on chemical signatures of generated melts [Klein and Langmuir, 1987; Hirth and Kohlstedt, 1996]. H₂O can significantly decrease the high-temperature creep strength of olivine crystals or aggregates of olivine crystals. This weakening of mantle material lowers its viscosity [Hirth and Kohlstedt, 1996; Zhao et al., 2004]. Lowering mantle viscosity can alter the rate of plate motion, mantle degassing, and mantle convection.

The mantle of the Earth is isotopically heterogeneous [e.g., Zindler et al., 1982; Hart and Zindler, 1986]. It has been suggested that much of this heterogeneity largely results from the recycling of crustal material (oceanic and continental). Numerous studies have suggested various isotopically distinct mantle end members, such as: DMM (depleted MORB mantle), EM1 (enriched mantle 1), EM2 (enriched mantle 2), and HIMU (high $\mu = {}^{238}\text{U}/{}^{204}\text{Pb}$) [White et al., 1985; Hart and Zindler, 1986; Hofmann et al. 1997]. DMM is sampled by mid-ocean ridge basalts, and is representative of the geochemically depleted shallow upper mantle [Hofmann, 1988]. EM1 has been suggested to represent either recycled oceanic crust with pelagic sediments [Weaver, 1991; Chauvel et al., 1992] or metasomatized subcontinental lithosphere [McKenzie and O’Nions, 1983]. EM2 likely represents recycled oceanic crust containing continent derived sediment [Hofmann and White, 1982; Chauvel et al., 1992; Jackson et al., 2007; Workman et al., 2008]. Lastly, HIMU is thought to represent ancient (< 2 Ga) recycled oceanic crust, and is characterized by highly radiogenic Pb-isotopes [Chase, 1981;

Hofmann and White, 1982; Zindler et al., 1982; Dixon et al., 2002; Lassiter et al., 2003; Chan et al., 2009; Cabral et al., 2014; Jackson et al., 2015]. However, alternative sources for these various mantle endmembers have been suggested. For example, Hart et al. [1986] suggested that the HIMU and possibly EM1 source could be generated from metasomatism of the continental lithosphere. If these mantle endmembers do in fact represent recycled material, they can provide constraints on the geochemical cycling of material in and out of the mantle.

Prior to subduction, oceanic lithosphere experiences low-temperature alteration due to the near-ridge and off-ridge circulation of seawater-derived fluids within the oceanic crust (and mantle), and thus becomes enriched in both H₂O and CO₂ over time [Staudigel et al., 1996]. This altered oceanic lithosphere is then subducted at a plate boundary and undergoes dehydration reactions, which release both H₂O and CO₂. The amount of H₂O and CO₂ released during subduction, as well as the amount returned to the deep mantle, is still a major point of contention (e.g., Cabral et al. [2014] vs. Jackson et al. [2015]). One way of constraining the amount of H₂O recycled into Earth's deep mantle via subduction is by analyzing H₂O concentration variations in basalts that are derived from mantle sources that contain high abundances of recycled material, such as EM1, EM2, and HIMU mantle.

Constraining primary magma volatile contents is difficult because magmas experience degassing during ascent and eruption. Therefore, measurements of volatile concentrations within subaerially erupted basalts are not an accurate representation of primary magmatic volatile concentrations. As a result, submarine glasses and melt inclusions (subaerial or submarine) are used to constrain primary magmatic H₂O content. Glasses and melt inclusions form at greater depths than subaerially erupted basalts where H₂O loss from magma degassing is thought to be less significant. These proxies are thus

thought to be a more accurate representation of primary magmatic volatile concentrations.

There are several mechanisms that affect (or control) the primary magmatic H₂O content in melt inclusions and glasses, such as partial melting and fractional crystallization. H₂O is thought to be a conserved incompatible element [Hofmann et al., 1986; Michael, 1995]. Therefore, H₂O should decrease in a melt as partial melting increases and increase in a melt as fractional crystallization increases. H₂O and Ce have similar incompatibilities [Michael, 1995; Danyushevsky et al., 2000], which means H₂O/Ce ratios should remain relatively unchanged during melting or differentiation. Therefore, as a means to “see through” magmatic processes, H₂O/Ce ratios of glasses and melt inclusions have been used to calculate mantle H₂O contents. If the source Ce content can be constrained, then it is possible to estimate source H₂O content using measured H₂O/Ce ratios of glasses and melt inclusions.

Furthermore, H₂O/Ce ratios measured in melt inclusions and glasses can provide estimates for the efficiency of dehydration during subduction, if the concentrations of H₂O and Ce are known for the pre-subducted source material. In fact, average H₂O and Ce contents of pre-subducted source material have been estimated based on measurements of fresh and altered mid-ocean ridge basalts (MORB) and sediments from a variety of locations. Altered oceanic crust has H₂O concentrations ranging from 2 to 3 wt.%, average Ce contents of ~6 ppm, and H₂O/Ce ratios of between 2,500 and 5,000 [Dixon et al., 2002]. Globally, subducted sediments have an average H₂O concentration of ~7.3 wt.%, average Ce concentrations of ~57 ppm, and an average H₂O/Ce ratio of 1,280 [Dixon et al., 2002].

Several studies have found that localities with erupted basalts and glasses that sample EM1 and EM2 mantle sources (e.g. Pitcairn, Society and Samoa) have low

H₂O/Ce ratios (<90) [Workman et al., 2006; Kendrick et al. 2014]. Based on estimates for pre-subducted source material from Dixon et al. [2002], the low H₂O/Ce ratios reported in basalts from EM localities have been interpreted to reflect high degrees of slab dehydration (~95-98% dehydration) [Dixon and Clauge, 2001; Dixon et al., 2002; Workman et al., 2006; Kendrick et al. 2014; Kendrick et al., 2017]. Therefore, these localities are thought to sample a relatively “dry” mantle source. For example, glasses from Pitcairn have an average H₂O/Ce ratio of 80 [Kendrick et al., 2014]. Bizimis and Peslier [2015] estimated that the EM source of Pitcairn has a Ce concentration of ~2 ppm. For this estimation, they assumed that the EM-1 source has a similar Ce concentration as the HIMU and EM-2 source, which are estimated to be 2.2 [Cabral et al., 2014] and 1.92 ppm respectively [Workman et al., 2004]. Based on this estimate of Ce content for the EM-1 source, Bizimis and Peslier [2015] suggest that the EM-1 source of Pitcairn has a H₂O concentration of ~160 ppm. For comparison, estimated H₂O concentrations of DMM, which is thought to be relatively dry, range from 54 ppm to 116 ppm [Simons et al. 2002; Salters and Stracke, 2004; Bizimis and Peslier, 2015]. Because estimated H₂O concentrations of the EM source at Pitcairn are similar to estimates for DMM, the recycled material in the EM source is thought to have lost the vast majority of its H₂O during subduction.

The H₂O content for HIMU mantle, however, is still largely unknown based on the variability of H₂O/Ce ratios reported for this endmember. Cabral et al. [2014] reported H₂O/Ce ratios of homogenized melt inclusions from Mangaia, Cook Islands, ranging from 119 to 245. Cabral et al. [2014] also estimated that the H₂O content of the HIMU source is ~440 ppm based on the average H₂O/Ce ratio in HIMU melt inclusions (~200) and assuming a HIMU Ce content of 2.2 ppm. This estimate suggests the HIMU mantle is ~4 to 8x “wetter” than DMM. More recently however, Jackson et al. [2015]

reported much lower $\text{H}_2\text{O}/\text{Ce}$ ratios (75-84) from HIMU submarine glass samples collected from the Tuvalu seamount. Using an average $\text{H}_2\text{O}/\text{Ce}$ ratio of 79 from these glasses and assuming a similar HIMU source Ce content (2.2 ppm), Jackson et al. [2015] estimated the HIMU source sampled by Tuvalu glasses contains only ~ 174 ppm H_2O , similar to estimates for EM mantle.

Although melt inclusions and glasses are thought to form at depths at which little to no H_2O loss occurs, there are several processes other than partial melting and fractional crystallization that can also affect H_2O contents in these samples. For example, elevated Cl/K ratios (< 0.1) in some MORB and OIB indicate that melts can assimilate seawater-derived brines or altered oceanic crust prior to eruption and/or quenching [e.g., Michael and Schilling, 1989]. Other studies have also shown that melt inclusions may experience H_2O loss via post-entrapment diffusion [Wallace, 2005; Chen et al., 2011; Cabral et al., 2014]. In either case (H_2O gain or loss), the measured $\text{H}_2\text{O}/\text{Ce}$ ratios will not accurately reflect primary magmatic H_2O content. Analyses of clinopyroxene phenocrysts offer a new means for testing H_2O loss or gain in melt inclusions and glasses.

Phenocrysts typically form at higher pressures (during magma storage) than submarine quenched glasses, which form during eruption. Because degassing occurs at lower pressures, pyroxene phenocrysts that grew during magma storage prior to eruption may be more reliable indicators of magmatic H_2O content than submarine glasses. Additionally, several studies have shown that hydrogen diffusion is slower in clinopyroxene than in olivine [Hirschmann et al., 2005; Warren and Hauri, 2014; Bucholz et al., 2013]. Therefore, if pyroxene phenocrysts grew in equilibrium with melt inclusion host phenocrysts, magmatic H_2O contents inferred from pyroxene phenocrysts can be directly compared to melt inclusion H_2O . This comparison can be used to test for post-entrapment diffusive H_2O loss. We seek to estimate a minimum H_2O content of the

HIMU mantle by examining pyroxene phenocrysts in a suit of HIMU basalts from the Austral Islands. Additionally, we seek to understand how various processes such as magma degassing and hydrogen diffusion affect H_2O and H_2O/Ce ratios within the Cook-Austral Islands basalts. We also seek to understand on a broader scale to what extent H_2O/Ce ratios track variations in source composition. Therefore, we have measured structurally bound hydrogen as well as major and trace element compositions in clinopyroxene phenocrysts hosted in 12 basalts collected from the Cook-Austral Islands.

Chapter 2: Background

This study focuses on the Cook-Austral Islands of Mangaia, Raivavae, and Rapa Iti. The Cook-Austral Islands are located in the French Polynesia region of the South Pacific south of Tahiti. The island of Raivavae is located adjacent to the Austral Fracture Zone (AFZ), which separates the northern and southern islands [Sandwell and Smith, 1997; Lassiter et al., 2002; Lassiter et al., 2003]. Mangaia is the northernmost island of the three, and Rapa is the southernmost island.

Basalts from Mangaia and Raivavae have highly radiogenic Pb-isotopic values ($^{206}\text{Pb}/^{204}\text{Pb}$ between 19.29 and 21.93) and low Sr-isotopic values ($^{87}\text{Sr}/^{86}\text{Sr} \sim 0.7028$). These basalts also have enriched Nd- and Hf- isotopic compositions, with ϵNd values ranging from 5.2 to 7.8 and ϵHf values ranging from 6.8 to 11.5 [Woodhead, 1996; Lassiter et al., 2003; Chan et al., 2009]. Lassiter et al. [2003] suggested that the northern Austral Islands sample a mixture of both a HIMU-like component and a DM-like component, based on their isotopic signatures. Lassiter et al. [2003] suggested that the negative correlation between Pb- and Nd-isotopic values in basalts from Raivavae and the other northern islands, such as Mangaia, is consistent with mixing between a HIMU-like component and a DMM-like component.

In addition to distinctive HIMU-like isotopic signatures, the northern Austral Islands have trace element compositions consistent with an ancient recycled component. For example, lavas from Raivavae show a negative correlation between $^{206}\text{Pb}/^{204}\text{Pb}$ and K/U ratios [Lassiter et al., 2003]. Such correlations arise during subduction because dehydration reactions preferentially remove fluid soluble elements (e.g. K) from the slab relative to immobile elements (e.g. U) [Weaver, 1991]. The correlation between Pb-isotopes and K/U in Raivavae lavas suggests that 1) the low K/U ratios are a source

feature and 2) the HIMU source feature is consistent with recycled, dehydrated oceanic crust [Lassiter et al. 2003]. Additionally, Cabral et al. [2013] reported evidence for MIF (mass independent fractionation) of sulfur isotopes in olivine-hosted melt inclusions from Mangaia. Because MIF is not observed in the geologic record after 2.45 Ga [Farquar et al., 2000; Farquar et al., 2011; Johnston, 2011], they suggested that these lavas contain a recycled component that must have been on Earth's surface prior to 2.45 Ga. Therefore, S-isotopes in Mangaia basalts are also consistent with an ancient recycled component in the HIMU source.

Basalts from the southern islands, including Rapa Iti, trend to more enriched compositions, with less radiogenic Pb-isotopic values ($^{206}\text{Pb}/^{204}\text{Pb}$ between 19.07 and 19.28) and higher Sr-isotopic values ($^{87}\text{Sr}/^{86}\text{Sr} > 0.7036$). Southern lavas have less radiogenic Nd- and Hf- isotopic compositions, with ϵNd values ranging from 2.3 to 3.8 and ϵHf values ranging from 2.1 to 4.2 [Lassiter et al., 2003; Chan et al., 2009]. Lassiter et al. [2003] suggested that the enriched source could not be generated from the addition of ancient pelagic sediments to the HIMU mantle, due to the lower $^{187}\text{Os}/^{188}\text{Os}$ values reported in EM lavas compared to HIMU lavas. They suggest that the enriched source sampled at Rapa may be representative of sub-arc mantle wedge material that is recycled into the deep mantle through viscous coupling to a downgoing slab. Chan et al. [2009] further supported this hypothesis based on elevated Li-isotopes measured in Rapa basalts relative to fresh MORB.

Lavas from these three islands are ideal for this study because both whole rock and olivine-hosted melt inclusion data already exist for most of the samples. This allows us to compare melt H_2O contents (calculated from clinopyroxene H_2O content) to the H_2O content of corresponding melt inclusions. Furthermore, host lavas from these

samples span a large range of Pb-isotopic compositions, which allows us to determine if H_2O/Ce ratios correlate with source compositional variations.

Chapter 3: Sample Description

For this study, we selected a subset of 11 Raivavae and Rapa basalts collected by John Lassiter and Hans Barschus in 1997. Of the 11 basaltic samples, 7 are from Raivavae and 4 from Rapa. We also selected one Mangaia sample (MG1001) provided by Matt Jackson. H₂O/Ce ratios of olivine-hosted melt inclusions from this sample have previously been reported by Cabral et al. [2014], and are systematically higher than H₂O/Ce ratios reported in HIMU Tuvalu glasses [Jackson et al., 2015]. Whole rock major, trace, and Pb-Sr-Nd-Hf-Os isotopic data for these samples are presented in Lassiter et al. [2003], Chan et al. [2009], and Herzberg et al. [2014]. Selected basalts from all three localities are alkalic and phenocryst-rich. Olivine and clinopyroxene modal abundances are >10% by volume, with the exception of sample RVV 316 (olivine ~7% and cpx ~5% by volume). Whole rock Mg#s [$\text{Mg}^{2+}/(\text{Mg}^{2+} + \text{Fe}^{2+})$] range from 38 to 75.

Many olivine phenocrysts within basalts selected for this study host melt inclusions, which have previously been studied by Lassiter et al. [2002], Szramek [2010], and Cabral et al. [2014]. Olivine-hosted melt inclusions have Mg#s that range from 45 to 61. Host olivine Mg#s range from 75 to 83. H₂O contents in melt inclusions range from 0.24 to 1.50 wt.%, Ce concentrations range from 28 to 339 ppm, and H₂O/Ce ratios range from 33 to 165. Melt inclusion La/Sm ratios range from 2.4 to 9.3. Complete major, trace, and volatile (H₂O, CO₂, Cl) data of olivine-hosted melt inclusions for a subset of samples (RVV 310, RVV 318, RVV 370, RPA 502 and MG1001) are presented in Lassiter et al. [2002] and Cabral et al. [2014]. Major, trace and chlorine data of other olivine-hosted melt inclusions (RVV 316, RVV 321, RVV 343, and RVV 346) are presented in Szramek [2010].

Chapter 4: Methods

We selected 99 pristine clinopyroxene phenocrysts for major, trace, and H₂O analysis. Phenocrysts were mounted in indium to minimize H₂O contamination during analysis. Grains were first mounted in crystal bond and polished to 1 μm prior to placement in the indium mounts. Following polishing, the crystal bond was dissolved in an acetone bath. Individual polished grains were then washed in a series of baths: clean acetone, ethanol, and DI water. Finally, the grains were dried, mounted in indium, pressed to achieve a flat surface, and carbon coated for chemical analyses.

Major elements were analyzed via EPMA at the University of Texas at Austin using procedures outlined in Gao et al. [2016]. Following major element analysis, pyroxene phenocrysts were analyzed for hydrogen via the Cameca 6f SIMS at Arizona State University. For SIMS analyses we used matrix-matched olivine and pyroxene standards from Mosenfelder and Rossman [2013 A and B]. Following SIMS analysis, pyroxene phenocrysts were analyzed for trace elements using LA-ICP-MS at the University of Texas at Austin. We analyzed the exact same spots (or as close as possible) from EPMA and SIMS measurements to maintain consistency across all data sets. See Appendix A for a more detailed description of analytical methods.

Secondary standards used for EPMA analysis were Cr-Augite 164905 and Kakanui Hornblende. For elements with concentrations greater than 1 wt%, reproducibility of both standards was better than 2%. For elements with concentrations less than 1 wt%, reproducibility ranged from better than 5% for Cr₂O₃, 11% for Na₂O, MnO, TiO₂, and better than 12% for MnO. Averaged analyses were accurate within 5% of published values for all elements, except for Mn (within 8%) (Jarosewich et al., 1980).

PMR-53 was used as a secondary standard for SIMS analysis for quantification of analytical error. Repeated analyses of PMR-53 were precise (1σ standard deviation) within 13%. Although the concentration of PMR-53 is disputed, the OH/Si intensities that observed in repeated analyses of PMR-53 are within the range of previously published OH/Si values for PMR-53 [202 to 268 ppm; Mosenfelder and Rossman, 2013 B and references therein].

Repeated analyses of LA-ICP-MS secondary standard, BCR-2G, were accurate within 6% of published values for all elements other than Ti (8%) and Pb (7%) (see Appendix Table A4). Repeated analyses of BCR-2G were reproducible within 5% (one standard deviation) for all elements other than Tm (13%), Lu (11%), and U (6%).

Chapter 5: Results

5.1 Clinopyroxene Major Elements

Major element compositions were collected for 141 spot analyses from 99 pyroxene phenocrysts and are presented in Appendix Table A5. Average clinopyroxene major element concentrations of individual basalt samples are presented in Table 1. Diopside is the dominant component of the clinopyroxene phenocrysts, with the exception RVV 343, which is augitic in composition. Clinopyroxene Mg#s range from 63 to 86, with an average Mg# of 81. Clinopyroxene Mg#s within individual whole rocks span a large range. For example, RPA 367 has a whole rock Mg# of 69, but individual clinopyroxene grains have Mg#s ranging from 75 to 87 (Figure 1).

5.2 Clinopyroxene H₂O Content

Individual clinopyroxene phenocryst H₂O contents are reported in Appendix Table A5 and average pyroxene H₂O contents of phenocrysts from individual basalt samples are reported in Table 1. H₂O contents of individual pyroxene phenocrysts range from 72 to 1019 ppm. Average H₂O contents of pyroxenes from individual basalts range from 90 to 756 ppm. Sample RVV 343 has the lowest average H₂O content of 90±13 ppm and is the second most evolved sample from this study (Mg# = 75). Sample RVV 321 has the highest average H₂O content of 756±100 ppm. However, RVV 321 is the third most evolved sample from this study (whole rock Mg# = 76). Intra-sample variability (standard deviation) ranges from 13 to 195 ppm. Clinopyroxene H₂O content does not correlate with indices of fractional crystallization (e.g., Mg#) or indices of melting (e.g., La/Sm ratios) (Appendix Figure A1a and A2a).

5.3 Clinopyroxene Trace Elements

Individual clinopyroxene phenocryst trace element compositions are reported in Appendix Table A5 and average pyroxene trace element compositions of phenocrysts from individual basalts are reported in Table 2. Normalized abundances of clinopyroxene phenocrysts show a decrease by nearly one order of magnitude moving from MREE to HREE. Pyroxene phenocrysts also show a moderate concave down LREE pattern (Figure 2). Ce concentrations ranges from 3.3 to 34.5 ppm. Clinopyroxene Ce content correlates with clinopyroxene Mg# and La/Sm ratios (Appendix Figure A1b and A2b). Ce content and Mg# are negatively correlated within pyroxene phenocrysts from individual samples. This correlation within individual samples creates negative sub-parallel trends, which are offset from sample to sample.

Chapter 6: Discussion

6.1 Calculation of magmatic compositions from pyroxene phenocrysts

During magma ascent, H₂O and CO₂ can be lost through degassing. Therefore, previous studies have used both submarine quenched glasses and olivine-hosted melt inclusions to constrain pre-eruptive magmatic H₂O content. Submarine glasses typically form at relatively shallow pressures (<50 MPa). However, simple degassing models suggest that ascending magmas primarily lose CO₂ at pressures greater than a few hundred bars, but that H₂O loss at these pressures is limited [Dixon et al., 1997]. Olivine-hosted melt inclusions from the Austral Islands typically have significantly greater entrapment pressures, between 100 and 200 MPa [Lassiter et al. 2002; Cabral et al. 2014]. These pressures suggest that melt inclusions within olivine phenocrysts formed during magma storage in crustal reservoirs prior to eruption. Numerous studies have examined geochemical variations in melt inclusions to explore a variety of magma chamber processes [e.g. Saal et al., 1998; Lassiter et al., 2002]. However, although melt inclusions may trap melts prior to magma ascent and degassing, there is a potential for post-entrapment H₂O loss due to rapid H diffusion through olivine [Mackwell and Kohlstedt, 1990; Demouchy et al., 2006; Lloyd et al., 2013].

Clinopyroxene phenocrysts can provide an alternative proxy for examining compositional variations of melts in crustal reservoirs prior to eruption. In the Cook-Austral Islands, olivine and clinopyroxene phenocrysts span similar ranges in Mg# (Figure 3). This suggests that the pyroxene and olivine phenocrysts grew at similar stages of melt evolution. Therefore, pyroxene phenocrysts likely formed at similar pressures as the olivine phenocrysts. Several recent studies have shown that hydrogen diffusion is slower in clinopyroxene than in olivine [Hirschmann et al., 2005; Warren and Hauri,

2014; Bucholz et al., 2013]. Therefore, pyroxene phenocrysts may be less susceptible to post-entrapment H₂O loss than olivine-hosted melt inclusions.

We calculated clinopyroxene/melt trace element K_D s using the program BigD [Nielsen, 1992]. Using these partition coefficients and measured clinopyroxene trace element compositions, we calculated melt trace element compositions. Calculation of pyroxene/melt K_D s requires constraints on the major element composition of the melt and temperature of the melt from which the pyroxene phenocrysts grew. For this calculation, we assume that the melts from which the pyroxenes grew are compositionally similar to the host basalts when corrected for fractionation. This assumption is supported by observed correlations between average phenocryst trace element abundances and whole rock trace element abundances (Appendix Figure A3), as well as correlations between phenocryst olivine:cpx ratios and whole rock isotopic composition (Appendix Figure A4). Therefore, for each phenocryst we approximated the composition of the melt from which it grew by adding or subtracting variable amounts of clinopyroxene and olivine to the host whole rock (in the relative proportions observed for that sample) until the calculated melt Mg# matches that expected from the clinopyroxene phenocryst Mg#, assuming melt/phenocryst equilibrium. The average measured pyroxene composition from each sample was used for this calculation. Average olivine forsterite content was assumed to be in equilibrium with this clinopyroxene composition. In addition, we used the calculated major element compositions of olivine in equilibrium with clinopyroxene to generate melt temperature estimates using the olivine thermometer from Eqn. 2 of Putirka et al. [2007]. However, for all trace elements discussed in the following sections, partition coefficients generated from BigD are insensitive to temperature (Appendix Figure A5).

Calculated melt compositions are reported in Appendix Table A6, and the average trace element compositions calculated for each sample is reported in Table 3. Within several samples, melts calculated from pyroxene phenocrysts span a wide range in trace element composition. For example, melts inferred from RPA 367 phenocrysts have Ce concentrations ranging from 39 to 145 ppm. Other samples have relatively homogeneous pyroxene phenocryst populations. For example, melts inferred from RPA 502 phenocrysts have Ce concentrations that range from 71 to 81 ppm, which is only slightly greater variability than that expected due to analytical uncertainty (~4%). Melt Ce content inferred from the entire analyzed suite ranges from 33 to 145 ppm. Trace element compositions of melts in equilibrium with pyroxene overlap with measured whole rock compositions (Figure 2). Additionally, K_D values generated by BigD are consistent with measured pyroxene/whole rock concentration ratios for most trace elements (e.g., La, Ce, Sm, and Yb; Figure 4). This further supports the assumption that the melts from which the pyroxene phenocrysts grew are compositionally similar to the host basalts. Calculated melt trace element compositions also overlap with olivine-hosted melt inclusions from the same samples (Figure 2). However, melt inclusions have, on average, greater incompatible trace element concentrations than either melts calculated from pyroxene compositions or the host basalts.

Melt H₂O concentrations were estimated from measured clinopyroxene H₂O content using pyroxene/melt K_D s estimated from pyroxene tetrahedral Al content [Hauri et al., 2006]. Calculated melt H₂O concentrations are reported in Appendix Table A6, and average melt H₂O concentrations inferred for each sample are reported in Table 3. Melt H₂O concentrations estimated from individual phenocrysts range from 0.2 to 3.2 wt.%, and melt H₂O concentration averages for phenocrysts from individual samples range from 0.3 to 2.1 wt.%. Melt H₂O/Ce ratios estimated from individual phenocrysts range from 39

to 517, and average sample melt H₂O/Ce ratios range from 63 to 321. Neither measured pyroxene H₂O concentrations nor calculated melt H₂O concentrations inferred from individual pyroxene phenocrysts correlate with calculated partition coefficients (Appendix Figure A6a and b). Pyroxene H₂O content should correlate with pyroxene/melt K_D(H₂O), if variations in magmatic H₂O content in the melts from which the pyroxenes grew are minor. However, pyroxenes span a much larger range in H₂O concentrations (71 to 1019 ppm) than in calculated K_D values (0.17 to 0.61). As a result, the correlation between pyroxene major element composition and content that should result from varying pyroxene/melt K_D(H₂O) is masked by larger variations in H₂O content of the melts from which the pyroxenes grew. This suggests that the variations in measured pyroxene H₂O content to first order are not primarily controlled by variations in H₂O partitioning. In the following sections, we evaluate whether variations in pyroxene H₂O reflect variations in magmatic H₂O content, or whether other processes such as diffusive H₂O loss or pyroxene alteration have played a significant role

6.2 Post-entrapment diffusive H₂O loss in olivine-hosted melt inclusions

Previous studies have measured H₂O and trace element concentrations in olivine-hosted melt inclusions from several of the same basalt samples from which we report clinopyroxene H₂O contents [Lassiter et al., 2002; Szramek, 2010; Cabral et al., 2014]. Figure 5 compares H₂O concentrations in melts calculated to be in equilibrium with clinopyroxene phenocrysts with H₂O concentrations in olivine-hosted melt inclusions from the same sample. Two samples (RVV 310 and MG1001) fall along the 1:1 equiline, but three other samples (RVV 318, RVV 370, and RPA 502) have significantly lower H₂O in olivine-hosted melt inclusions than in the melts calculated from pyroxene compositions.

A similar trend is observed in samples from the Canary Islands and Azores Islands. Average H₂O concentrations from both olivine-hosted melt inclusions [Longpre et al., 2017] and average melts in equilibrium with cpx [Weis et al., 2015] from the Canary Islands fall near the 1:1 equiline. This suggests that, on average, olivine-hosted melt inclusions from the Canary Islands have not lost H₂O. However, H₂O concentrations of melts in equilibrium with cpx from the Azores are systematically higher than H₂O concentrations of corresponding olivine-hosted melt inclusions [Turner et al., 2017], which suggests either post-entrapment H₂O loss in melt inclusions or that the melt inclusions were trapped at different stages of magma evolution/different depths.

Estimates of melt H₂O contents from pyroxene phenocrysts are by nature more indirect than measurements from melt inclusions because the former requires both measurement of pyroxene H₂O content and estimation of pyroxene/melt K_D(H₂O) values. In addition, pyroxene and olivine phenocrysts could potentially grow at different times from different melts with differing H₂O contents. For the two samples that fall along the 1:1 equiline (RVV 310 and MG1001), average pyroxene and olivine Mg#s from these samples indicate chemical equilibrium between these phases (Figure 3). This suggests that pyroxene and olivine in both samples grew at the same time from the same melts. The correspondence of melt H₂O content estimated from pyroxenes and measured melt inclusion H₂O content for these samples therefore suggests that our inversion method described above is robust.

For the three samples (RVV 318, RVV 370, and RPA 502) with systematically lower H₂O concentrations in the melt inclusions, it is possible that pyroxenes from these samples grew from the same magma at a different stage in evolution (e.g. a more primitive magma that is either less degassed or less fractionated) when it had a higher magmatic H₂O concentration. In fact, samples RVV 318 and RPA 502 have average

pyroxene Mg#s that are slightly more primitive than the coexisting olivine Mg#s (Figure 3). However, average pyroxene and olivine Mg#s for RVV 370 indicate chemical equilibrium (Figure 3). Therefore, it is unlikely that the higher H₂O contents of these calculated melts are the result of differences in melt composition. Alternatively, it is possible that pyroxene/melt K_D(H₂O) values were systematically underestimated in these samples, which would result in an overestimation of melt H₂O content. However, K_D values estimated for pyroxenes from these three samples are within the same range as K_D values from RVV 310 and MG1001. Additionally, there is no correlation between estimated K_D values and calculated melt H₂O content (Appendix Figure A6b), or the difference between calculated melt H₂O content and measured melt inclusion H₂O content (Appendix Figure A7). Therefore, systematic error in estimates of pyroxene/melt K_D(H₂O) values is also not likely the explanation for higher H₂O contents recorded in pyroxene from these samples.

Olivine-hosted melt inclusions are susceptible to H₂O loss through rapid H diffusion in slow cooling melts [Hauri, 2002; Cervantes and Wallace, 2003; Berlo et al., 2012]. Typically, this can be avoided if melt inclusions from scoria samples are used [Cervantes and Wallace, 2003; Kelley et al., 2010]. However, on older ocean islands, scoria is rapidly eroded and is also typically more heavily altered than the interiors of massive flows. Therefore, previous studies of melt inclusions from ocean island basalts have primarily relied on melt inclusions from massive flows [e.g. Lassiter et al., 2002 and Cabral et al., 2014]. Within natural samples, hydrogen diffusion has been shown to be more rapid in olivine than pyroxene by nearly a factor of 100 [Warren and Hauri, 2014]. Therefore, olivine-hosted melt inclusions are likely more susceptible to diffusive H₂O loss than are the cores of pyroxene phenocrysts. Diffusive H₂O loss should result in a correlation between inclusion size and H₂O content, because large inclusions are less

susceptible to diffusive H₂O loss [Chen et al., 2011]. Cabral et al. [2014] reported that H₂O concentrations in melt inclusions from one Mangaia sample (MGA-B-47) correlate with inclusion diameter. They suggested that this sample had lost H₂O through post-entrapment diffusion. In contrast, H₂O concentrations in melt inclusions from MG1001, which have similar H₂O contents as melts inferred from pyroxene phenocrysts from MG1001 (this study), do not correlate with inclusion diameter. Therefore, they suggested that melt inclusions from this sample had not experienced significant post-eruptive H₂O loss. In detail, we should also expect H₂O loss to correlate with flow thickness and sample distance to flow margins. However, this information is not available for the samples available for this study.

Melt inclusions from samples RVV 318, RVV 370, and RPA 502 are systematically smaller than those studied by Cabral et al. (2014), making them more susceptible to diffusive H₂O loss. Broad correlations ($R^2 = 0.275$) between inclusion H₂O content and inclusion diameter are observed in all three samples (Appendix Figure A8). The significance of these correlations ranges from 98.7% to 99.9% using a two-tailed student t-test. This suggests that melt inclusions from these samples have likely lost H₂O through post-entrapment diffusion.

We therefore infer that diffusive H₂O loss is the most likely explanation for the systematic differences observed between melt inclusion H₂O contents and H₂O contents of melts estimated from pyroxene. Based on the evidence presented above, magmatic H₂O contents calculated from pyroxene phenocrysts are likely a more robust estimate for pre-eruptive magmatic H₂O content than olivine-hosted melt inclusions in ocean island basalts where scoria is not readily available. In the following discussion we examine variations in magmatic H₂O content calculated from pyroxene with other geochemical tracers calculated from pyroxene.

6.3 Variations in magmatic H₂O and H₂O/Ce ratios calculated from pyroxene phenocrysts in the Cook-Austral Islands

Previous studies have estimated the amount of H₂O returned to Earth's deep mantle through subduction by measuring H₂O/Ce ratios of melts that sample Earth's mantle end-members, such as HIMU, EM-1, and EM-2 [Dixon 2002, Cabral et al. 2014, Jackson et al. 2015]. Cabral et al. [2014] and Jackson et al. [2015] reported extremely different estimates (≈ 120 ppm) for the HIMU mantle H₂O/Ce ratio. Cabral et al. [2014] reported H₂O/Ce ratios ranging from 119 to 245 in olivine-hosted melt inclusions from Mangaia. Based on these values, they estimated that the Mangaia HIMU source has an average H₂O/Ce ratio of ~ 200 . In contrast, Jackson et al. [2015] measured H₂O/Ce ratios in submarine quenched glasses from the Tuvalu seamount that span a range in Pb isotopic compositions, including samples with HIMU-like isotopic signatures. For HIMU-like glasses they reported H₂O/Ce ratios ranging from 75 to 84 in the least degassed glasses. The H₂O/Ce ratios reported in Jackson et al. [2015] fall within the same range as H₂O/Ce ratios previously reported from EM-1 and EM-2 glasses [Douglass et al., 1995 and 1999; Dixon et al., 1997; Workman et al., 2006; Kendrick et al., 2014]. Jackson et al. [2015] suggested that the high H₂O/Ce ratios reported from Mangaia melt inclusions may be the result of assimilation of seawater prior to entrapment or that there are variable processes, such as diffusive loss of H₂O but not Ce, that affect different HIMU domains, thus generating heterogeneities in the source.

The discrepancy of H₂O/Ce ratios between Mangaia and Tuvalu is problematic if H₂O/Ce ratios reflect source variations. Jackson et al. [2015] suggested that the HIMU source may be intrinsically heterogeneous. However, melt inclusions from Mangaia and glasses from Tuvalu are different types of samples, which are therefore difficult to

compare directly. For example, saturation pressures for Mangaia melt inclusions range from 39 to 212 MPa, whereas saturation pressures for Tuvalu glasses are ≤ 40 MPa. Additionally, the HIMU-like glasses from Tuvalu are highly evolved (MgO < 4 wt%) relative to HIMU-like melt inclusions from Mangaia and Raivavae [Cabral et al., 2014 and Lassiter et al., 2002 respectively]. These glasses also have Ce concentrations that extend to much higher values (avg. = 153 ppm) than in the Mangaia melt inclusions (avg. = 95 ppm), which likely reflects either lower degrees of partial melting or higher degrees of fractional crystallization of the Tuvalu magmas. Jackson et al. [2015] suggested that the low H₂O/Ce ratios reported in Tuvalu glasses indicates that the source of the Tuvalu melts has a lower H₂O/Ce ratio than the source of the Mangaia melts (~ 200 ; Cabral et al. [2014]). If we make the assumption that the estimated source H₂O/Ce ratio by Cabral et al. [2014] is correct, then it would be physically impossible for the Tuvalu melts with ~ 150 ppm Ce to contain more than 1.7 wt.% H₂O at 250 bars, which implicitly assumes zero CO₂. The Tuvalu glasses have lower H₂O content than the CO₂-free maximum and thus plot at a high H₂O/CO₂ ratio, which makes them very susceptible to H₂O loss through the addition of CO₂. Therefore at high Ce concentrations, and thus high H₂O at a constant H₂O/Ce ratio, the Tuvalu melts will approach the solubility limit.

Host basalts of pyroxene phenocrysts selected for this study span a wide range in isotopic compositions. Raivavae basalts have radiogenic Pb- and Nd-isotopic values (²⁰⁶Pb/²⁰⁴Pb ranges from 19.29 to 21.06 and ¹⁴³Nd/¹⁴⁴Nd ranges from 0.51293 to 0.51304), but have low Sr-isotopic values (⁸⁷Sr/⁸⁶Sr ranging from 0.7028 to 0.7030) [Lassiter et al. 2003; Chan et al. 2009]. Basalts from Mangaia span a narrow range in Pb-isotopic values and also have the most radiogenic Pb-isotopic compositions within the suite of samples (²⁰⁶Pb/²⁰⁴Pb ranges from 21.15 to 21.93; Woodhead, 1996) and have Sr-isotopic values that overlap with those from Raivavae (⁸⁷Sr/⁸⁶Sr ranges from 0.70265 to 0.70310).

Previous studies have suggested that these lavas sample a mixture of HIMU-like and DMM-like components. Basalts from Rapa fall off the mixing trend defined by the northern Cook-Austral. Rapa basalts have less radiogenic Pb-isotopic values for given Nd-isotopic values ($^{206}\text{Pb}/^{204}\text{Pb}$ ranges from 18.95 and 19.28 and $^{143}\text{Nd}/^{144}\text{Nd}$ ranges from 0.51274 to 0.51279). Additionally, basalts from Rapa have the most radiogenic Sr-isotopic values within the Austral Islands ($^{87}\text{Sr}/^{86}\text{Sr}$ ranges from 0.7039 to 0.7041). Based on these observations, Lassiter et al. [2003] suggested that Rapa basalts sample an EM-like or FOZO-like component. Because host basalts selected for this study span a large range of isotopic compositions, they are ideal for further examining if $\text{H}_2\text{O}/\text{Ce}$ ratios reflect differences in source composition or various magmatic processes. In the following discussion, we examine whether H_2O , Ce, and $\text{H}_2\text{O}/\text{Ce}$ ratios of melts calculated from pyroxene correlate with source features or magmatic processes.

Within HIMU-like basalts ($^{206}\text{Pb}/^{204}\text{Pb} > 19.29$) sampled at Mangaia and Raivavae, magmatic H_2O contents calculated from pyroxene range from 0.5 to 3.2 wt%. Ce and $\text{H}_2\text{O}/\text{Ce}$ ratios of melts calculated from pyroxene range from 44 to 119 ppm and 48 to 466, respectively. Within EM- or FOZO-like basalts ($^{206}\text{Pb}/^{204}\text{Pb} < 19.29$), magmatic H_2O contents calculated from pyroxene span a similar range in H_2O content, from 0.2 to 2.8 wt%. Additionally, Ce and $\text{H}_2\text{O}/\text{Ce}$ ratios of melts calculated from pyroxene span similar ranges as for the HIMU-like basalts, from 33 to 145 ppm and 39 to 517, respectively. Although host-basalts from these samples span a wide range in isotopic composition, melts calculated from pyroxene all have similar ranges in H_2O , Ce, and $\text{H}_2\text{O}/\text{Ce}$ ratios, and $\text{H}_2\text{O}/\text{Ce}$ ratios do not correlate with isotopic compositions (Figure 6).

The lack of correlation between isotopic compositions and H_2O or $\text{H}_2\text{O}/\text{Ce}$ of basalts sampling different mantle sources (e.g. HIMU+DMM vs. EM or FOZO) could result from these reservoirs having similar H_2O and $\text{H}_2\text{O}/\text{Ce}$ ratios even though these

mantle sources contain different amounts and types of subducted components that began with very different H_2O/Ce ratios. Assuming that the HIMU source represents ancient recycled oceanic crust and both EM sources represents oceanic crust plus sediment (however this is highly debated), Dixon et al. [2002] estimated H_2O and H_2O/Ce ratios of the recycled components within each endmember. They estimated that mature oceanic crust (HIMU recycled component) has H_2O/Ce ratios ranging from 2500 to 5000 and H_2O content that ranges from 2 to 3 wt% prior to subduction. Dixon et al. [2002] also estimated that global subducted sediments (EM recycled component) have H_2O/Ce ratios of ~ 1280 and H_2O contents ~ 7.3 wt% prior to subduction. Generation of similar H_2O/Ce ratios in the HIMU and EM mantle sources would therefore require the recycled component in the HIMU source to undergo more extensive dehydration than the recycled component in the EM source. Although generation of similar H_2O/Ce ratios in the HIMU and EM source due to varying amounts of dehydration, this would seem unlikely.

Alternatively, H_2O and H_2O/Ce may track various magmatic processes, such as fractional crystallization or fractionation during partial melting. For example, Bizimis and Peslier [2015] suggested that bulk $D(H_2O)$ is $\sim 5x$ lower than the $D(Ce)$ for melts derived from a pyroxenite lithology. This estimate contrasts with the similar H_2O and Ce partition coefficients estimated for peridotite lithologies. Therefore, Bizimis and Peslier [2015] suggested that variations in melt H_2O/Ce ratios track varying degrees of melting from pyroxenite and peridotite lithologies.

If variations in H_2O/Ce ratios reflect fractionation during partial melting, then there should be a correlation between H_2O and H_2O/Ce ratios with indices of partial melting, such as La/Sm. However, there is no clear correlation between H_2O or H_2O/Ce ratios with La/Sm ratios of melts calculated from pyroxene phenocrysts (Figure 8a). In contrast, there is a weak correlation between Ce content and La/Sm ratios that fall within

trends defined by global Ce and La/Sm data (Figure 8b). Additionally, because H₂O and Ce are both incompatible species, H₂O and Ce should correlate with each other, as well as with other conserved incompatible elements (e.g. Zr or Sm), regardless of whether their K_D values are identical. In fact, within global MORB data these correlations are observed and are relatively strong, with R² values ranging from 0.51 to 0.91 (Figures 8-10). Similar to global MORB-data, melts calculated from pyroxene phenocrysts show a strong correlation of Ce content with both Zr and Sm content, with R² values ranging from 0.51 to 0.91 and 0.69 to 0.86, respectively (Figure 10b). However, calculated magmatic H₂O does not correlate with Ce or other incompatible trace elements (Figures 9 and 10a). In summary, neither H₂O concentrations nor H₂O/Ce ratios appear to primarily reflect variations in the degree of partial melting.

Variations in H₂O and H₂O/Ce ratios could primarily reflect variations in the degree of fractional crystallization. If this were the case, then there should be a correlation between indices of fractional crystallization (e.g. Mg#) and H₂O or H₂O/Ce. For example, if a melt is saturated in H₂O during fractional crystallization, then it is possible that Ce will increase during crystallization, but H₂O will not. For example, calculated magmatic H₂O and Ce contents show no correlation with magmatic Mg# (Figure 7). This lack of correlation suggests that there is little to no effect of fractional crystallization on H₂O and H₂O/Ce ratios. The observations outlined above suggest that Ce is behaving as expected for a conserved incompatible element, but H₂O is not in the melts parental to the pyroxene phenocrysts.

The observation that Ce is behaving as expected for a conserved incompatible element, but H₂O is not, may suggest that some of the original H₂O concentration in pyroxene phenocrysts (prior to eruption) is lost during ascent, possibly due to diffusion. In turn, H₂O concentrations of smaller phenocrysts may be more readily affected during

eruption than larger phenocrysts because the diffusive length-scale for the time required for phenocryst ascent may be same as the size of the phenocryst. Therefore, phenocrysts that are smaller than the diffusive length-scale will have lost H₂O throughout the entire grain. However, phenocrysts larger than the diffusive length-scale will have core that are unaffected by diffusive loss. If this is true, then there should be a correlation between H₂O content and phenocryst size. Average core to rim phenocryst size ranges from 0.8 to 6.3 mm and average pyroxene H₂O ranges from 90 to 756 ppm. Broad correlations between phenocryst size and H₂O content are observed within samples from this study (Appendix Figure A9). For example, sample RVV 316 has the second lowest reported H₂O content (111 ppm), and the smallest measured phenocryst size from the entire suite of phenocrysts (0.8 mm). Additionally, sample RVV 318 on average has the largest phenocrysts (6.3 mm) and has the second highest average H₂O content (684 ppm) from the suite of phenocrysts.

We therefore suggest that, similar to olivine phenocrysts, pyroxene phenocrysts may also be susceptible to H₂O loss through diffusion. If pyroxene phenocrysts have lost H₂O through diffusion, then core to rim transects of the phenocrysts should show a decrease in H₂O content from the core to the rim. In order to further test the susceptibility of pyroxene phenocrysts to hydrogen diffusion, we measured core to rim variations in H₂O content from six phenocrysts. From the six core to rim transects, only one phenocryst shows a clear decrease in H₂O content (Appendix Figure A10). However, this phenocryst only shows a decrease in H₂O content from 654 ppm to 524 ppm (20% change in H₂O) from core to rim. Transects of five other phenocrysts show no clear correlation of H₂O content from core to rim. This suggests that although pyroxene phenocrysts show a correlation between H₂O content and phenocryst size, pyroxene phenocrysts from this study have likely not experienced any significant H₂O loss via

diffusion. Although pyroxenes from this study show no evidence for H₂O loss via diffusion, we suggest that smaller phenocrysts should be avoided for future studies because they are likely to record lower than average H₂O contents.

6.4 Global H₂O/Ce ratios and possible variations in source lithology

Several previous studies have estimated primary magmatic H₂O concentrations via measured H₂O and H₂O/Ce ratios in a variety of sample types. These studies implicitly assume that H₂O loss during magma evolution or eruption in the studied samples was minimal. Below, we examine whether global correlations of H₂O and Ce with other conserved incompatible elements reflect H₂O loss rather than true variations in source composition, as previously thought.

Although, global melt inclusions and glasses span a wide range in isotopic compositions, there are no correlations between H₂O and H₂O/Ce ratios with isotopic compositions. Similar to melt compositions calculated from pyroxene, melt inclusions and glasses show a correlation of Ce content with Sm content and La/Sm ratios, but H₂O does not. Additionally, magmatic H₂O contents of melt inclusions and glasses do not correlate with Ce content. These observations further support the observations from melts calculated from pyroxene phenocryst, in which Ce is behaving as expected for a conserved incompatible element, but H₂O is not.

Jackson et al. [2015] noted a global negative correlation between H₂O/Ce ratios and Ce content (Figure 11). They argued that variations in H₂O/Ce ratios in OIB are the result of variations in source lithology [Jackson et al., 2015]. They suggested that the high Ce contents and low H₂O/Ce ratios reported in HIMU and EM glasses may result from low degrees of melting from a dominantly pyroxenite component. They also suggest that the low Ce content and high H₂O/Ce ratios reported in MORB samples may be the

result of higher degrees of melting of a dominantly peridotitic lithology. This model is based on previous work of Bizimis and Peslier [2015], who suggested that Ce has a higher partition coefficient than H during crystallization of pyroxene-rich lithologies, which would cause pyroxenites to generally have higher Ce and lower H₂O/Ce than peridotites.

This model can be tested using multiple previously suggested geochemical tracers of pyroxenite vs. peridotite melting. For example, melts derived from a pyroxenite source are predicted to have lower SiO₂ content, higher CaO/Al₂O₃ ratios, lower Na/Ti ratios, and more radiogenic Pb-isotopic compositions than ambient mantle peridotite [Hauri, 1996; Putirka, 1999; Jackson and Dasgupta, 2008; Jackson et al., 2012]. If H₂O/Ce ratios track variations in source lithology, then H₂O/Ce ratios should correlate with these geochemical tracers of pyroxenite vs. peridotite melting. However, as previously discussed, H₂O/Ce ratios show no correlation with isotopic compositions within melts calculated from pyroxene or in global OIB melt inclusions and glasses. H₂O/Ce ratios of melts calculated from pyroxene phenocrysts, as well as global melt inclusions, glasses and MORB show no correlation with SiO₂ content, CaO/Al₂O₃ ratios, and Na/Ti ratios (Figure 12). These observations suggest that the global correlation between H₂O/Ce ratios and Ce content is not likely the result of mixing between low degree melts of a dominantly pyroxenite lithology and high degree melts of a dominantly peridotite lithology, as previously suggested by Jackson et al [2015].

Alternatively, the negative global correlation between H₂O/Ce ratios and Ce content may be the result of H₂O loss via degassing processes. Glasses from Tuvalu, Society, Pitcairn, and Samoa span the largest range in Ce content within the global data set, from ~50 ppm to greater than 300 ppm. If H₂O were behaving as expected for a conserved incompatible element, then samples with the lowest Ce content should also

have the lowest H₂O content and vice versa. However, glasses from these localities all have consistently upper limits on H₂O of ~1.5 to 2 wt%. For example, some glasses from Samoa have Ce concentrations between 60 and 80 ppm and H₂O concentrations between 1 and 2 wt%. In contrast some glasses from Tuvalu have Ce concentrations above 300 ppm, but also H₂O concentrations between 1 and 2 wt %. Additionally, H₂O should correlate with alkalinity, in which high degree melts (tholeiitic basalts) should have higher H₂O and Ce concentrations than low degree melts (alkali basalts). Although Ce shows a positive correlation with alkalinity, H₂O does not. Therefore, the constant H₂O content observed in global OIB glasses, as well as the negative global correlation between H₂O/Ce ratios and Ce content may be the result of H₂O loss via degassing processes. In the following section we discuss the evidence and implications of H₂O loss via magma degassing.

6.5 Degassing Models for global OIB melt inclusions and glasses

Previous studies have suggested various mechanisms for H₂O and CO₂ loss in magmas (e.g. open and closed system degassing). In open system degassing models, each individual gas bubble that is formed immediately leaves the system. During degassing in natural systems, the solubility of CO₂ decreases more drastically than H₂O until very low pressures (< ~10 MPa). Therefore, as magmas ascend, they will lose CO₂ more rapidly than H₂O, which will then increase the H₂O/CO₂ ratio in the magma. Therefore, previous studies have argued that little H₂O loss occurs during open system degassing until pressures between 10 and 50 MPa [Dixon et al., 1995; Dixon, 1997; Jackson et al., 2015]. In closed system degassing models, individual gas bubbles do not leave the system until eruption and the concentrations of CO₂ and H₂O of the gas bubbles constantly reequilibrates during magma ascent in order to maintain equilibrium with the ascending

magma. Similar to open system degassing, the vapor has a high $\text{CO}_2/\text{H}_2\text{O}$ ratio relative to the melt at high pressures. However, the increase of H_2O in the vapor during ascent is more pronounced than in open system degassing models because as the melt loses both H_2O and CO_2 , the $\text{CO}_2/\text{H}_2\text{O}$ ratio in the vapor decreases and thus increases the amount of H_2O in the vapor. Therefore, this model suggests that at relatively low pressures (between 10 and 50 MPa), significant H_2O loss can occur [Dixon, 1997; Workman et al., 2006; Kendrick et al., 2014; Jackson et al., 2015].

Because both open and closed system degassing models predict little H_2O loss, but do predict significant CO_2 loss at high pressures, there should not be a correlation between CO_2 and H_2O until pressures between 10 and 50 MPa depending upon initial CO_2 concentrations. Glasses from Tuvalu, Pitcairn, and Samoa show no correlation between CO_2 and H_2O regardless of eruption pressures, which are estimated to be between ~10 and 60 MPa. Additionally, based on their estimated initial CO_2 content, open and closed system degassing models suggest that these glasses have not lost any primary magmatic H_2O . However, melt inclusions from Mangaia and the Azores directly contradict the assumption that CO_2 and H_2O should not correlate at pressure above 10 to 50 MPa. Mangaia melt inclusions from whole rock MGA-B-25 and MGA-B-47 show a rough positive correlation between CO_2 and H_2O for inclusions with saturation pressures between 10 and 50 MPa. Additionally, melt inclusions from the Azores have saturation pressures ranging from ~90 to 450 MPa and also show a strong positive correlation between CO_2 and H_2O . Because open and closed system degassing models cannot explain the behavior of CO_2 and H_2O in these systems, it is important to evaluate what other processes can.

MeTrich et al. [2011] and [2014] suggested that the correlation between CO_2 and H_2O within melt inclusions from the Azores could be the result of CO_2 rich vapors

generated at great depths ($> \sim 500$ MPa) that percolate through the volcanic system prior to eruption. As the CO_2 rich vapors generated by melts at greater depths, with high $\text{CO}_2/\text{H}_2\text{O}$, percolate through shallower melts; the $\text{CO}_2/\text{H}_2\text{O}$ ratio of the shallow melts will increase in order to maintain equilibrium. As this occurs, the melt will evolve along an isobar at a given pressure. Then as the melt begins to ascend, and thus decrease in pressure, the melts will evolve along an isopleth if CO_2 rich vapors with high $\text{CO}_2/\text{H}_2\text{O}$ are continuing to percolate through the melt, thus increasing the $\text{CO}_2/\text{H}_2\text{O}$ of the melt. We will refer to this model as “sparging”.

In addition to the Azores melt inclusion studies, sparging has also been used to explain the correlation between CO_2 and H_2O in melt inclusions from Mt. Etna [Spillaert et al., 2006]. CO_2 and H_2O concentrations of melt inclusions from these studies [MeTrich et al., 2011 and 2014; Spillaert et al., 2006] do not fall along either open or closed system degassing trends. Using the sparging model, melt inclusions from these studies evolve along respective isobars until they are in equilibrium with the $\text{CO}_2/\text{H}_2\text{O}$ ratio of the vapor generated at depth. Then, as the melt begins to ascend, which we assumed based on the wide range of melt inclusion entrapment pressures from these studies (~ 87 to 470 MPa), the melts will evolve along an isopleth of constant $\text{CO}_2/\text{H}_2\text{O}$ as long as the CO_2 rich vapor generated from greater depths continues to percolate through the melt. This suggests that the magma chambers in which these melt inclusions derive likely became oversaturated in CO_2 due to the fluxing of a CO_2 -rich vapor from greater depths.

If sparging is the dominant control of CO_2 and H_2O reported in global OIB glasses and melt inclusions, then OIB sources should be CO_2 -rich. In fact, Saal et al. [1998] reported carbonate globules in melt inclusions from Mangaia. They suggested that the presence of this phase directly indicates a CO_2 -rich magma in the Cook-Austral chain. Dupuy et al. [1992] suggested that the variable and unusually high Zr/Hf ratios reported

in global oceanic basalts represents source heterogeneities caused by carbonatitic metasomatism. This evidence is also consistent with work by Hauri et al. [1993], which suggested that trace element compositions of clinopyroxene, spinel, and apatite in peridotite xenoliths from Savai'i, Samoa and Tubuai, Australs were consistent with formation in carbonatitic melts. Hauri et al. [1993] suggested that this evidence, in conjunction with isotopic variations within these xenoliths, further supports the hypothesis that HIMU and EM-2 represent recycled oceanic crust and sediments. There are numerous other studies that also report evidence in support of carbon rich OIB melts. For example, Nuemann et al. [2002] suggested that mantle xenoliths from Tenerife, Canary Islands show evidence for metasomatism generated silicic carbonatite melts. Other studies have also shown evidence for metasomatism generated silicic carbonatite melts in mantle xenoliths from Lanzarote, Canary Islands [Siena et al., 1991; Nuemann et al., 1995].

Because melt inclusions from various OIB localities fit along isopleths of constant $\text{CO}_2/\text{H}_2\text{O}$ ratios, it is vital that in the future researchers evaluate if melt inclusions or glasses from any locality have lost H_2O not only through open and closed system degassing, but also through sparging. Additionally, because sparging predicts significant H_2O loss at pressures below 400 MPa, previous estimates of $\text{H}_2\text{O}/\text{Ce}$ ratios in EM and HIMU mantle sources may be too low given that their saturation pressures are < 400 MPa. Therefore, previous studies, which have suggested that low $\text{H}_2\text{O}/\text{Ce}$ ratios in melt inclusions and glasses reflect a relatively “dry” source, should be reevaluated using pyroxene phenocrysts.

6.6 Estimating source H_2O content from pyroxene phenocrysts

Because global OIB glasses show evidence of significant CO₂ and H₂O loss via a sparging model, OIB glasses are likely not reliable proxies for pre-eruptive magmatic H₂O contents. Additionally, because melt inclusions show evidence for post-entrapment hydrogen diffusion, they are also not reliable proxies for pre-eruptive magmatic H₂O contents. Therefore, because previous studies have estimated the amount of H₂O returned to the deep mantle via H₂O/Ce ratios of both melt inclusions and glasses, the amount of H₂O returned to the deep mantle may be underestimated.

Therefore, we proposed that clinopyroxene phenocrysts offer a more robust proxy for pre-eruptive magmatic H₂O contents than melt inclusions and glasses. However, based on the observation that Ce behaves as expected for a conserved incompatible element, and H₂O does not, we suggest estimating magmatic H₂O content from calculated melts with <100 ppm Ce. In doing so, HIMU melts from this study have H₂O/Ce ratios ranging from 111 to 316 ppm, and an average H₂O/Ce ratio of 222 (similar to that H₂O/Ce ratios reported by Cabral et al. [2014]). Assuming the same concentration of Ce in the HIMU source as Cabral et al. [2014] (2.2 ppm), estimated average magmatic H₂O from pyroxene phenocrysts is 487 ppm. Melts with isotopic compositions within the EM-2 field from this study have H₂O/Ce ratios ranging from 64 to 409, and an average H₂O/Ce ratio of 185. Assuming a source Ce concentration of 1.92 ppm [Workman et al., 2004], estimated average magmatic H₂O from pyroxene phenocrysts is 355 ppm. Given that H₂O loss can still occur in clinopyroxene phenocrysts, estimates of pre-eruptive magmatic H₂O content from melts inferred from pyroxene should be considered a minimum.

In future studies it would be advantageous to compare H₂O concentrations of clinopyroxene-hosted melt inclusions to olivine-hosted melt inclusions. Based on findings from this study, as well as that of Hirschmann et al. [2005], Warren and Hauri

[2014] and Bucholz et al. [2013], we expect that clinopyroxene-hosted melt inclusions would likely not lose H₂O post-entrapment, and therefore have similar H₂O concentrations as melts calculated from pyroxene phenocrysts. If these expectations prove to be true, then clinopyroxene-hosted melt inclusions would be the most ideal proxies for determining pre-eruptive magmatic H₂O content because they also record CO₂ content. With both H₂O and CO₂ from pyroxene-hosted melt inclusions, we can better understand global degassing processes. Furthermore, because pyroxene phenocrysts do show a correlation between H₂O content and phenocryst size, larger pyroxene phenocrysts or pyroxene melt inclusions are likely to more accurately record primary melt compositions. Until future studies of H₂O contents in pyroxene-hosted melt inclusions are conducted, we believe that clinopyroxene phenocrysts are the most robust proxy for pre-eruptive magmatic H₂O contents.

Chapter 7: Conclusions

Based on major, trace, and volatile compositions of pyroxene phenocrysts from the Cook-Austral Islands, we conclude that:

- Olivine-hosted melt inclusions are susceptible to post-entrapment hydrogen diffusion and therefore are not reliable proxies for pre-eruptive magmatic H₂O contents.
- Global OIB glasses show evidence of significant CO₂ and H₂O loss via a sparging model, in which CO₂-rich vapors generated at high pressures percolate into magma chambers at lower pressures. This process results in degassing trends that approach isopleths of constant CO₂/H₂O. Therefore, OIB glasses are also likely not reliable proxies for pre-eruptive magmatic H₂O contents.
- Because previous studies have estimated the amount of H₂O returned to the deep mantle via H₂O/Ce ratios of both melt inclusions and glasses, the amount of H₂O returned to Earth's mantle may be underestimated.
- Clinopyroxene phenocrysts offer a new and more robust proxy for pre-eruptive magmatic water contents than melt inclusions and glasses
- We estimate that melts calculated from pyroxene phenocrysts, from this study, with isotopic compositions within the HIMU field, have an average magmatic H₂O content of ~487 ppm. This estimate is very similar to the estimate of Cabral et al. [2014], which suggested that the HIMU source had a H₂O content of ~440 ppm.
- We estimate that melts calculated from pyroxene phenocrysts, from this study, with isotopic compositions within the EM-2 field from this study have an average magmatic H₂O content of ~355 ppm, which is significantly higher than previous estimates for EM (e.g. 160 ppm from Bizimis and Peslier [2015]).

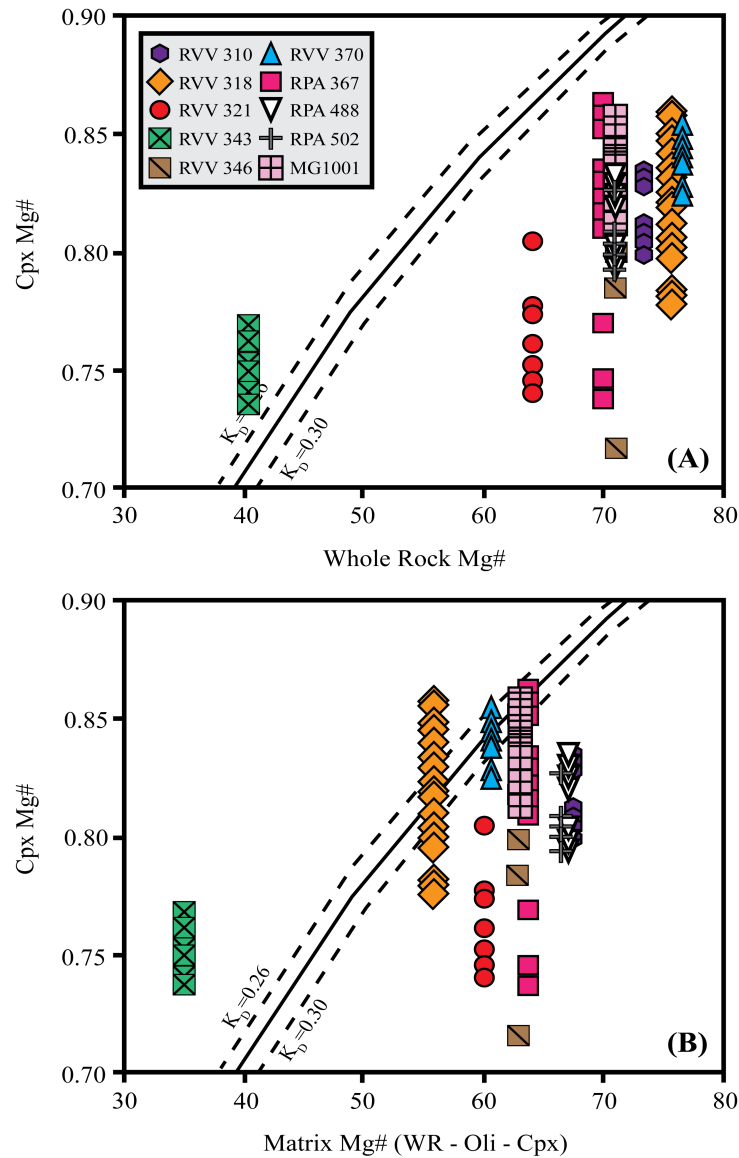


Figure 1: (a) Cpx phenocryst Mg# vs. whole rock Mg#. Solid and dashed black lines represent the expected Mg# of a melt in equilibrium with cpx assuming a K_D value of 0.28 ± 0.02 [McKenzie and O’Nions, 1991] (b) Cpx Mg# vs. host melt Mg#. Melt compositions were calculated by subtracting out the observed abundance of phenocrysts from whole rocks. Whole rock compositions from Woodhead et al. [1996], Lassiter et al. [2003], and Chan et al. [2009].

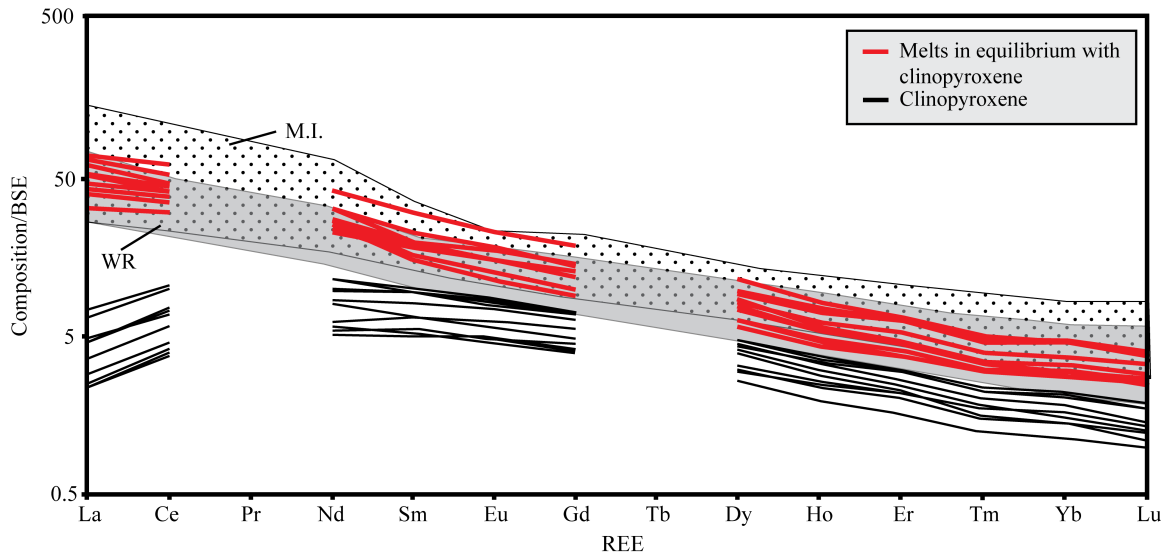


Figure 2: REE abundances of cpx phenocrysts from Raivavae, Rapa, and Mangaia (Cook-Austral Islands). Compositions normalized to Bulk Silicate Earth (BSE) values from McDonough and Sun [1995]. Grey field represents whole rock compositions (see Figure 1 for references). Open field with solid black dots are melt inclusion compositions from Lassiter et al. [2002].

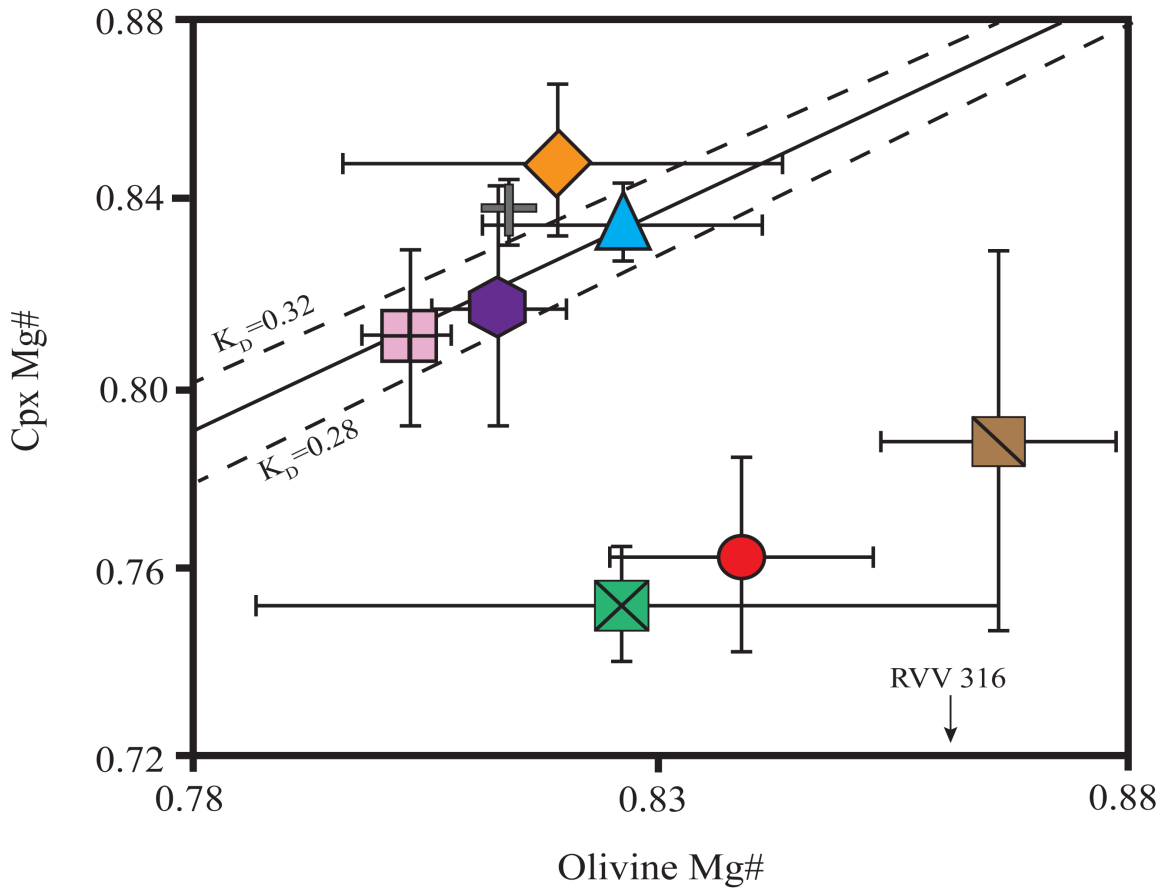


Figure 3: Average cpx Mg# vs. olivine Mg#. Samples RVV 310, RVV 318, RVV 370 and MG1001 fall along the equilibrium line, which suggests that both phases grew in equilibrium. Several other samples (e.g. RVV 321) do not fall along the equilibrium line and olivine phenocrysts are likely more primitive than pyroxene phenocrysts. Phase equilibrium line was generated assuming a cpx (Fe/Mg) K_D value of 0.28 [McKenzie and O’nions, 1991] and an olivine (Fe/Mg) K_D value of 0.3 ± 0.02 [Ford et al. 1983; Hauri 1996].

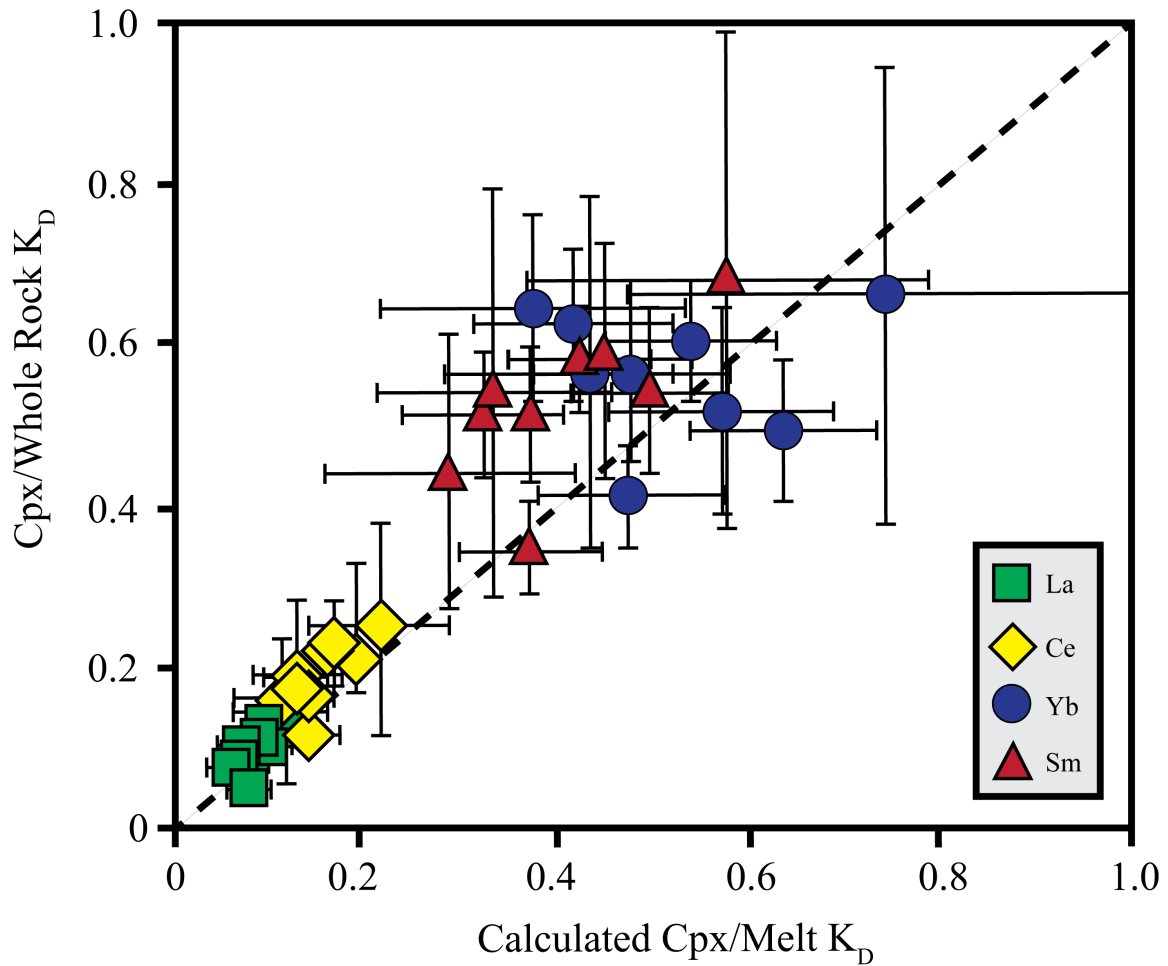


Figure 4: Average calculated cpx/whole rock K_D vs. calculated cpx/melt K_D generated from BigD. Average K_D values for both all four elements fall along the 1:1 line within error. This suggests that K_D values for all four elements are likely not overestimated by BigD.

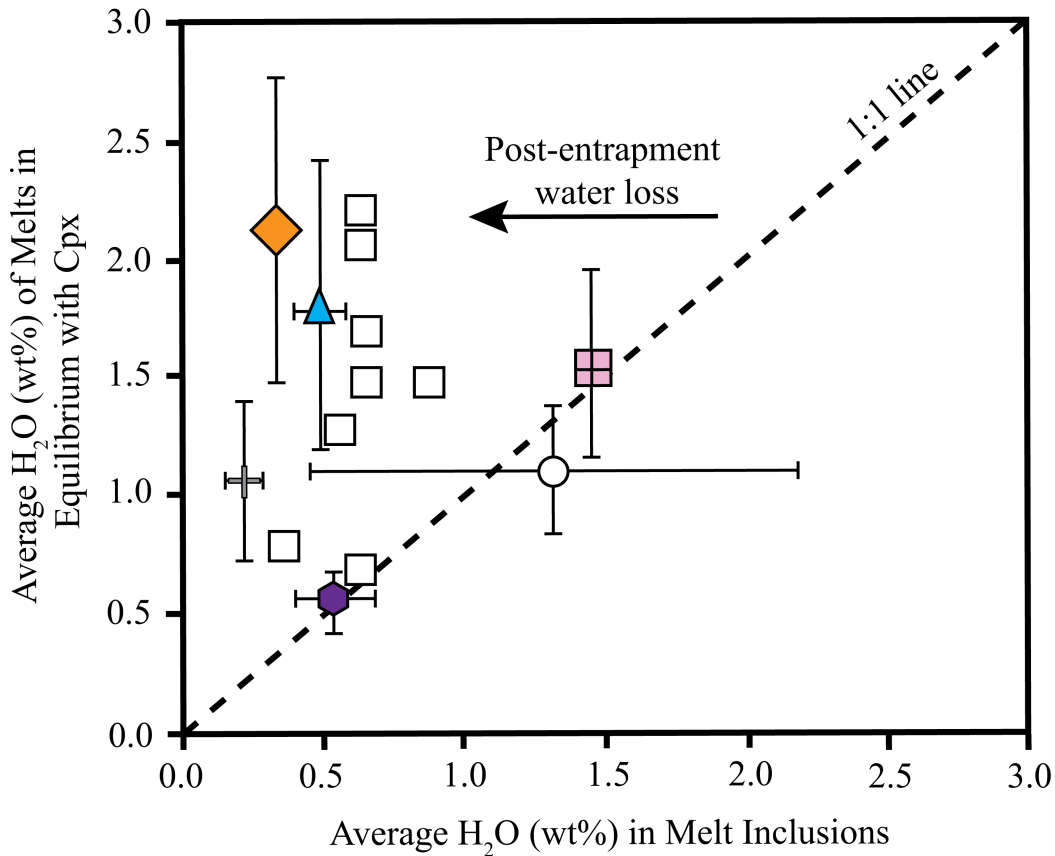


Figure 5: Average H₂O (wt%) of melts in equilibrium with cpx vs. average H₂O (wt%) of olivine-hosted melt inclusions. *From this study:* Two samples (RVV 310 and MG1001) fall along the 1:1 line, which suggests that melt inclusions from these samples have likely not lost H₂O post-entrapment. Melt inclusions from all other samples have systematically lower H₂O content than melts calculated from cpx. This suggests that melt inclusions from these samples have likely lost H₂O post-entrapment. Austral Island melt inclusion data from Lassiter et al. [2002]. Mangaia (MG1001) melt inclusion data from Cabral et al. [2014]. *Other studies:* Black outlined square symbols represent H₂O concentrations of both melts calculated from clinopyroxene phenocrysts and olivine-hosted melt inclusions from San Miguel, Azores [Turner et al., 2017]. Melt inclusions from this study also have systematically lower H₂O concentrations than melts calculated from pyroxene, which further supports post-entrapment H₂O loss in melt inclusions. The black outlined circle represents H₂O concentrations of olivine-hosted melt inclusions from Longpre et al. [2017] and H₂O concentrations of melts in equilibrium with cpx from Weis et al. [2015], both from the Canary Islands. For this symbol, error bars reflect 1σ standard deviation of reported data from each data set. Average H₂O concentrations from each data set fall near the 1:1 equiline and suggest that, on average, olivine-hosted melt inclusions from the Canary Islands have not lost H₂O post-entrapment.

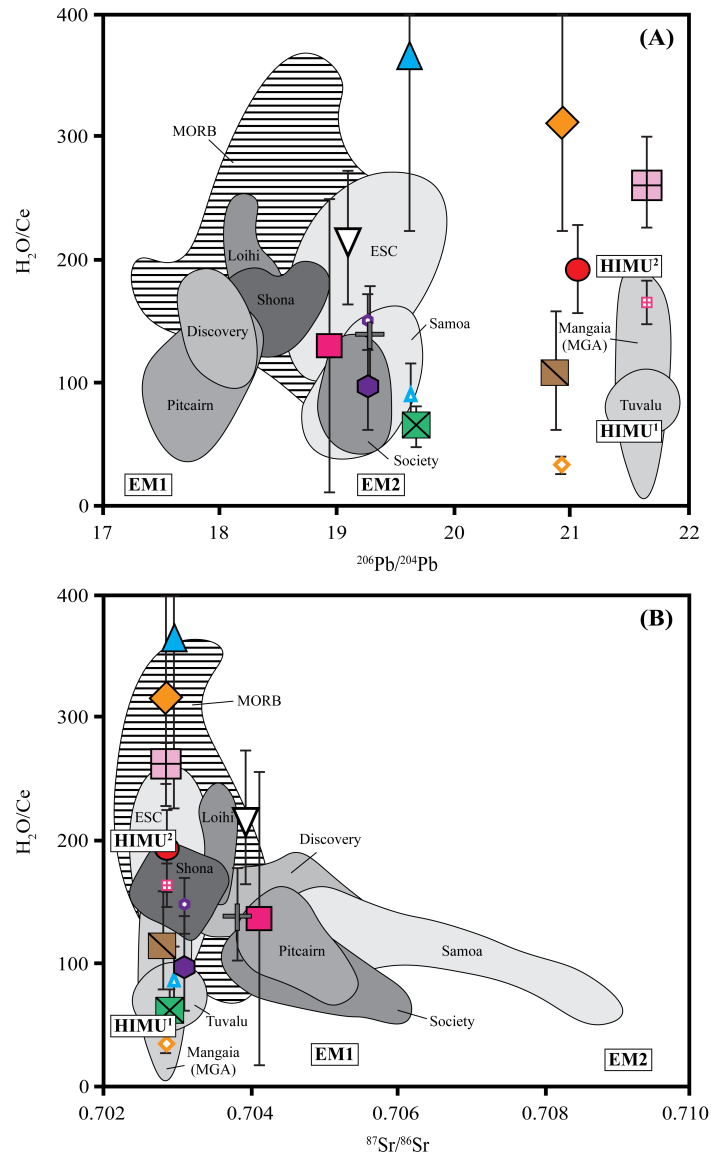


Figure 6: Whole rock $^{206}Pb/^{204}Pb$ vs. average H_2O/Ce ratios of melts in equilibrium with cpx, olivine-hosted melt inclusions, and global OIB glasses and MORB. Error bars represent standard deviation of mean. “HIMU¹” H_2O/Ce estimate from Cabral et al. [2014], “HIMU²” estimate from Jackson et al. [2015]. Sample information: MORB from Dixon [2002] and Kendrick et al. [2017] (and references therein); Azores from MeTrich et al. [2014]; Pitcairn and Society from Kendrick et al. [2014]; Mangaia (MGA and MG1001) from Cabral et al. [2014]; Tuvalu glasses from Jackson et al. [2015]; Discovery and Shona from Dixon et al. [2002]; Samoa from Workman et al. [2006]; Santiago from Koleszar et al. [2009]; Loihi from Dixon and Clague [2001]; ESC from Simmons et al. [2002].

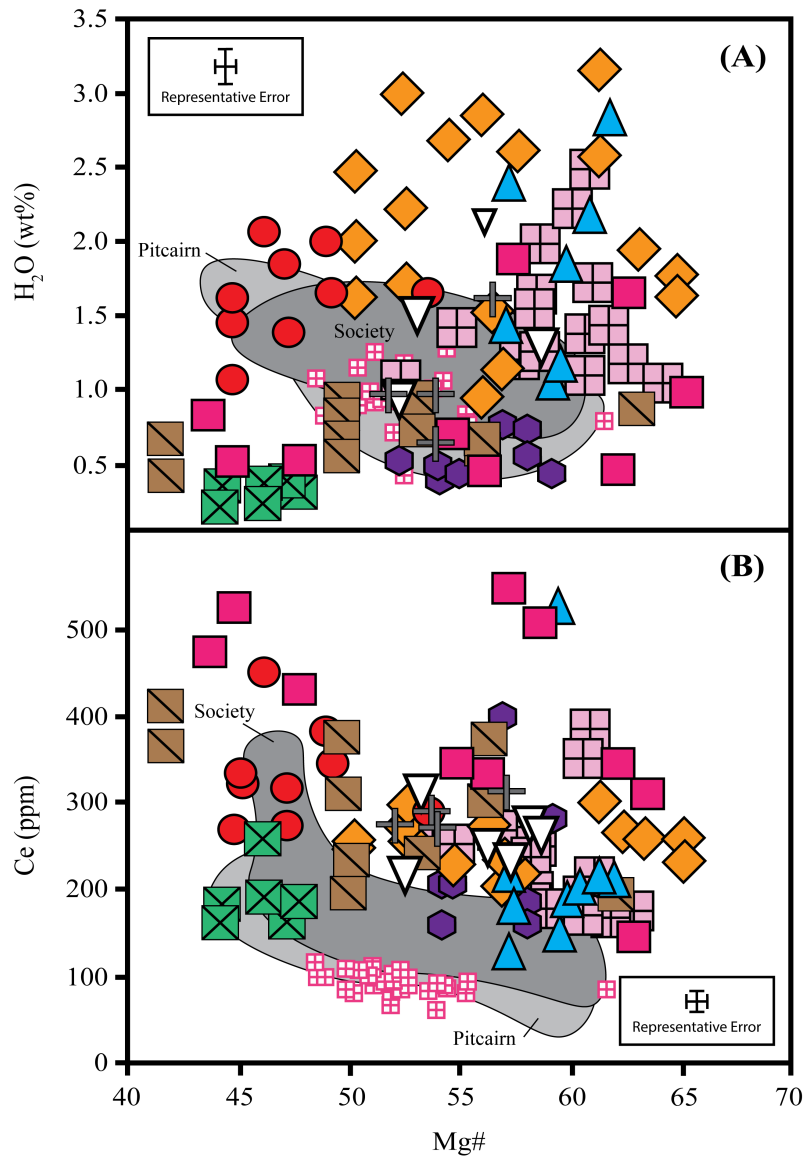


Figure 7: (A) Calculated H₂O contents of melts in equilibrium with cpx vs. calculated Mg# of melts in equilibrium with cpx. Overall there is a weak correlation between magmatic H₂O and Mg#. (B) Calculated Ce contents of melts in equilibrium with cpx vs. calculated Mg# of melts in equilibrium with cpx. Overall there is a correlation between magmatic Ce content and Mg#.

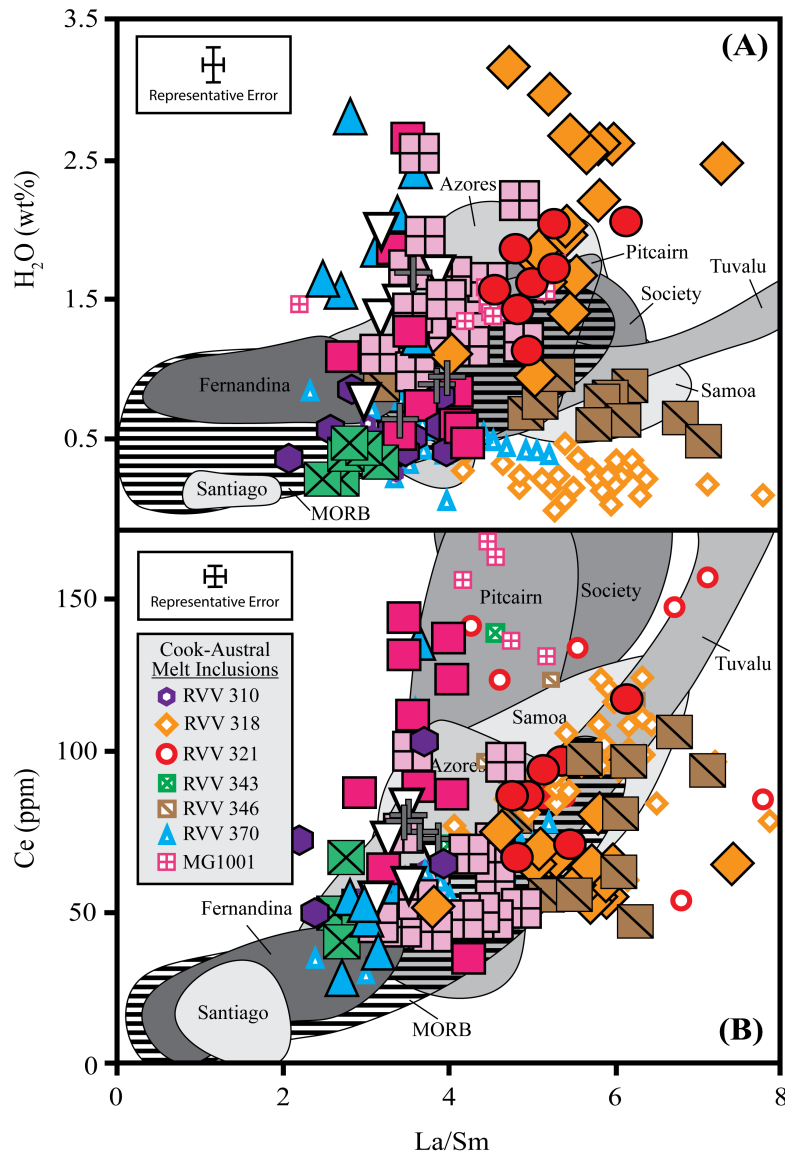


Figure 8: (A) Calculated H₂O contents of melts in equilibrium with cpx vs. calculated La/Sm ratios of melts in equilibrium with cpx. There is no observed correlation between magmatic H₂O and La/Sm. Global OIB glasses and melt inclusions (grey fields) also show no correlation between H₂O and La/Sm. However, global MORB (field of dashed black and white lines) do show a correlation between H₂O and La/Sm. (B) Calculated Ce contents of melts in equilibrium with cpx vs. calculated La/Sm of melts in equilibrium with cpx. Overall there is a positive correlation between magmatic Ce content and La/Sm ratios. Global OIB glasses and melt inclusions, as well as global MORB also show a positive correlation between Ce content and La/Sm ratios. These observations suggest that Ce is behaving as expected for a conserved incompatible element, but H₂O is not. See Figure 6 for OIB and MORB references.

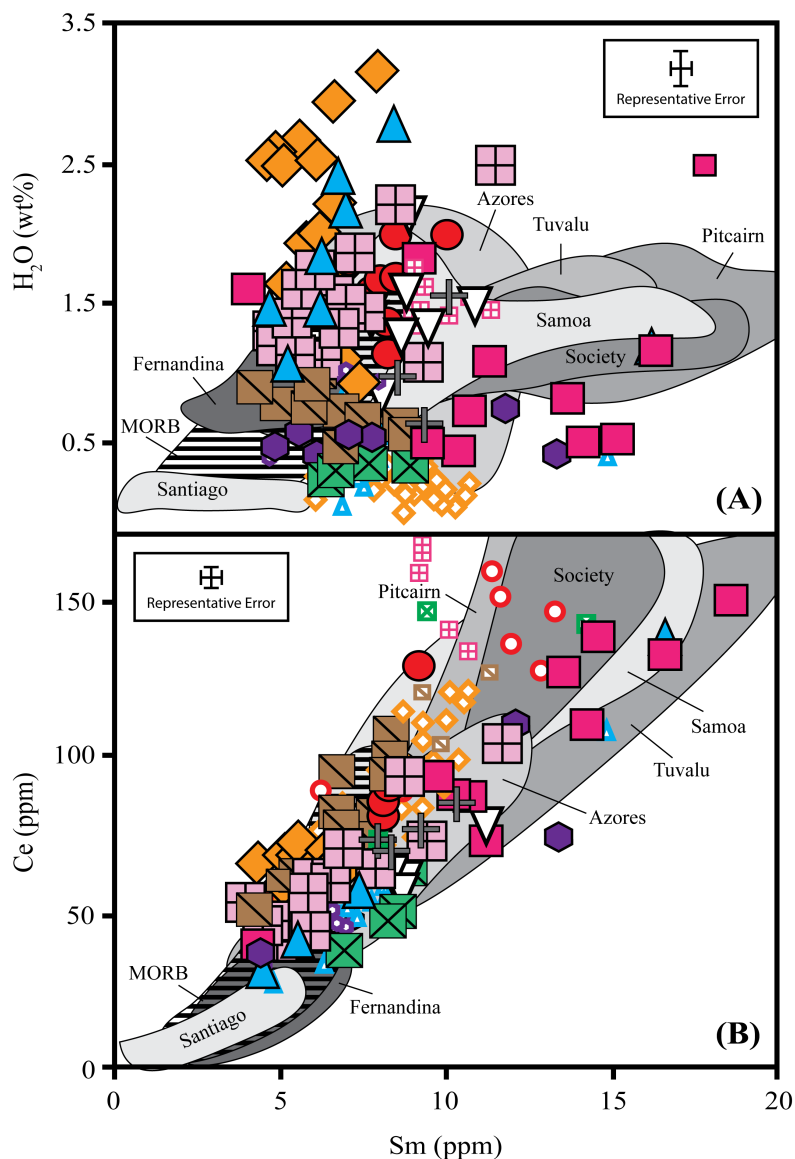
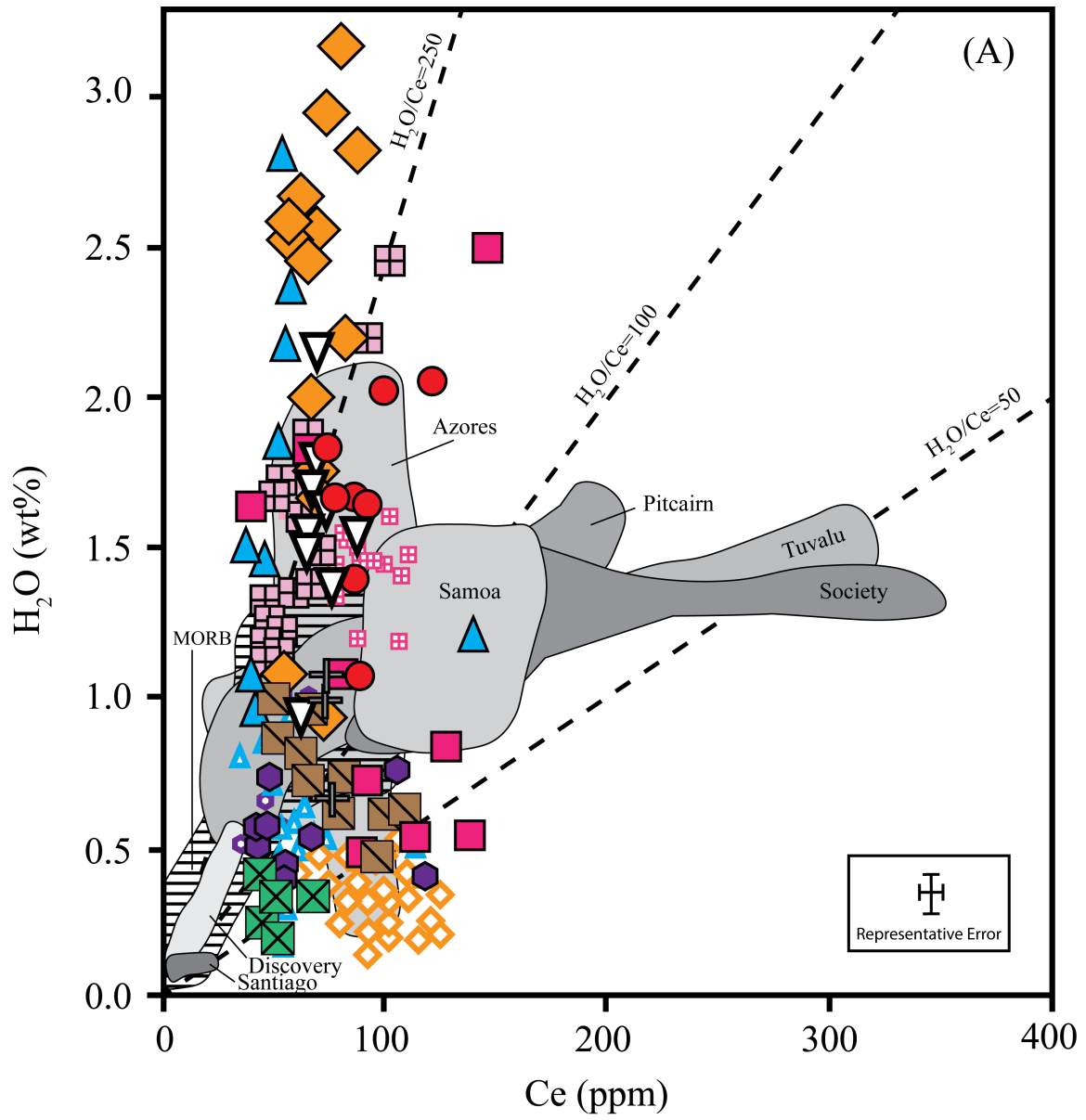


Figure 9: (A) Calculated H_2O of melts in equilibrium with cpx vs. calculated Sm of melts in equilibrium with cpx. There is no observed correlation between magmatic H_2O and Sm. Global OIB glasses and melt inclusions (grey fields) also show no correlation between H_2O and Sm. However, global MORB (field of dashed black and white lines) do show a correlation between H_2O and Sm. (B) Calculated Ce contents of melts in equilibrium with cpx vs. calculated Sm of melts in equilibrium with cpx. Overall there is a positive correlation between magmatic Ce content and Sm. Global OIB glasses and melt inclusions, as well as global MORB also show a positive correlation between Ce content and Sm content. These observations further suggest that Ce is behaving as expected for a conserved incompatible element, but H_2O is not. See Figure 6 for OIB and MORB references.



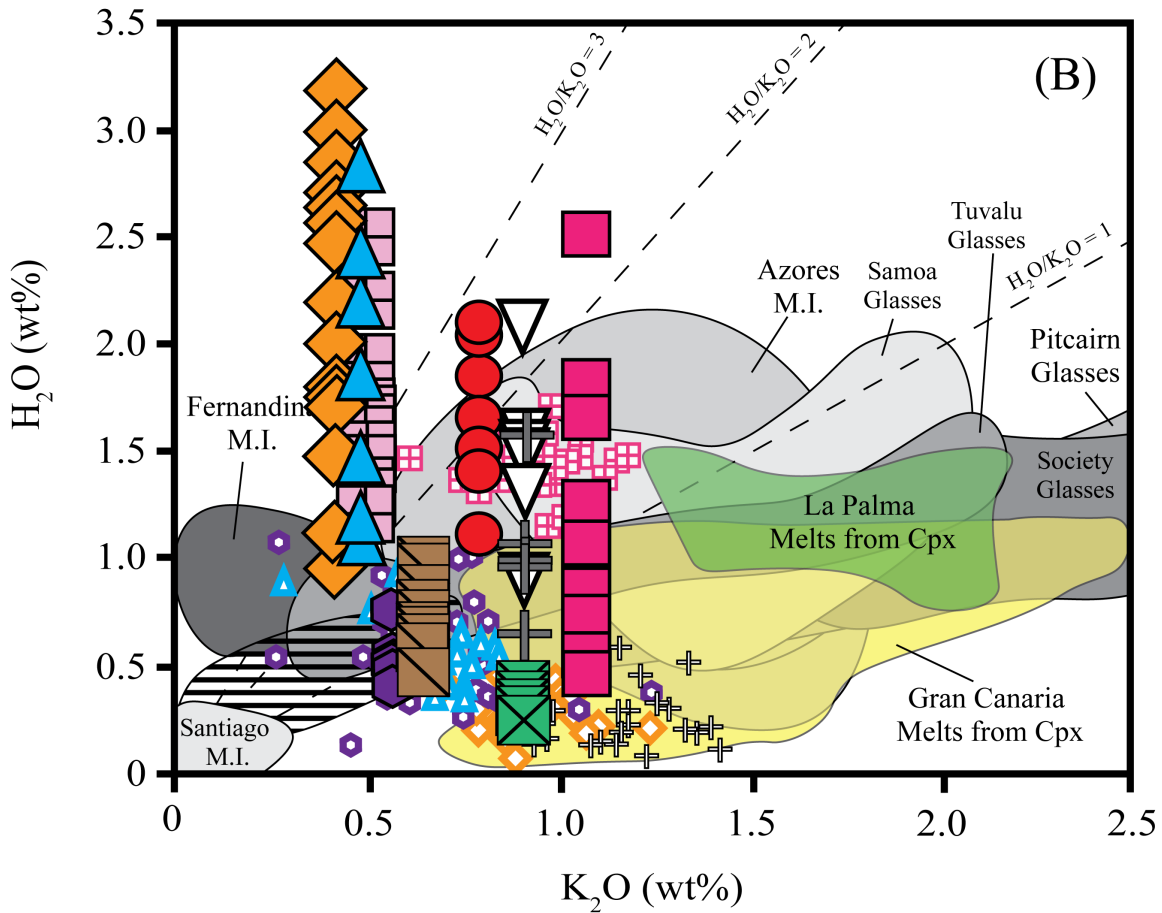


Figure 10: (A) H_2O (wt%) vs. Ce (ppm) of calculated melts from the Cook-Austral Islands, and their corresponding melt inclusions, as well as global OIB and MORB. H_2O concentrations of melts calculated from pyroxene extend to much higher values than corresponding melt inclusions. Glasses from Pitcairn, Tuvalu and Society extend to the highest Ce content and to very low H_2O/Ce ratios. Figure modified from Cabral et al. [2014] and Jackson et al. [2015]. (B) H_2O (wt.%) of calculated melts from the Cook-Austral Islands, and their corresponding melt inclusions, as well as calculated melts from the Canary Islands vs. corresponding whole-rock K_2O (wt.%). Measured H_2O and K_2O of global OIB glasses, melt inclusions, and MORB are also plotted in this figure. H_2O concentrations of melts calculated from pyroxene (this study) extend to much higher values than the global data set for a given K_2O value. See Figure 6 for OIB and MORB references. Canary Island H_2O concentrations of melts calculated from pyroxene and whole rock K_2O from Weis et al. [2015] and references therein. A sub-set of Azores H_2O and K_2O concentrations of olivine-hosted melt inclusions are from Turner et al. [2017].

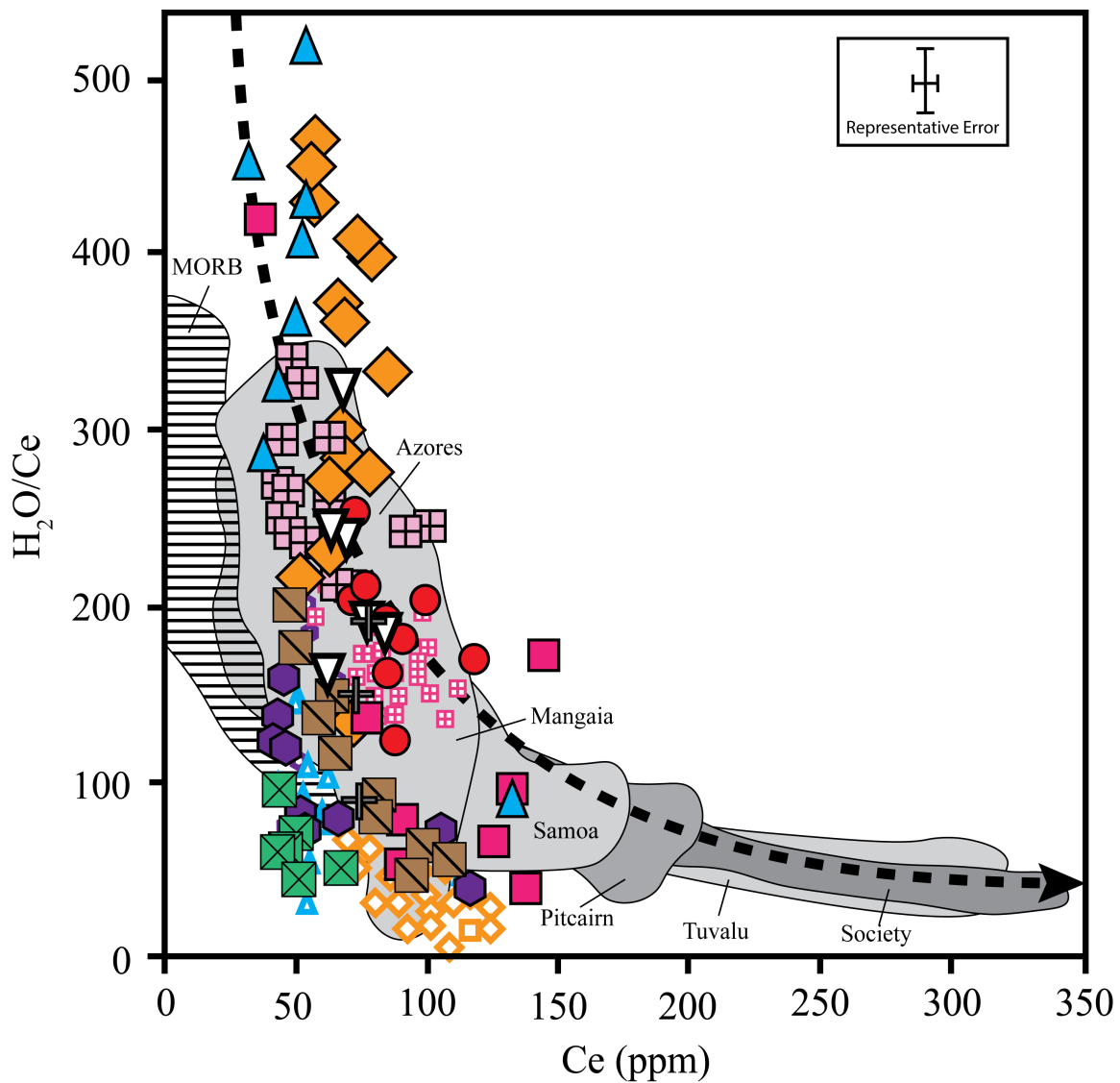


Figure 11: H₂O/Ce vs. Ce (ppm) of calculated melts from the Cook-Austral Islands, and their corresponding melt inclusions, as well as global OIB and MORB. This negative correlation has been attributed to mixing between pyroxenite and peridotite lithologies [Jackson et al., 2015]. The black dashed line represents modeled H₂O/Ce ratios with a constant H₂O concentration of 1.5 wt% and an increasing Ce content from 2 to 350 ppm. See Figure 6 for OIB and MORB references. Figure modified from Jackson et al. [2015].

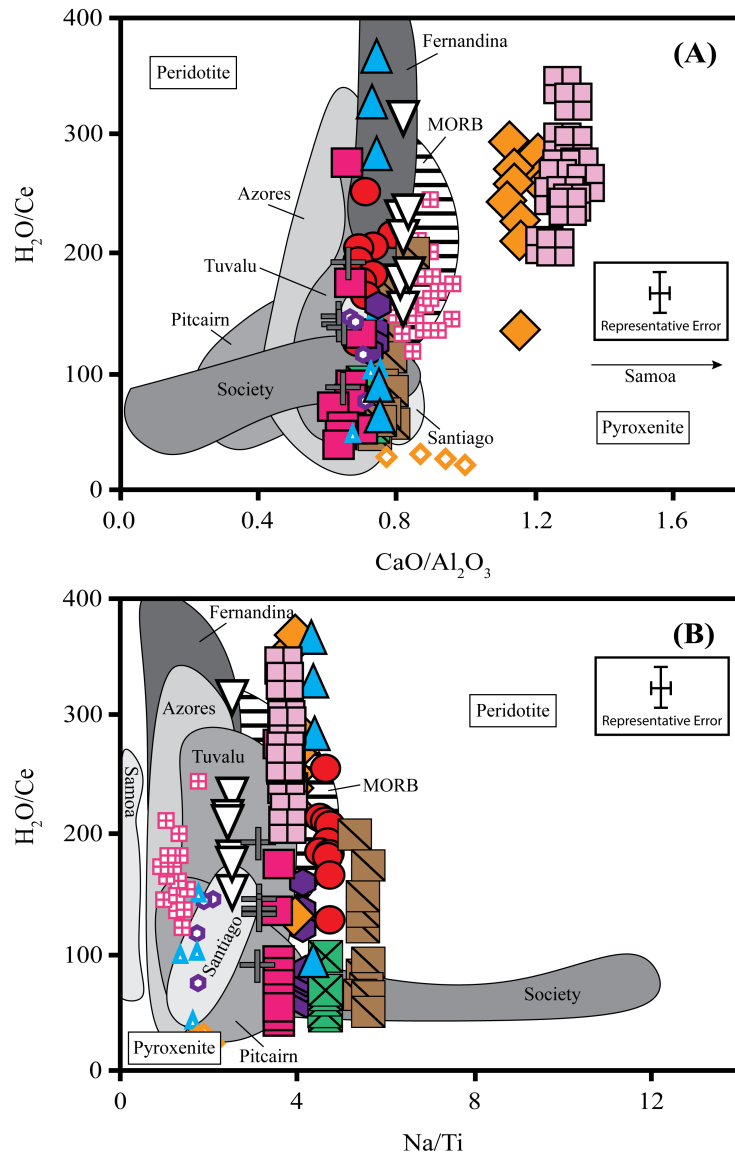


Figure 12: (A) H₂O/Ce vs. CaO/Al₂O₃ of calculated melts from the Cook-Austral Islands, and their corresponding melt inclusions, as well as global OIB. (B) H₂O/Ce vs. Na/Ti of calculated melts from the Cook-Austral Islands, and their corresponding melt inclusions, as well as global OIB. See Figure 6 for OIB references. H₂O/Ce ratios of pyroxenite and peridotite fields are based on work from Bizimis and Peslier [2015], who suggested that Ce has a higher partition coefficient than H during crystallization of pyroxenite lithologies. CaO/Al₂O₃ values of pyroxenite and peridotite fields are based on work from Jackson and Dasgupta [2008] and Jackson et al. [2012], who suggested pyroxenite lithologies have high CaO/Al₂O₃ values whereas peridotite lithologies have low values. Na/Ti values of pyroxenite and peridotite follow the model outlined in Putirka [1999].

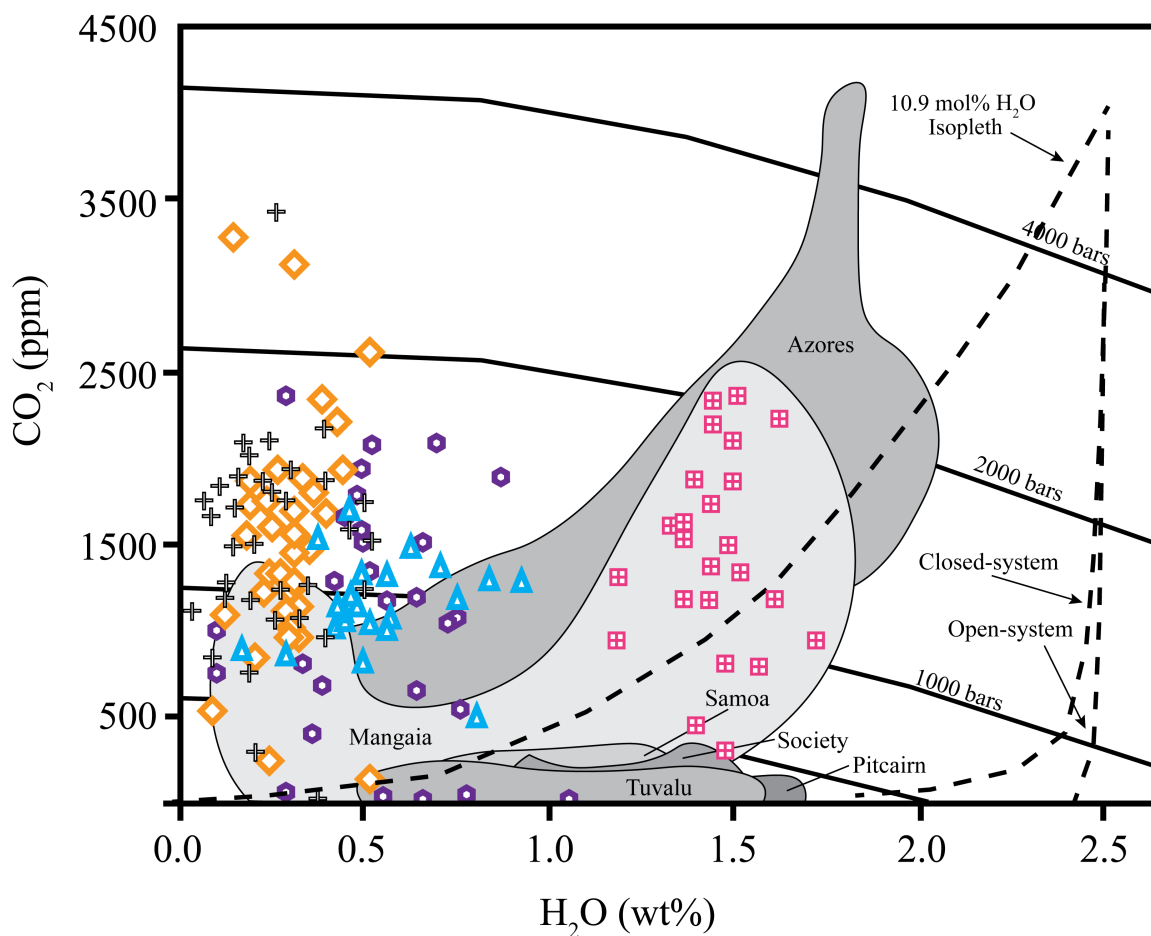


Figure 13: CO₂ (ppm) vs. H₂O (wt%) of melt inclusions from the Cook-Austral Islands, as well as glasses and melt inclusions from other OIB. Dashed black lines represent open and closed system degassing (with 0 wt% exsolved vapor), as well as an isopleth with a fixed vapor composition of 10.9 mol% H₂O and 89.1 mol% CO₂ (CO₂/H₂O=8.17). Degassing paths were generated from the program VolatileCalc_2.0. Inputs for each model were 49 wt% SiO₂, 2.5 wt% H₂O, 4000 ppm CO₂, and 1250 °C. See Figure 6 for sample information. See Figure 6 for OIB references.

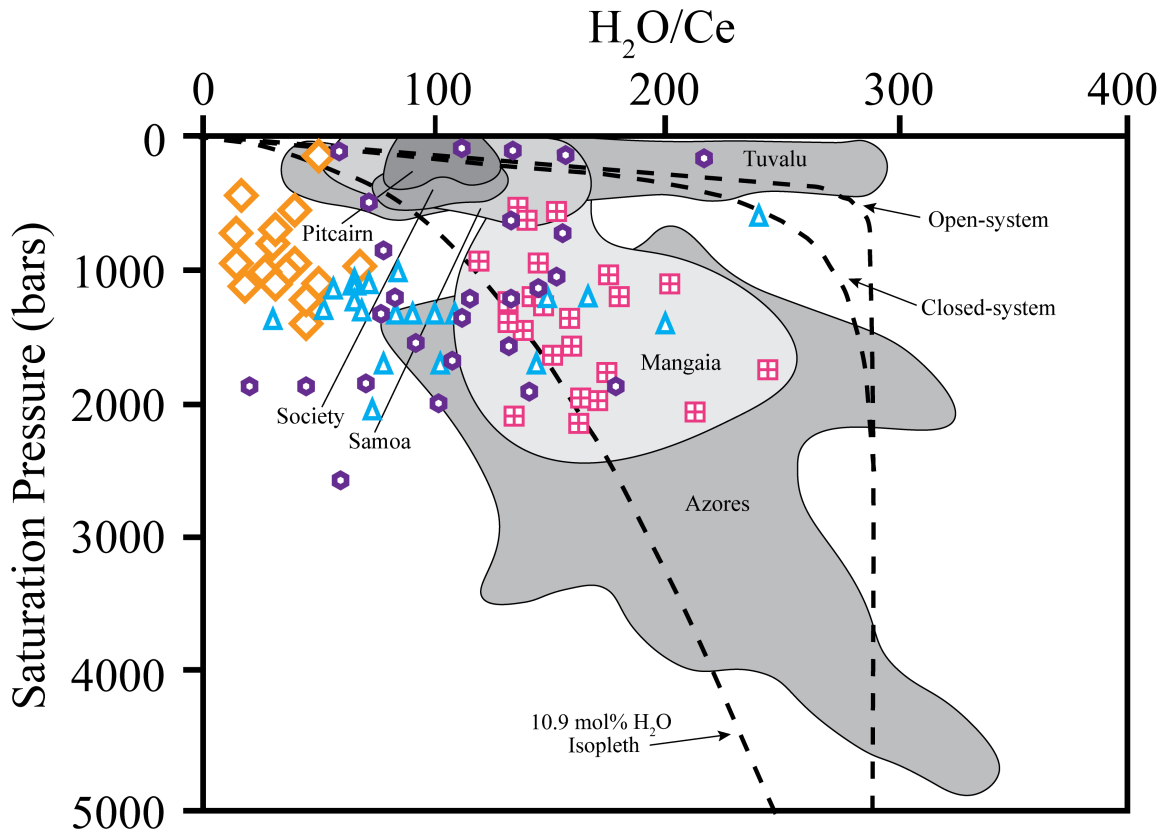


Figure 14: Saturation pressure vs. H_2O/Ce ratios of melt inclusions from the Cook-Austral Islands, as well as glasses and melt inclusions from other OIB. Dashed black lines represent open and closed system degassing (with 0 wt% exsolved vapor), as well as an isopleth with a fixed vapor composition of 10.9 mol% H_2O . Each model follows the same parameters outlined in Figure 14. Additionally, a constant Ce concentration of 83 ppm was assumed for each model based on H_2O/Ce ratio of 300 and 2.5 wt% H_2O . See Figure 6 for OIB references.

Table 1: Average major element compositions of clinopyroxene phenocrysts

	RVV 310	RVV 316	RVV 318	RVV 321	RVV 343	RVV 346
	n=9	n=1	n=18	n=9	n=6	n=11
SiO₂	49.63 (1.35)	46.17 -	48.79 (1.06)	46.33 (0.71)	49.04 (1.04)	47.13 (2.35)
TiO₂	0.95 (0.43)	2.13 -	1.29 (0.32)	1.95 (0.32)	1.31 (0.27)	1.88 (0.75)
Al₂O₃	5.33 (1.12)	8.20 -	5.76 (1.00)	8.78 (0.78)	5.07 (0.71)	7.41 (1.87)
Cr₂O₃	0.92 (0.21)	0.01 -	0.51 (0.28)	0.20 (0.17)	0.20 (0.03)	0.47 (0.28)
FeO	6.02 (0.23)	10.56 -	5.67 (0.64)	7.05 (0.52)	8.48 (0.37)	6.41 (0.90)
MnO	0.12 (0.03)	0.29 -	0.10 (0.02)	0.11 (0.02)	0.18 (0.02)	0.12 (0.03)
MgO	15.38 (0.92)	9.90 -	14.55 (0.86)	12.74 (0.62)	14.46 (0.32)	13.50 (1.48)
CaO	21.36 (0.83)	22.44 -	23.11 (0.38)	22.12 (0.27)	20.97 (0.21)	22.85 (0.35)
Na₂O	0.38 (0.07)	0.66 -	0.37 (0.06)	0.73 (0.09)	0.45 (0.04)	0.44 (0.06)
K₂O	0.01 (0.01)	0.00 -	- -	0.01 (0.01)	- -	0.01 (0.01)
NiO	0.03 (0.02)	- -	0.03 (0.02)	0.02 (0.02)	0.02 (0.01)	0.03 (0.02)
Total	100.11 (1.40)	100.36 -	100.19 (0.82)	100.01 (0.81)	100.19 (0.85)	100.22 (0.95)
Mg#	82 (1)	63 -	82 (2)	76 (2)	75 (1)	79 (4)
H₂O (ppm)	148 (29)	111 -	684 (198)	756 (100)	90 (13)	292 (61)
D_{H₂O}	0.03	0.04	0.03	0.05	0.03	0.04
Size (mm)	3.22	0.79	6.33	4.00	3.22	2.33

Table 1 (continued): Average major element compositions of clinopyroxene phenocrysts

	RVV 370	RPA 367	RPA 414	RPA 488	RPA 502	MG1001
	n=8	n=11	n=9	n=7	n=5	n=15
SiO₂ (wt%)	50.30	49.60	49.64	48.66	47.91	49.78
	(0.99)	(1.49)	(1.49)	(1.02)	(1.94)	(0.73)
TiO₂	0.98	1.42	1.30	1.70	2.04	1.06
	(0.25)	(0.58)	(0.46)	(0.21)	(0.35)	(0.26)
Al₂O₃	4.45	4.72	5.15	6.07	6.28	4.37
	(0.74)	(1.10)	(0.92)	(0.61)	(0.97)	(0.56)
Cr₂O₃	0.98	0.66	0.70	0.86	0.61	0.85
	(0.12)	(0.46)	(0.19)	(0.35)	(0.14)	(0.19)
FeO	5.50	6.15	5.62	5.86	6.12	5.27
	(0.31)	(1.34)	(0.31)	(0.47)	(0.30)	(0.25)
MnO	0.12	0.13	0.10	0.11	0.10	0.10
	(0.02)	(0.04)	(0.02)	(0.02)	(0.02)	(0.02)
MgO	15.82	15.11	15.29	14.87	14.45	15.41
	(0.40)	(1.17)	(0.74)	(0.28)	(0.51)	(0.65)
CaO	21.67	21.70	22.04	21.94	22.22	22.78
	(0.30)	(0.51)	(0.61)	(0.25)	(0.46)	(0.42)
Na₂O	0.37	0.42	0.40	0.42	0.47	0.37
	(0.08)	(0.06)	(0.09)	(0.03)	(0.03)	(0.04)
K₂O	0.00	0.00	0.00	0.01	-	0.00
	(0.00)	(0.00)	(0.00)	-	-	(0.00)
NiO	0.03	0.04	0.03	0.04	0.03	0.03
	(0.01)	(0.03)	(0.01)	(0.02)	(0.02)	(0.01)
Total	100.21	99.93	100.25	100.52	100.23	100.00
	(0.75)	(0.78)	(0.83)	(1.23)	(1.29)	(1.19)
Mg#	84	81	83	82	81	84
	(1)	(4)	(1)	(1)	(1)	(1)
H₂O(ppm)	425	263	271	498	382	404
	(122)	(138)	(106)	(84)	(80)	(71)
D_{H2O}	0.02	0.03	0.03	0.03	0.04	0.03
Size (mm)	5.56	2.78	4.89	2.44	4.11	6.33

Values in parentheses refer to 1 standard deviation from sample average.

“n=” refers to number of pyroxene grains analyzed from each sample.

“RVV” refers to whole rock samples from Raivavae Island; “RPA” refers to whole rock samples from Rapa Island; “MG” refers to whole rock samples from Mangaia.

$$\mathbf{Mg\#} = \frac{Mg}{(Mg+Fe)} * 100$$

$$\mathbf{Cr\#} = \frac{Cr}{(Cr+Al)} * 100$$

FeO* refers to total iron content ($\text{FeO}^* = \text{FeO} + \text{Fe}_2\text{O}_3$)

$D_{\text{H}_2\text{O}}$ refers to the calculated partition coefficient of H_2O via the methods from Hauri et al. [2006]: $D_{\text{H}_2\text{O}} = \left(0.326 * \frac{Al(IV)}{Total(IV)}\right) - 0.0016$

Size (mm) refers to the average of 10 rim-to-rim length measurements of pyroxene phenocrysts from each sample.

Table 2: Average trace element compositions of clinopyroxene phenocrysts

	RVV 310	RVV 316	RVV 318	RVV 321	RVV 343	RVV 346
Sr (ppm)	45.38 (13.31)	135.10 -	53.70 (5.37)	78.36 (11.26)	35.95 (1.62)	63.76 (12.18)
Y	8.69 (1.88)	15.78 -	9.18 (2.21)	12.88 (1.93)	12.62 (2.17)	13.13 (5.61)
Zr	23.76 (13.92)	144.40 -	36.69 (12.91)	53.76 (12.75)	27.13 (6.96)	69.30 (48.88)
Nb	0.17 (0.09)	2.49 -	0.44 (0.32)	0.73 (0.16)	0.16 (0.05)	0.83 (0.72)
Ba	0.03 (0.07)	1.74 -	0.24 (0.78)	0.14 (0.30)	0.00 (0.00)	0.14 (0.28)
La	1.50 (0.76)	9.24 -	3.06 (0.77)	4.32 (0.90)	1.62 (0.24)	4.76 (2.63)
Ce	6.24 (3.04)	34.50 -	11.37 (2.67)	16.59 (3.19)	7.01 (1.13)	17.31 (9.07)
Pr	1.08 (0.51)	5.42 -	1.86 (0.42)	2.69 (0.56)	1.23 (0.17)	2.78 (1.39)
Nd	6.41 (2.88)	26.80 -	9.98 (2.22)	14.61 (2.99)	7.64 (1.28)	14.46 (6.99)
Sm	2.03 (0.79)	6.67 -	2.70 (0.66)	4.03 (0.75)	2.68 (0.44)	3.92 (1.77)
Eu	0.73 (0.25)	1.99 -	0.86 (0.21)	1.32 (0.25)	0.94 (0.14)	1.27 (0.55)
Gd	2.26 (0.68)	5.44 -	2.56 (0.58)	3.83 (0.69)	3.05 (0.52)	3.72 (1.67)
Tb	0.34 (0.10)	0.75 -	0.36 (0.08)	0.54 (0.08)	0.46 (0.08)	0.54 (0.24)
Dy	2.07 (0.52)	4.19 -	2.19 (0.53)	3.17 (0.49)	2.91 (0.48)	3.16 (1.29)
Ho	0.37 (0.09)	0.69 -	0.38 (0.10)	0.54 (0.09)	0.52 (0.10)	0.56 (0.24)
Er	0.87 (0.21)	1.54 -	0.94 (0.23)	1.32 (0.20)	1.30 (0.21)	1.34 (0.56)
Tm	0.10 (0.02)	0.18 -	0.12 (0.03)	0.15 (0.02)	0.15 (0.03)	0.16 (0.07)
Yb	0.63 (0.12)	1.09 -	0.73 (0.19)	0.91 (0.16)	0.95 (0.14)	0.97 (0.42)
Lu	0.08 (0.02)	0.15 -	0.09 (0.02)	0.12 (0.02)	0.12 (0.02)	0.13 (0.06)

Table 2 (continued): Average trace element compositions of clinopyroxene phenocrysts

	RVV 370	RPA 367	RPA 414	RPA 488	RPA 502	MG1001
Sr (ppm)	41.99 (4.39)	68.62 (19.15)	59.77 (12.91)	71.92 (5.05)	82.78 (2.74)	50.06 (6.56)
Y	8.72 (1.15)	12.34 (4.68)	9.02 (2.36)	10.17 (1.76)	11.14 (1.10)	7.18 (1.03)
Zr	21.99 (5.17)	52.55 (31.83)	32.71 (13.88)	41.06 (9.79)	55.45 (8.96)	25.32 (8.79)
Nb	0.14 (0.04)	0.33 (0.18)	0.24 (0.22)	0.24 (0.05)	0.41 (0.05)	0.17 (0.09)
Ba	0.00 (0.01)	0.11 (0.21)	0.09 (0.19)	0.01 (0.03)	0.14 (0.23)	0.17 (0.38)
La	1.55 (0.38)	3.16 (1.58)	1.99 (0.86)	2.32 (0.42)	2.95 (0.35)	1.87 (0.53)
Ce	6.49 (1.45)	12.96 (6.47)	8.13 (2.93)	9.69 (1.48)	11.99 (1.44)	7.56 (1.89)
Pr	1.15 (0.26)	2.25 (1.14)	1.44 (0.50)	1.77 (0.30)	2.15 (0.27)	1.29 (0.30)
Nd	6.82 (1.42)	12.73 (6.19)	8.31 (2.87)	10.73 (1.80)	12.46 (1.42)	7.15 (1.38)
Sm	2.24 (0.34)	3.95 (1.84)	2.55 (0.78)	3.27 (0.53)	3.85 (0.41)	2.15 (0.47)
Eu	0.75 (0.12)	1.26 (0.56)	0.91 (0.26)	1.14 (0.17)	1.30 (0.13)	0.71 (0.12)
Gd	2.37 (0.38)	3.87 (1.72)	2.63 (0.80)	3.40 (0.69)	3.73 (0.41)	2.14 (0.42)
Tb	0.35 (0.06)	0.53 (0.23)	0.37 (0.10)	0.46 (0.08)	0.52 (0.06)	0.30 (0.04)
Dy	2.08 (0.26)	3.09 (1.19)	2.16 (0.54)	2.67 (0.47)	2.83 (0.32)	1.74 (0.22)
Ho	0.36 (0.05)	0.51 (0.19)	0.37 (0.11)	0.42 (0.07)	0.46 (0.06)	0.30 (0.04)
Er	0.90 (0.11)	1.19 (0.45)	0.88 (0.23)	0.99 (0.17)	1.07 (0.15)	0.72 (0.10)
Tm	0.10 (0.01)	0.14 (0.05)	0.10 (0.03)	0.11 (0.02)	0.12 (0.02)	0.09 (0.01)
Yb	0.62 (0.09)	0.81 (0.31)	0.60 (0.15)	0.62 (0.12)	0.67 (0.08)	0.51 (0.09)
Lu	0.08 (0.01)	0.10 (0.04)	0.07 (0.02)	0.08 (0.02)	0.08 (0.02)	0.07 (0.01)

Values in parentheses refer to 1 standard deviation from sample average.

“n=” refers to number of pyroxene grains analyzed from each sample.

See Table 1 for sample naming scheme.

Table 3: Average composition of melts calculated from pyroxene phenocrysts.

	RVV 310	RVV 318	RVV 321	RVV 343	RVV 346
Mg#	0.56 (0.02)	0.57 (0.05)	0.48 (0.03)	0.46 (0.02)	0.51 (0.06)
H₂O (wt%)	0.55 (0.13)	2.13 (0.64)	1.67 (0.31)	0.31 (0.06)	0.73 (0.16)
Temp (°C)	1216 (25)	1139 (54)	1176 (22)	1192 (11)	1154 (58)
La (ppm)	25.3 (8.8)	32.6 (3.8)	42.0 (8.3)	20.9 (3.0)	38.7 (11.8)
Ce	58.7 (20.4)	66.6 (7.5)	87.9 (14.6)	50.0 (8.8)	77.1 (20.8)
Nd	32.5 (11.8)	30.4 (3.3)	39.9 (6.6)	28.4 (4.8)	33.4 (7.7)
Sm	7.8 (2.9)	6.0 (0.8)	8.0 (1.0)	7.3 (0.9)	6.7 (1.4)
Eu	2.6 (1.0)	1.7 (0.2)	2.4 (0.3)	2.3 (0.3)	2.0 (0.4)
Gd	7.6 (3.4)	4.7 (0.4)	6.4 (0.7)	7.0 (1.0)	5.3 (1.1)
Dy	6.4 (2.9)	3.7 (0.5)	4.9 (0.5)	6.1 (0.9)	4.2 (0.8)
Ho	1.1 (0.4)	0.6 (0.1)	0.8 (0.1)	1.0 (0.2)	0.7 (0.1)
Er	2.6 (1.1)	1.6 (0.2)	2.0 (0.2)	2.7 (0.4)	1.7 (0.4)
Tm	0.3 (0.2)	0.2 (0.0)	0.2 (0.0)	0.3 (0.0)	0.2 (0.0)
Yb	2.0 (0.9)	1.3 (0.2)	1.4 (0.2)	2.0 (0.2)	1.3 (0.3)
Lu	0.3 (0.1)	0.2 (0.0)	0.2 (0.0)	0.3 (0.0)	0.2 (0.0)

Table 3 (continued): Average calculated melt composition

	RPA 367	RPA 488	RPA 502	MG1001
Mg#	0.55 (0.07)	0.56 (0.02)	0.54 (0.02)	0.60 (0.02)
H₂O (wt%)	1.08 (0.67)	1.49 (0.36)	1.06 (0.33)	1.55 (0.40)
Temp (°C)	1161 (73)	1161 (24)	1210 (16)	1270 (22)
La (ppm)	44.6 (14.5)	29.6 (4.5)	33.5 (1.5)	26.5 (7.5)
Ce	100.8 (33.1)	67.9 (8.2)	74.6 (3.9)	59.8 (17.2)
Nd	52.0 (16.6)	39.2 (4.8)	40.4 (2.4)	29.8 (8.4)
Sm	12.1 (3.9)	8.8 (1.1)	9.2 (0.6)	6.6 (1.7)
Eu	3.5 (1.1)	2.7 (0.3)	2.8 (0.2)	1.9 (0.5)
Gd	9.9 (3.1)	7.6 (1.2)	7.4 (0.5)	5.5 (1.7)
Dy	7.5 (2.6)	5.5 (0.6)	5.2 (0.4)	4.1 (1.2)
Ho	1.2 (0.4)	0.8 (0.1)	0.8 (0.1)	0.7 (0.2)
Er	2.8 (1.0)	2.0 (0.3)	1.9 (0.2)	1.7 (0.4)
Tm	0.3 (0.1)	0.2 (0.0)	0.2 (0.0)	0.2 (0.1)
Yb	2.0 (0.7)	1.3 (0.2)	1.3 (0.2)	1.2 (0.3)
Lu	0.2 (0.1)	0.2 (0.0)	0.2 (0.0)	0.2 (0.1)

Values in parentheses refer to 1 standard deviation from sample average.

“n=” refers to number of pyroxene grains analyzed from each sample.

See Table 1 for sample naming scheme.

Melt major element compositions calculated by subtracting olivine and pyroxene phenocryst in their observed abundances from whole rock compositions.

$$\text{Mg\#} = \frac{\text{Mg}}{(\text{Mg} + \text{Fe})} * 100$$

FeO* refers to total iron content ($\text{FeO}^* = \text{FeO} + \text{Fe}_2\text{O}_3$)

Melt H₂O concentrations calculated using parameters outlined in Hauri et al. [2006] (see Table A5 information).

Melt temperatures calculated from Equation 2 of Putirka et al. [2007] using olivine major element compositions calculated to be in equilibrium with pyroxene phenocrysts from the same samples.

Melt trace element compositions calculated using pyroxene/melt partition coefficients calculated from the program BigD.

Appendix

Full Methods Description

Sample Preparation:

Nine mounts of 10 samples from the Cook-Austral Islands (Raivavae, Rapa, and Mangaia) were created in the following way: Whole rock samples were crushed and sieved for mineral separates. Pristine and inclusion free clinopyroxene minerals were picked and then mounted in crystal bond on glass slides. Grains were polished with grit paper from 65 to 13 μm and then polished to 1 μm using diamond paste. The crystal bond, in which the polished grains were mounted, was dissolved in an acetone bath. Individual polished grains were then washed in a series of baths: clean acetone, ethanol, and deionized water.

Indium was used as the final mounting material for samples to minimize H_2O contamination during SIMS analysis at Arizona State University. The indium was held in 1 inch aluminum rounds with a cylindrical depression of 0.75 inches in diameter at the center. Prior to placement of the clinopyroxene grains, the indium mounts were prepared using the following procedure. Solid indium was placed in the center of the mounts and heated to 250 $^{\circ}\text{C}$ on a hot plate in order to melt the indium into the mount. To ensure no organic material was incorporated into the mount, temperatures above the melting temperature of indium were used to oxidize any organics. Indium oxidizes in the presence of oxygen, thus an oxide coat was formed on the surface of the mounts, which was scraped off prior to cooling. Lastly, the mounts were placed between two plastic sheets and pressed to 5 tons of force using a hydraulic press at the University of Texas at Austin. This ensured that the mounts had a level and flat surface. However, five tons of force was fairly excessive and resulted in the deformation of our mounts (each mount widened by a

few millimeters). The aluminum sides of these mounts had to then be ground in order to fit into the 1 inch EMPA and SIMS mount holders. Each mount was then carbon coated prior to major element analysis.

Cleaned grains were picked and loaded onto mounts and pressed into place with a clean glass microscope slide. Once grains and standards were placed, the mounts were pressed with the hydraulic press using the same procedure as before. Lastly, the mounts were lightly polished using a 1 μm diamond suspension and polishing cloth to remove surficial material. The mounts were then sonicated for 10 sec in 18M Ω water and stored in an oven at 80 °C.

Major Element Analysis:

Following sample preparation, grains within these nine mounts were analyzed for major elements using the JEOL JXA-8200 EPMA at the University of Texas at Austin. EMPA analysis were conducted using a 20 nA beam current, 15 kV accelerating voltage, and a 10 μm defocused beam. Count times were 30 to 40 seconds on peak and 15 to 20 seconds off peak. Precision of repeated analysis on the secondary standard NMNH Cr-Augite 164905 is given in Appendix Table A1. For elements with concentrations greater than 1 wt. %, reproducibility of Cr-Augite 164905 was better than 2%. For elements with concentrations less than 1 wt%, reproducibility ranged from better than 5% for Cr₂O₃, 11% for Na₂O, MnO, TiO₂, and better than 12% for MnO. Averaged analyses of NMNH Cr Augite were accurate within 5% of published values for all elements, except for Mn (within 8%) (Jarosewich et al., 1980). Cr-Augite NMNH 164905 is a true secondary standard for Mounts F, G, H, and I. However, for Mounts A through E, Al was calibrated using Cr-Augite as a primary standard, therefore NMNH Kakanui Hornblende 143965 was used as a secondary standard for this element. Repeated analyses

of Kakanui Hornblende were reproducible better than 2% for Al. Furthermore, Cr-Augite was used as the primary standard for Mg, Si, Ca and Fe for Mount A, B, and C. Thus, for these mounts, Kakanui Hornblende was used as the secondary standard for Mg, Si, Ca and Fe. Reproducibility for these elements was also better than 2%. Averaged analyses of NMNH Kakanui Hornblende were within 3% of published values for Al₂O₃, FeO, CaO, MgO, SiO₂.

Volatile Content Analysis:

Following major element analysis, samples were analyzed for H₂O contents using the Cameca IMS 6f Secondary Ion Mass Spectrometer at Arizona State University. Mounts were left in the SIMS anti-chamber at 2x10⁻⁸ torr for roughly 24 hours prior to analysis in order to minimize the background signal. Main chamber pressures ranged from 2.5 x10⁻¹⁰ to 4x10⁻¹⁰ torr during analysis and a 10 nA rastered Cs⁺ beam was used for analysis. Energy filtering was conducted with a 75V offset. Mass resolving power was approximately 5000. A 20 μm primary beam was rastered across a 40 μm square area. However, only an 8 μm circular area in the center of the rastered area was sampled. Intensities of ¹⁶O¹H, ¹⁸O, ¹⁹F, ²⁸Si, and ³⁵Cl were measured by an electron multiplier. Although a majority of the measured grains are inclusion free, intensities of ¹⁶O¹H and ³⁵Cl over the duration of individual analyses were used to monitor for possible inclusions or contamination that contain much higher H₂O content than the host pyroxene. See Appendix Figure A11a for an example of a spot analysis containing an inclusion, as well as Appendix Figure A11b for an inclusion free spot analysis.

We analyzed the exact same (or as close as possible) spots from EPMA measurements to maintain consistency across all data sets (from major elements, to H₂O content, and to trace elements). Mosenfelder and Rossman [2013 B] suggested there is

little to no matrix effects between olivine, orthopyroxene, and clinopyroxene. Therefore, we used matrix matched olivine and pyroxene standards. The well-correlated calibration curves generated from our analyses further demonstrate that there is no matrix effect between olivine, orthopyroxene, and clinopyroxene. Two to three standards were placed at the center of each mount, these standards include PMR 53, JLM 77, CITI7210, 62047708, GRR2334a, GRR16506 [Mosenfelder and Rossman, 2013 B]. In addition to standard, a blank was also placed at the center of each mount. Blanks used are San Carlos and GRR1017 [Mosenfelder and Rossman, 2013 A]. Background OH/Si intensities were determined via the analysis of either San Carlos or GRR1017. GRR1017 is a true blank standard with reported FTIR values of 0 ppm H₂O [Mosenfelder and Rossman, 2013 A]. Measurements conducted by Edward Marshall via the Thermo Electron Nicolet 6700 FTIR spectrometer at the University of Texas at Austin, show that San Carlos has <3 ppm H₂O, below detection limits for FTIR. Therefore, we cannot definitively say that San Carlos is a true blank.

A single mount was measured each day. A block of standards were run at the beginning of each analytical sequence, at the end, and between every ~10 sample analyses. Blank background intensities were subtracted from standards and samples within each calibration block. The blank corrected standard intensities were then regressed against their published values (see Appendix Table A2 for published values and references). This regression was forced through zero and the resulting regression function was used to calculate sample intensities between each standard block. Any calibration curve that produced an R² value less than 0.90 was subsequently rejected along with the sample analyses associated with said calibration curve. See Appendix Figure A12 for all calibration curves.

Several studies of the standard PMR 53 have reported a large range in H₂O concentrations from 202 ppm [Aubaud et al. 2007] to 333 [Mosenfelder and Rossman, 2013 B]. Therefore, PMR 53 was used as a secondary standard for any mounts with three or more standards, not including PMR 53. For these mounts, PMR 53 was treated in the same manner as a sample, where a regression function generated from a calibration curve was used to calculate intensity. All calculated intensities of PMR 53 were then averaged together (see Appendix Table A3) and was then used in any calibration curve that did not contain more than three standards other than PMR 53.

Individual grain H₂O contents were averaged together for each sample. Any individual grain analyses that resulted in H₂O contents outside a 2 σ standard deviation for that sample were removed from the data set and not considered in the average. Furthermore, any samples that had high standard error relative to poisson error (SE/PE > 5) were removed. This is only the case for two analyses, where SE/PE is >800 in addition to no detectable ³⁵Cl.

Trace Element Analysis:

Trace element concentrations were measured via Excimer LA-ICP-MS with a New Wave UP-193FX laser system coupled to an Agilent 7500Ce quadrupole at the University of Texas at Austin. Again, we analyzed the exact same spots (or as close as possible) from EPMA and SIMS measurements to maintain consistency across all data sets. All grains were pre-ablated with a 100 μ m spot size. Each analysis used a 90 μ m spot size at 40% power and a 10 Hz rep rate. A 45 second gas blank was collected before each analysis followed by a 60 second laser dwell time. Ablated material was transported with a He sweep gas flow rate of 750 mL/min and an Ar carrier gas flow of 900 mL/min. A total of 121 spot analyses were conducted, including standards. NIST 612 (a synthetic

glass) was used as a primary standard and BCR 2G (a USGS basalt) was used as a secondary standard. Three spots of NIST 612 and BCR 2G were analyzed at the beginning and end of the sequence, as well as between every hour of analyses. Analyses of BCR-2G were accurate within 6% of published values for all elements other than Ti (7.6%) and Pb (6.8%) (see Appendix Table A4). Repeated analyses of BCR-2G were reproducible within 5% (1σ) for all elements other than Tm (12.6%), Lu (11.3%), and U (5.5%).

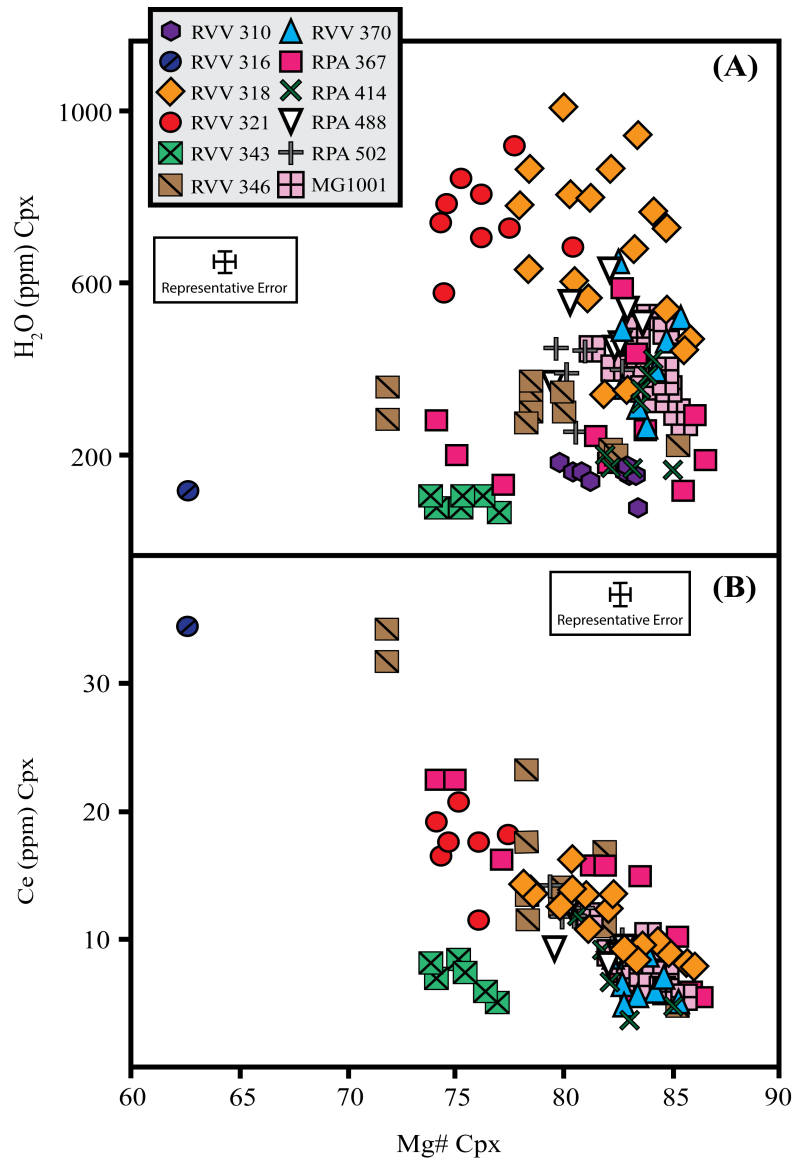


Figure A1: (A) Measured H₂O vs. Mg# of clinopyroxene phenocrysts. Overall there is no correlation between H₂O and Mg#. (B) Measured Ce vs. Mg# of clinopyroxene phenocrysts. There is a negative correlation between Ce content and Mg#.

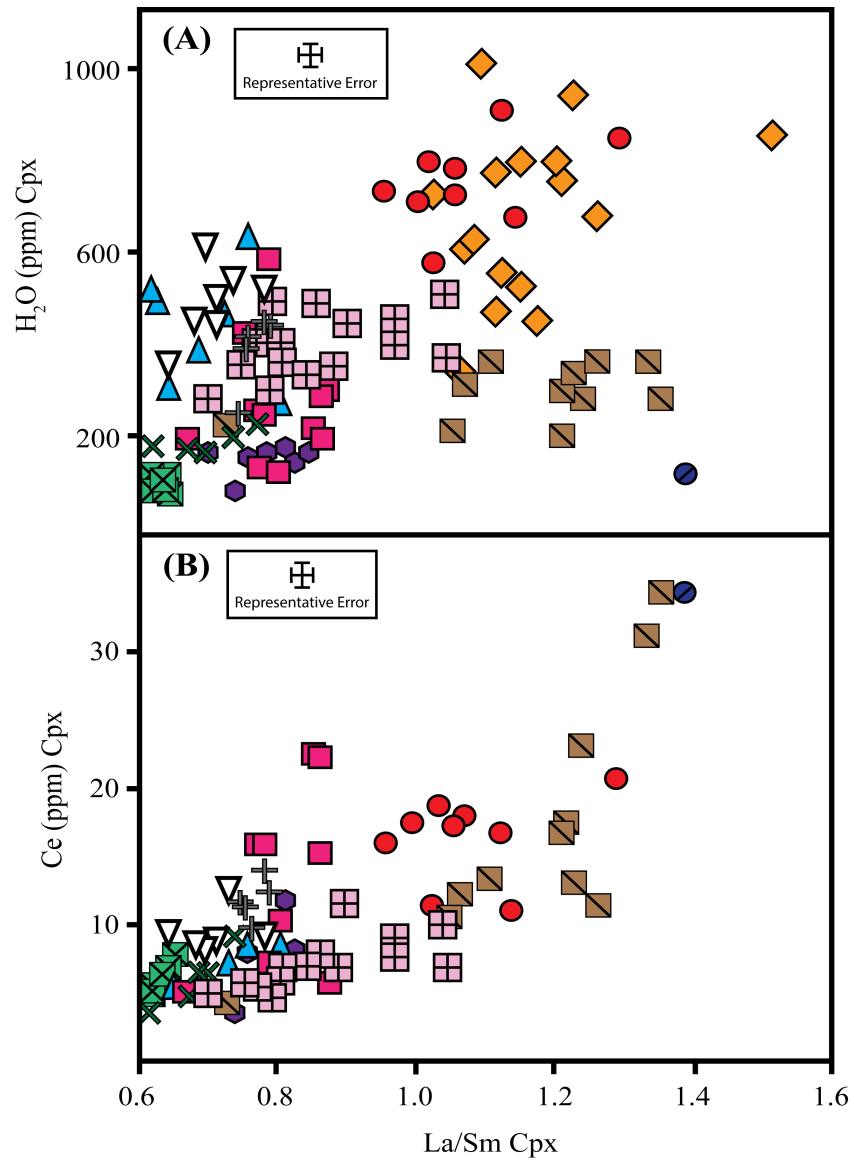


Figure A2: (A) Measured H₂O vs. La/Sm ratios of clinopyroxene phenocrysts. Overall there is a weak positive correlation between H₂O and La/Sm. (B) Measured Ce vs. La/Sm ratios of clinopyroxene phenocrysts. There is a positive correlation between Ce content and La/Sm.

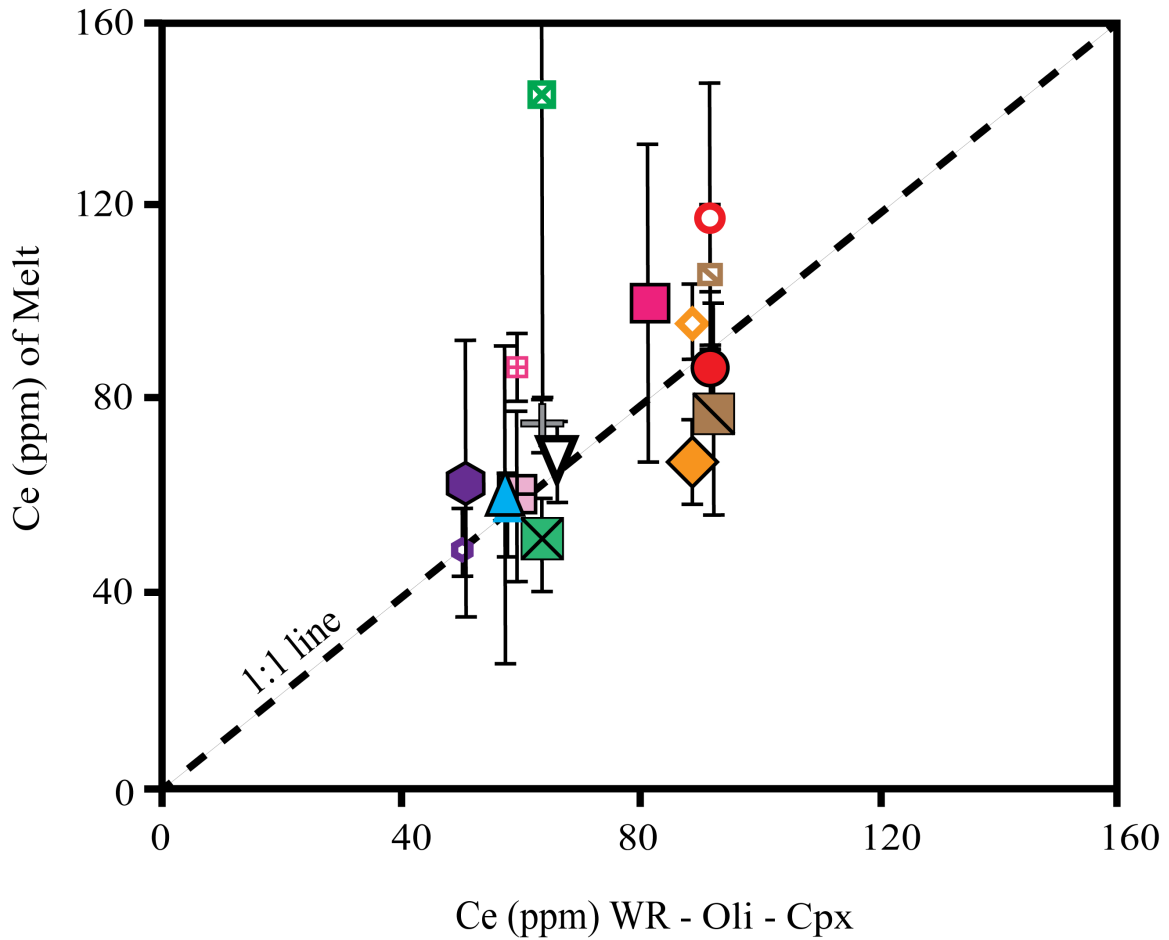


Figure A3: Average Ce concentrations of melts calculated from pyroxene and olivine-hosted melt inclusions from the same samples vs. average whole rock Ce concentrations. Melt inclusions from samples RVV 318, RVV 321, RVV 343, RVV 346 and MG1001 have systematically higher Ce concentrations than corresponding melts from pyroxene phenocrysts. Melt inclusions data from Lassiter et al. [2002], Szramek [2010], and Cabral et al. [2014].

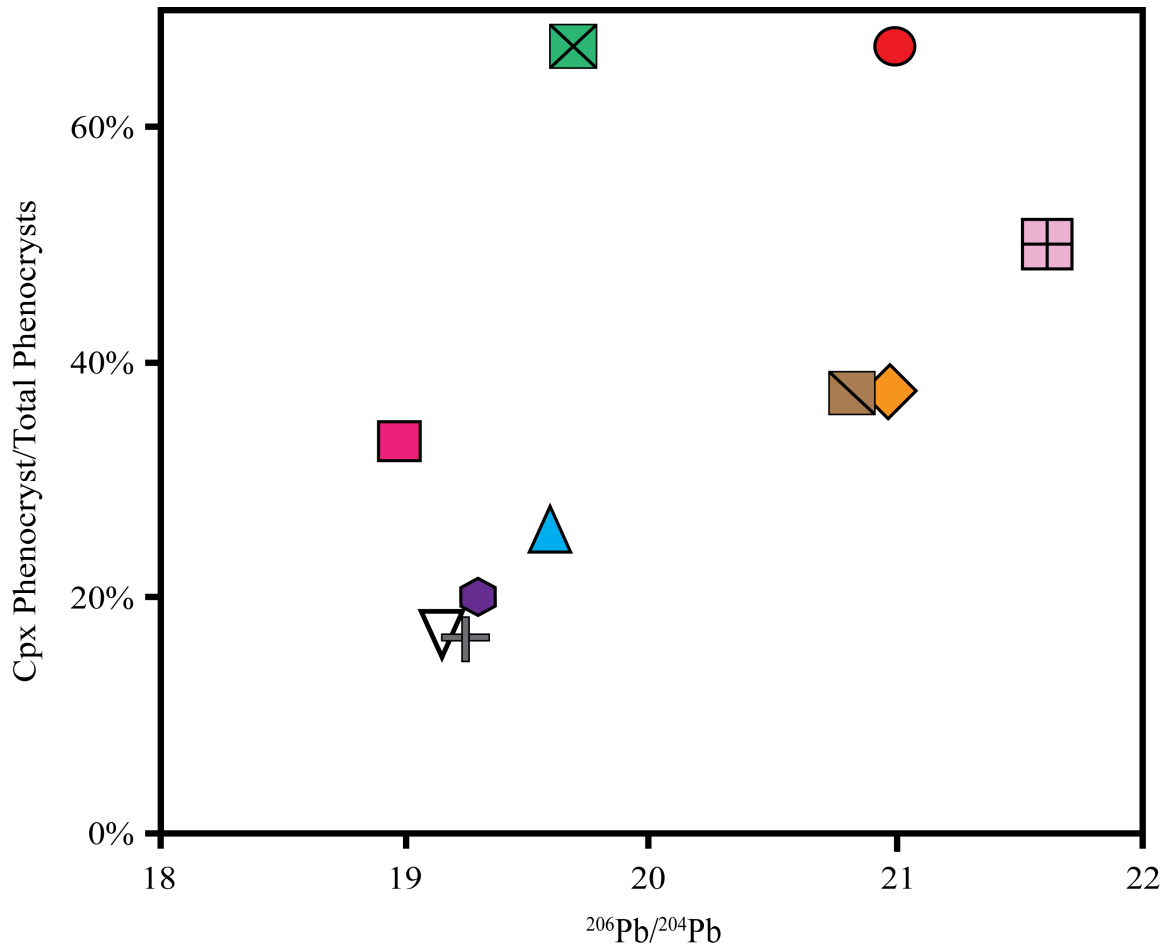


Figure A4: Cpx phenocrysts/Total phenocrysts vs. whole rock $^{206}\text{Pb}/^{204}\text{Pb}$. Cpx phenocryst represents the % phenocrysts observed in the rock and total phenocryst represents the total % of olivine and clinopyroxene phenocrysts in the rock. There is a general correlation between cpx phenocrysts/total phenocrysts and isotopic values.

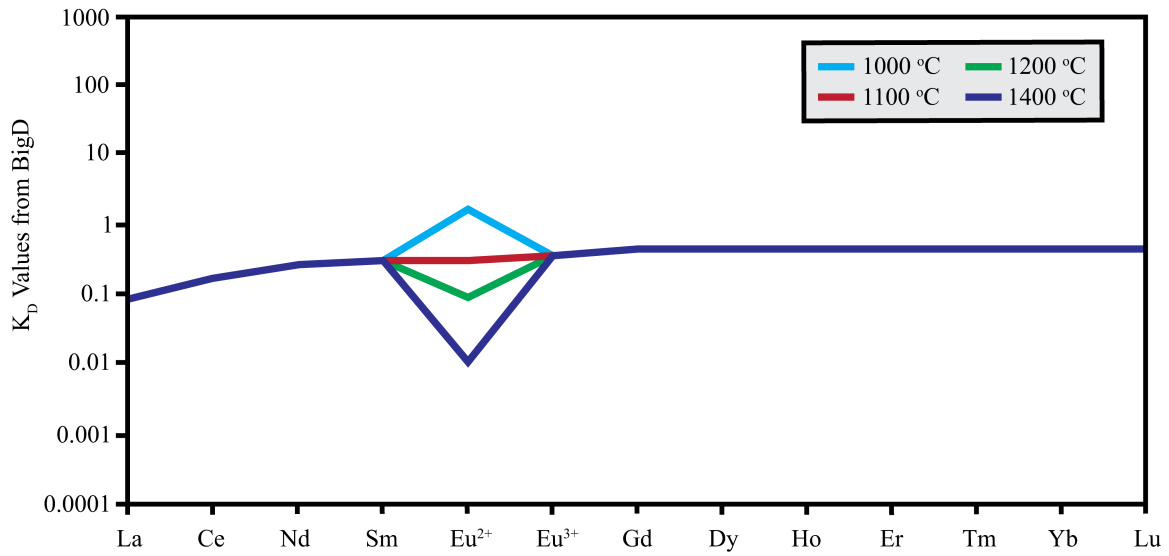


Figure A5: Calculated pyroxene/melt K_D values of a representative pyroxene grain at different temperatures. K_D values calculated from the program BigD [Nielsen, 1992]. K_D values generated from BigD are insensitive to temperature for all elements other than Eu^{2+} .

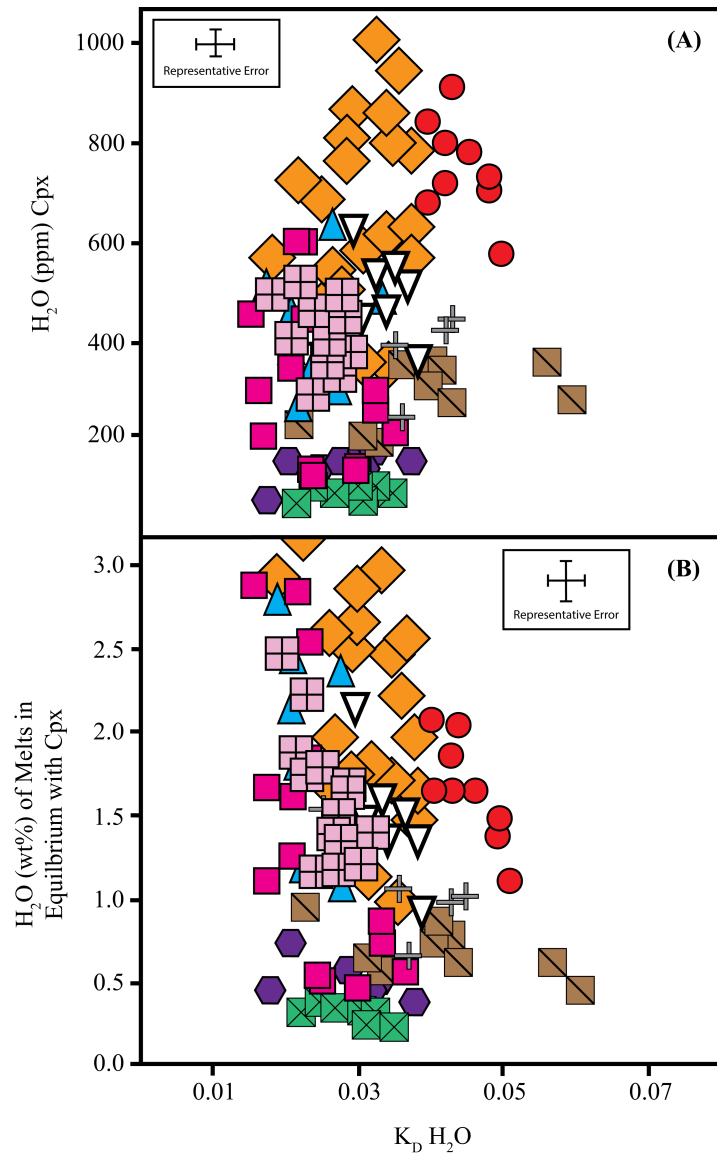


Figure A6: (A) Measured H_2O concentrations of pyroxene phenocrysts vs. calculated pyroxene/melt K_D (H_2O) values. There is no correlation between pyroxene H_2O and K_D values, which suggest K_D values are not dependent of pyroxene H_2O content. (B) H_2O content of melts calculated from pyroxene phenocrysts vs. calculated pyroxene/melt K_D (H_2O) values. There is no correlation between melt H_2O and K_D values, which suggests melt H_2O content is not dependent on K_D values. K_D values calculated from parameters outline in Hauri et al. [2006].

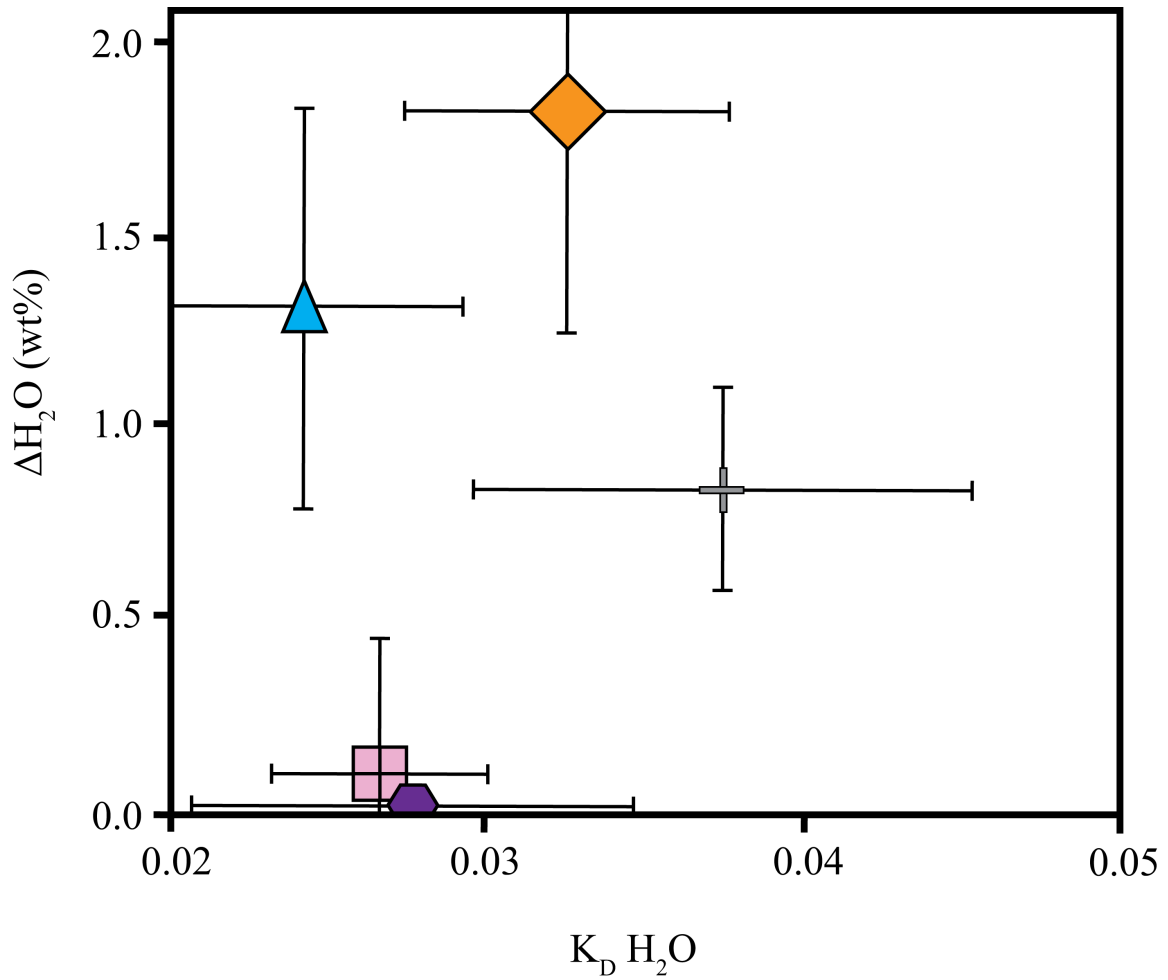


Figure A7: ΔH_2O (wt%) vs. calculated pyroxene/melt K_D (H_2O). ΔH_2O represents the difference between average magmatic H_2O calculated from pyroxene phenocrysts and average olivine-hosted melt inclusion H_2O from the same samples. Pyroxene/melt K_D values calculated from parameters outlined in Hauri et al. [2006]. There is no observed correlation between ΔH_2O and K_D values. Melt inclusions data from Lassiter et al. [2002], Szramek [2010], and Cabral et al. [2014].

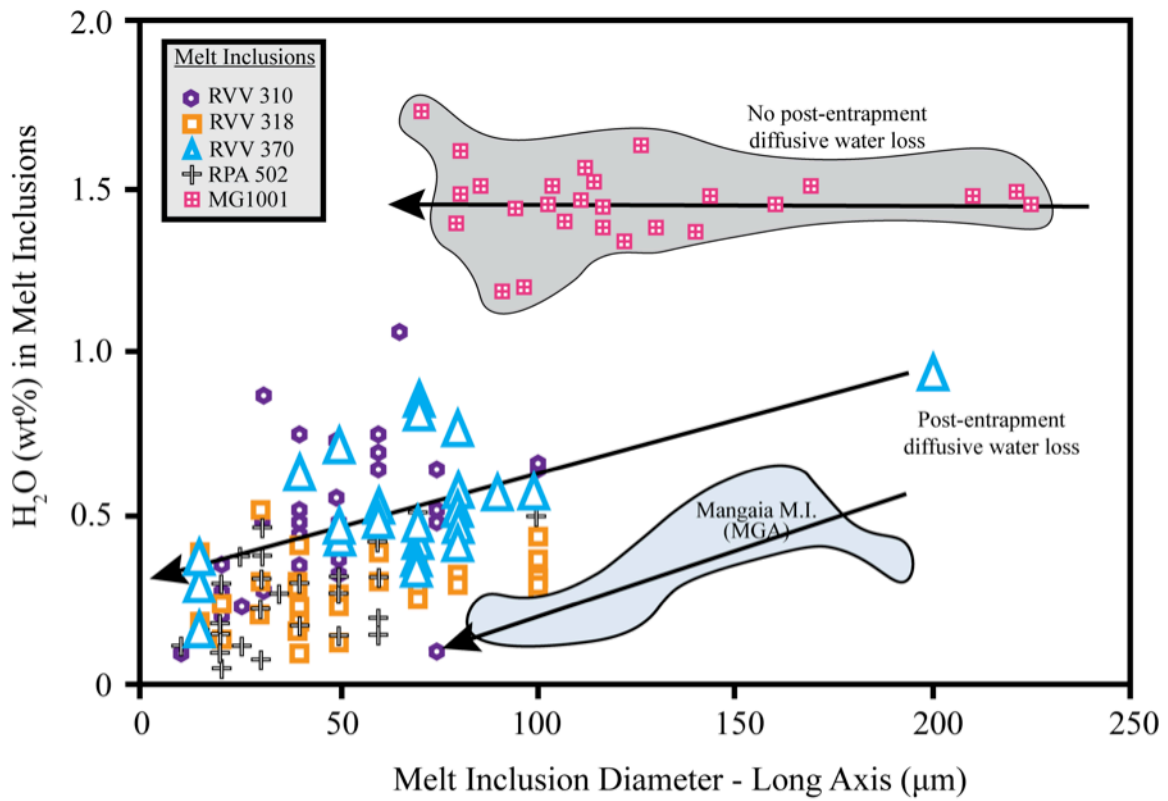


Figure A8: H₂O (wt%) in melt inclusions vs. melt inclusion diameter (long axis). Figure modified from Cabral et al. [2014]. Solid black lines represent trend lines through individual samples. Melt inclusions data from Lassiter et al. [2002], Szramek [2010], and Cabral et al. [2014].

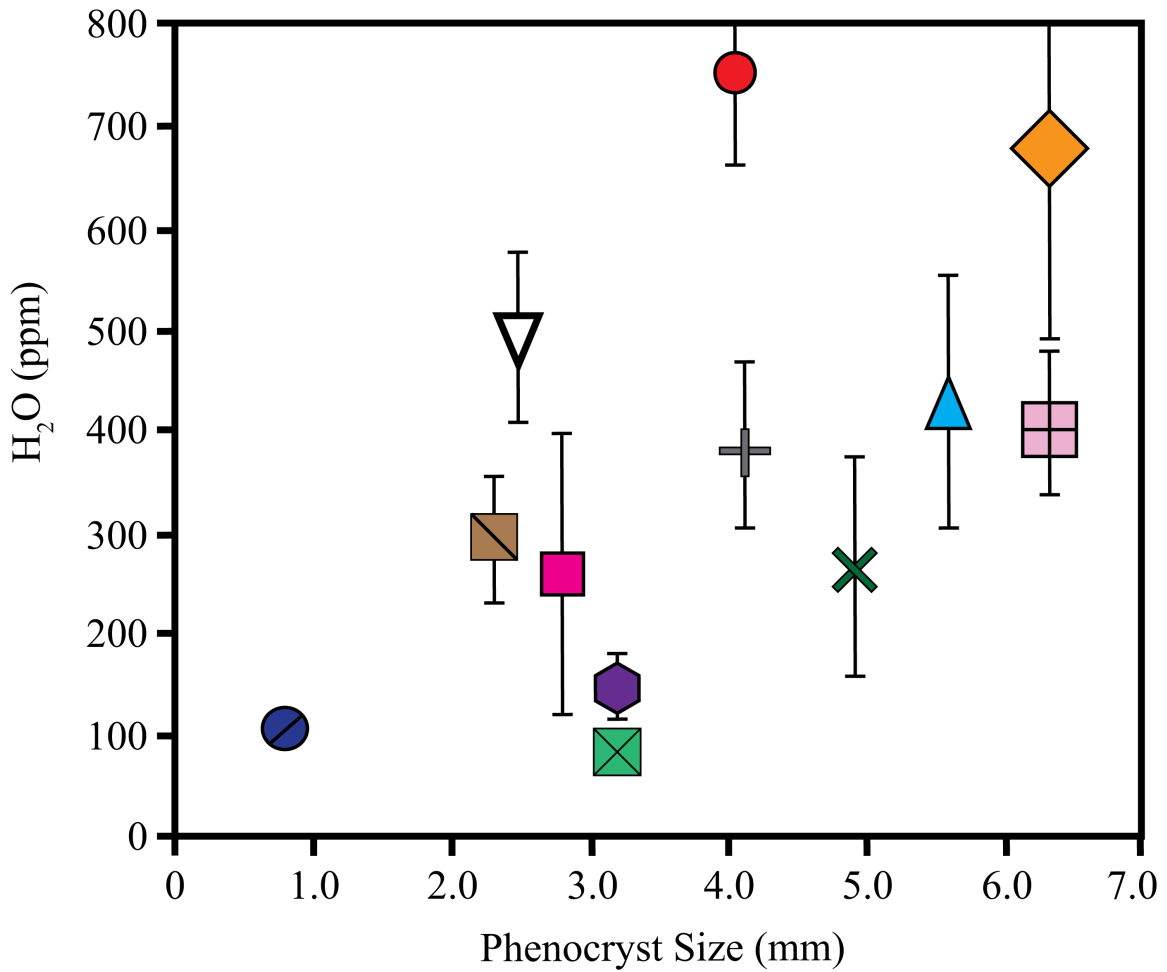


Figure A9: Average phenocryst size vs. average phenocryst H₂O content. Phenocryst size refers to the average of 10 rim-to-rim length measurements of pyroxene phenocrysts from each sample. There is a broad correlation between H₂O content and phenocrysts size.

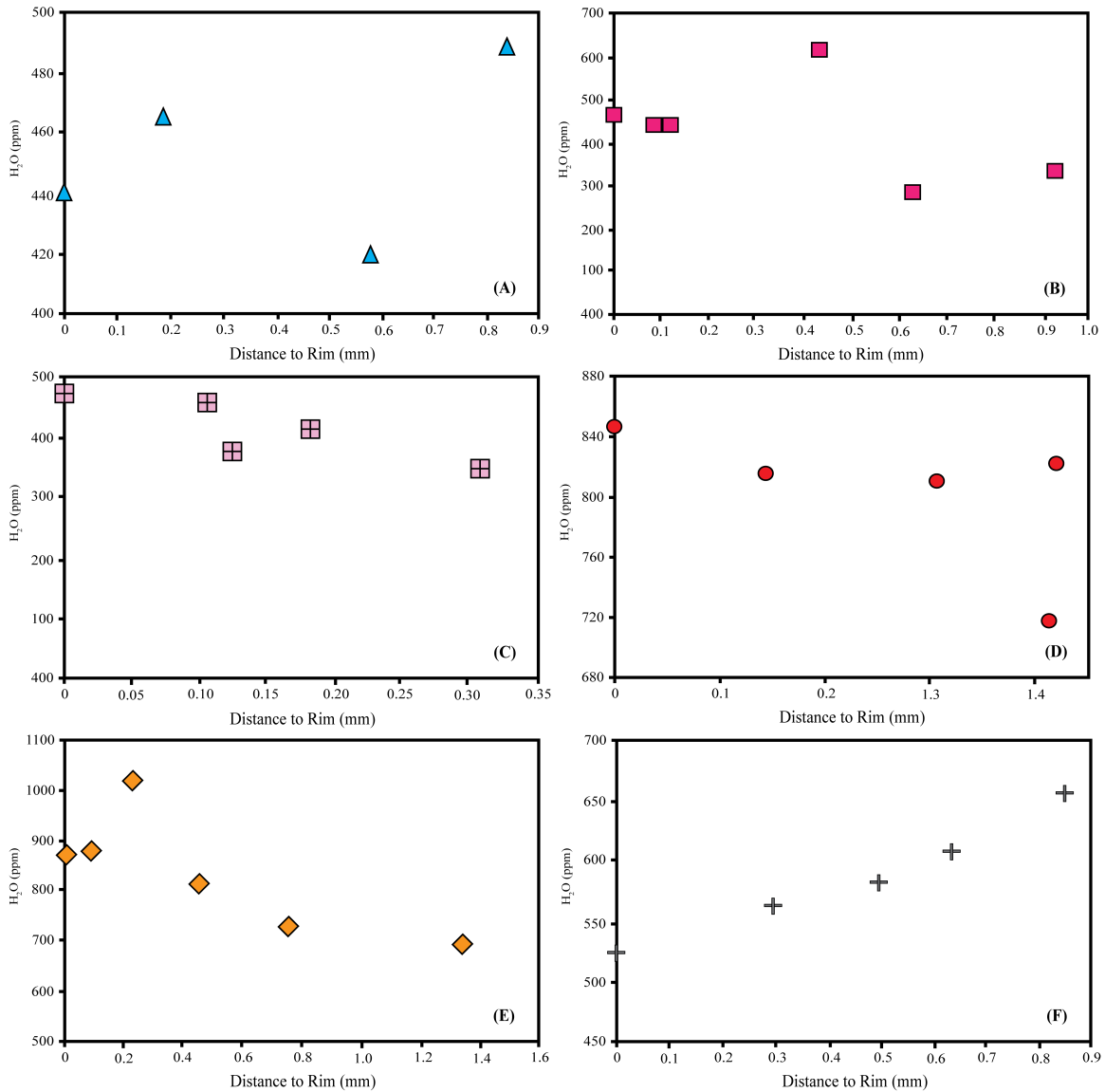


Figure A10: Core to rim transects of H₂O content in six pyroxene phenocrysts. (A) RVV 370 and (B) RPA 367 shows no clear correlations between H₂O content and distance from rim (C) MG1001 (D) RVV 321 (E) RVV 318 shows a weak correlation between H₂O content and distance from rim. However, the trend is opposite of what is expected, with an increase in H₂O towards to rim rather than a decrease. Phenocryst (C) shows a decrease in H₂O by 54 ppm (11% increase). Phenocryst (D) shows a decrease in H₂O by 25 ppm (3% increase). Phenocryst (E) shows an increase in H₂O by 184 ppm (21% increase). (F) RPA 502 shows a decrease in H₂O content from core to rim, as expected, by 131 ppm (20% decrease).

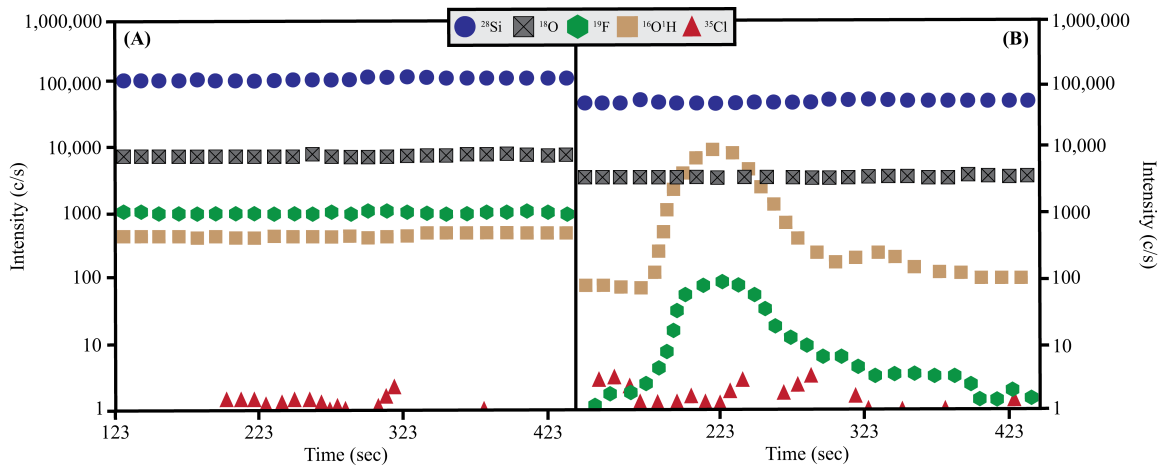


Figure A11: SIMS beam intensity (counts per second) vs. analysis time. (A) An example of a spot analysis with no inclusions. (B) An example of a spot analysis with an inclusion, which caused both the ^{19}F and $^{16}\text{O}^1\text{H}$ signal to increase.

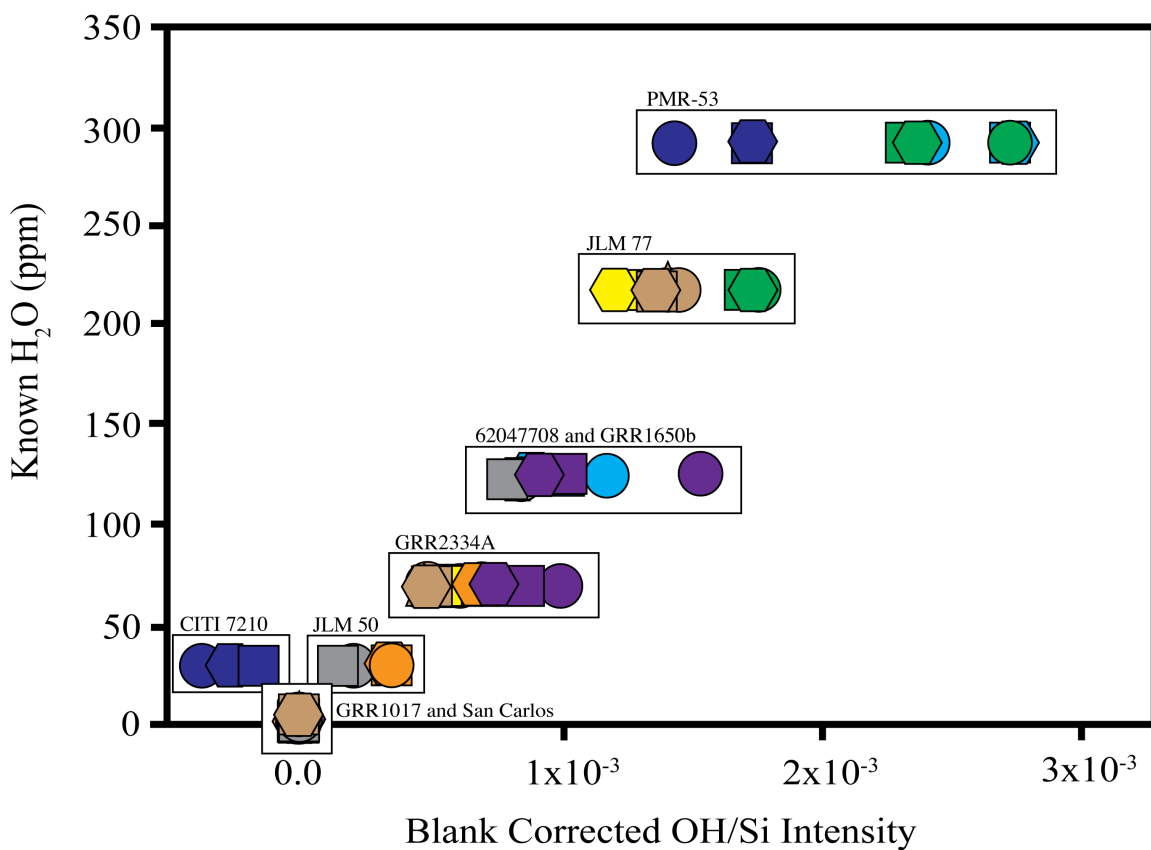


Figure A12: Known H₂O concentrations of standards vs. blank corrected OH/Si intensity for all standards used for SIMS analysis. The color of a given point represents all calibration curves generated on the same day. Symbols with the same color represent individual calibration curves within a given day. For example, the green circles represent the third calibration curve for day one and the green squares represent the second calibration curve for day one.

Table A1: Precision and accuracy of secondary standard Cr-Augite and Kakanui Hornblende.

	Cr-Augite NMNH 164905				NMNH Kakanui Hornblende 143965			
	Average	Published	%Diff	%RSD	Average	Published	%Diff	%RSD
Na ₂ O	0.82	0.84	3%	11%	-	-	-	-
Al ₂ O ₃	7.93	8.03	1%	1%	14.96	14.90	0.4%	1%
Cr ₂ O ₃	0.89	0.85	5%	4%	-	-	-	-
FeO	4.79	4.69	2%	2%	10.77	10.92	1.4%	1%
CaO	17.33	17.30	0%	1%	10.03	10.30	2.6%	1%
MgO	17.26	17.32	0%	2%	12.61	12.80	1.4%	2%
SiO ₂	49.92	50.48	1%	1%	39.92	40.37	1.1%	1%
MnO	0.13	0.12	8%	12%	-	-	-	-
K ₂ O	0.00	-	-	-	-	-	-	-
NiO	0.05	-	-	-	-	-	-	-
TiO ₂	0.49	0.51	4%	11%	-	-	-	-
Total	99.60	100.14	1%	1%	96.22	100.06	0.04	1%

Table A2: Blank corrected OH/Si intensities and known H₂O concentrations of standards used for SIMS analyses.

	Sample ID:	Blank Corrected OH/Si	Known H ₂ O (ppm)	Reference
Mount A: Standard Block 1	San Carlos-A1a	3.48E-05	3	Ed Marshall by FTIR
	JLM77-A1a	1.76E-03	217	Mosenfelder, 2013 (part 2), L&R
	PMR53-A1a	2.40E-03	291	Averaged Calculated PMR53
	GRR1017-A1a	0	0	Mosenfelder. 2011
Mount A: Standard Block 2	JLM77-A1b	1.70E-03	217	Mosenfelder, 2013 (part 2), L&R
	PMR53-A1b	2.33E-03	291	Averaged Calculated PMR53
	GRR1017-A1b	0	0	Mosenfelder. 2011
Mount A: Standard Block 3	JLM77-A1c	1.74E-03	217	Mosenfelder, 2013 (part 2), L&R
	PMR53-A1c	2.75E-03	291	Averaged Calculated PMR53
	GRR1017-A1c	0	0	Mosenfelder. 2011
Mount B: Standard Block 1	PMR53-B1a	1.67E-03	291	Averaged Calculated PMR53
	PMR53-B1b	1.44E-03	291	Averaged Calculated PMR53
	San Carlos-B1a	0	3	Ed Marshall by FTIR
	CITi7210-B1a	-4.02E-04	29	Mosenfelder, 2013 (part 2), L&R
Mount B: Standard Block 2	San Carlos-B1b	0	3	Ed Marshall by FTIR
	PMR53-B1c	1.70E-03	291	Averaged Calculated PMR53
	CITi7210-B1b	-1.94E-04	29	Mosenfelder, 2013 (part 2), L&R
Mount B: Standard Block 3	San Carlos-B1c	0	3	Ed Marshall by FTIR
	PMR53-B1d	1.70E-03	291	Averaged Calculated PMR53
	CITi7210-B1c	-2.72E-04	29	Mosenfelder, 2013 (part 2), L&R

Table A2 (continued): Blank corrected OH/Si intensities and known H₂O concentrations of standards used for SIMS analyses.

	Sample ID:	Blank Corrected OH/Si	Known H ₂ O (ppm)	Reference
Mount B: Standard Block 4	PMR53-B1e	1.82E-03	291	Averaged Calculated PMR53
	San Carlos-B1d	0	3	Ed Marshall by FTIR
	CIT17210-B1d	1.09E-03	29	Mosenfelder, 2013 (part 2), L&R
Mount C: Standard Block 1	San Carlos-C1a	0	3	Ed Marshall by FTIR
	PMR53-C1a	2.41E-03	291	Averaged Calculated PMR53
	62047708-C1a	7.76E-04	122	Mosenfelder, 2013 (part 2), L&R
Mount C: Standard Block 2	PMR53-C1b	2.76E-03	291	Averaged Calculated PMR53
	San Carlos-C1b	0	3	Ed Marshall by FTIR
	62047708-C1b	8.85E-04	122	Mosenfelder, 2013 (part 2), L&R
Mount C: Standard Block 3	PMR53-C1c	2.72E-03	291	Averaged Calculated PMR53
	San Carlos-C1c	0	3	Ed Marshall by FTIR
	62047708-C1c	1.00E-03	122	Mosenfelder, 2013 (part 2), L&R
Mount D: Standard Block 1	San Carlos-D1a	0	3	Ed Marshall by FTIR
	GRR2334a-D1a	6.39E-04	74	Mosenfelder, 2013 (part 1), L&R
	GRR1650b-D1a	7.57E-04	119	Mosenfelder, 2013 (part 1), L&R
Mount D: Standard Block 2	San Carlos-D1b	0	3	Ed Marshall by FTIR
	GRR2334a-D1b	8.33E-04	74	Mosenfelder, 2013 (part 1), L&R
	GRR16506-D1b	1.33E-03	119	Mosenfelder, 2013 (part 1), L&R
Mount D: Standard Block 3	San Carlos-D1c	0	3	Ed Marshall by FTIR
	GRR2334a-D1c	7.21E-04	74	Mosenfelder, 2013 (part 1), L&R
	GRR16506-D1c	8.54E-04	119	Mosenfelder, 2013 (part 1), L&R

Table A2 (continued): Blank corrected OH/Si intensities and known H₂O concentrations of standards used for SIMS analyses.

	Sample ID:	Blank Corrected OH/Si	Known H ₂ O (ppm)	Reference
Mount E: Standard Block 1	San Carlos-E1a	0	3	Ed Marshall by FTIR
	GRR2334a-E1a	9.51E-04	74	Mosenfelder, 2013 (part 1), L&R
	JLM50-E1a	2.20E-04	36	Mosenfelder, 2013 (part 1), L&R
Mount E: Standard Block 2	San Carlos-E1b	0	3	Ed Marshall by FTIR
	JLM50-E1b	3.15E-04	36	Mosenfelder, 2013 (part 1), L&R
	GRR2334a-E1b	5.59E-04	74	Mosenfelder, 2013 (part 1), L&R
Mount E: Standard Block 3	San Carlos-E1c	0	3	Ed Marshall by FTIR
	JLM50-E1c	3.09E-04	36	Mosenfelder, 2013 (part 1), L&R
	GRR2334a-E1c	5.80E-04	74	Mosenfelder, 2013 (part 1), L&R
Mount F: Standard Block 1	JLM77-F1a	1.44E-03	217	Mosenfelder, 2013 (part 2), L&R
	GRR2334a-F1a	4.73E-04	74	Mosenfelder, 2013 (part 1), L&R
	San Carlos-F2a	0	3	Ed Marshall by FTIR
Mount F: Standard Block 2	JLM77-F1b	1.42E-03	217	Mosenfelder, 2013 (part 2), L&R
	San Carlos-F2b	0	3	Ed Marshall by FTIR
	GRR2334a-F1b	4.71E-04	74	Mosenfelder, 2013 (part 1), L&R
Mount F: Standard Block 3	San Carlos-F2c	0	3	Ed Marshall by FTIR
	GRR2334a-F1c	5.03E-04	74	Mosenfelder, 2013 (part 1), L&R
	JLM77-F1c	1.38E-03	217	Mosenfelder, 2013 (part 2), L&R

Table A2 (continued): Blank corrected OH/Si intensities and known H₂O concentrations of standards used for SIMS analyses.

	Sample ID:	Blank Corrected OH/Si	Known H ₂ O (ppm)	Reference
Mount F: Standard Block 4	San Carlos-F2d	0	3	Ed Marshall by FTIR
	GRR2334a-F1d	5.42E-04	74	Mosenfelder, 2013 (part 1), L&R
	JLM77-F1d	1.35E-03	217	Mosenfelder, 2013 (part 2), L&R
Mount G: Standard Block 1	San Carlos-G1a	0	3	Ed Marshall by FTIR
	JLM77-G1a	1.43E-03	217	Mosenfelder, 2013 (part 2), L&R
	GRR2334a-G1a	4.73E-04	74	Mosenfelder, 2013 (part 1), L&R
Mount G: Standard Block 2	San Carlos-G1b	0	3	Ed Marshall by FTIR
	JLM77-G1b	1.34E-03	217	Mosenfelder, 2013 (part 2), L&R
	GRR2334a-G1b	4.78E-04	74	Mosenfelder, 2013 (part 1), L&R
Mount G: Standard Block 3	San Carlos-G1c	0	3	Ed Marshall by FTIR
	JLM77-G1c	1.23E-03	217	Mosenfelder, 2013 (part 2), L&R
	GRR2334a-G1c	4.70E-04	74	Mosenfelder, 2013 (part 1), L&R
Mount H: Standard Block 1	San Carlos-H1a	0	3	Ed Marshall by FTIR
	GRR1650b-H1a	4.22E-04	119	Mosenfelder, 2013 (part 1), L&R
	62047-70B-H1a	6.35E-04	122	Mosenfelder, 2013 (part 2), L&R
	CITI7210-H1a	2.35E-04	29	Mosenfelder, 2013 (part 2), L&R
	GRR1650b-H1b	3.57E-04	119	Mosenfelder, 2013 (part 1), L&R
Mount H: Standard Block 2	San Carlos-H1b	0	3	Ed Marshall by FTIR
	GRR1650b-H1b	6.00E-04	119	Mosenfelder, 2013 (part 1), L&R
	62047-70B-H1b	7.82E-04	122	Mosenfelder, 2013 (part 2), L&R
	CITI7210-H1b	2.46E-04	29	Mosenfelder, 2013 (part 2), L&R

Table A2 (continued): Blank corrected OH/Si intensities and known H₂O concentrations of standards used for SIMS analyses.

	Sample ID:	Blank Corrected OH/Si	Known H ₂ O (ppm)	Reference
Mount H: Standard Block 3	GRR1650b-H1c	6.00E-04	119	Mosenfelder, 2013 (part 1), L&R
	San Carlos-H1c	0	3	Ed Marshall by FTIR
	62047-70B-H1c	7.40E-04	122	Mosenfelder, 2013 (part 2), L&R
	CITI7210-H1c	2.05E-04	29	Mosenfelder, 2013 (part 2), L&R
Mount I: Standard Block 1	GRR1017-I1a	0	0	Mosenfelder. 2011
	San Carlos-I1a	2.50E-06	3	Ed Marshall by FTIR
	GRR2334a-I1a	5.87E-04	74	Mosenfelder, 2013 (part 1), L&R
	CITI7210-I1a	2.30E-04	29	Mosenfelder, 2013 (part 2), L&R
Mount I: Standard Block 2	GRR1017-I1b	0	0	Mosenfelder. 2011
	San Carlos-I1b	1.47E-05	3	Ed Marshall by FTIR
	GRR2334a-I1b	5.84E-04	74	Mosenfelder, 2013 (part 1), L&R
	CITI7210-I1b	2.58E-04	29	Mosenfelder, 2013 (part 2), L&R
Mount I: Standard Block 3	GRR1017-I1c	0	0	Mosenfelder. 2011
	GRR2334a-I1c	5.71E-04	74	Mosenfelder, 2013 (part 1), L&R
	CITI7210-I1c	2.63E-04	29	Mosenfelder, 2013 (part 2), L&R
	San Carlos-I1c	1.53E-05	3	Ed Marshall by FTIR

Table A3: Individual and averaged calculated intensities of secondary standard PMR 53.

Sample ID:	Calculated H ₂ O (ppm)
PMR53-D1a	339.4
PMR53-D1b	234.1
PMR53-D1c	271.3
PMR53-E1a	-
PMR53-E1b	244.7
PMR53-E1c	236.1
PMR53-E1d	249.2
PMR53-F3a	323.5
PMR53-F3b	335.9
PMR53-F3c	298.7
PMR53-F3d	315.5
PMR-53-G3a	314.4
PMR-53-G3b	313.7
PMR53-G3c	-
PMR53-H1a	-
PMR53-H1b	336.1
PMR53-H1c	338.4
PMR53-I1b	278.6
PMR53-I1a	304.9
PMR53-I1c	257.5
PMR53-I1d	253.3
AVERAGE	291
±σ	38.2

Table A4: Average measured trace element composition of LA-ICP-MS secondary standard BCR-2G compared to published values.

BCR-2G	Average	$\pm\sigma$	Published	Accuracy to Standard	%RSD
Na	23803	232	23962	0.7%	1.0%
Ca	50124	742	50457	0.7%	1.5%
Ti	13032	387	14100	7.6%	3.0%
V	436	5.21	425	2.6%	1.2%
Rb	47.3	0.67	47.0	0.6%	1.4%
Sr	326	7.58	342	4.8%	2.3%
Y	33.2	1.13	35.0	5.2%	3.4%
Zr	180	4.89	184	2.2%	2.7%
Nb	12.9	0.25	12.5	3.5%	1.9%
Ba	665	13.83	683	2.7%	2.1%
La	24.4	0.70	24.7	1.2%	2.9%
Ce	51.2	1.12	53.3	3.9%	2.2%
Pr	6.37	0.19	6.70	4.9%	3.0%
Nd	28.1	0.86	28.9	2.7%	3.1%
Sm	6.62	0.21	6.59	0.4%	3.2%
Eu	1.95	0.08	1.97	1.0%	4.0%
Gd	6.45	0.25	6.71	3.8%	3.8%
Tb	1.00	0.05	1.02	2.3%	5.0%
Dy	6.35	0.23	6.44	1.4%	3.7%
Ho	1.27	0.05	1.27	0.2%	4.0%
Er	3.58	0.11	3.70	3.3%	3.2%
Tm	0.54	0.07	0.51	5.5%	12.6%
Yb	3.41	0.11	3.39	0.5%	3.3%
Lu	0.51	0.06	0.50	1.2%	11.3%
Hf	4.58	0.17	4.84	5.3%	3.8%
Pb	10.3	0.30	11.0	6.8%	2.9%
Th	5.99	0.19	5.90	1.5%	3.2%
U	1.75	0.10	1.69	3.4%	5.5%

Table A5: Individual clinopyroxene major, trace, and volatile compositions

	RVV 310- A1a	RVV 310- A1b	RVV 310- B1a	RVV 310- C1a	RVV 310- D1a
SiO₂ (wt%)	48.54	47.92	51.14	50.17	50.50
TiO₂	0.98	1.14	0.28	0.61	0.62
Al₂O₃	4.78	6.38	4.22	4.30	4.30
Cr₂O₃	0.91	0.87	1.27	1.05	1.01
FeO	5.86	6.11	5.66	6.08	5.93
MnO	0.17	0.12	0.10	0.14	0.14
MgO	15.91	14.12	16.01	16.67	15.91
CaO	20.27	21.64	20.59	20.76	20.70
Na₂O	0.33	0.27	0.36	0.36	0.33
K₂O			0.01		
NiO				0.00	0.02
Total	97.76	98.55	99.65	100.15	99.47
Mg#	0.83	0.80	0.83	0.83	0.83
Cr#	0.11	0.08	0.17	0.14	0.14
H₂O (ppm)	157.81	162.41	77.12	148.36	157.97
Sr	39	40.3	28.27	29.94	53.3
Y	8.34	7.8	6.14	7	9.8
Zr	18.95	18.95	8.91	10.52	26.01
Nb	0.12	0.14	0.07	0.06	0.20
Ba			0.00		0.18
La	1.26	1.29	0.57	0.74	1.80
Ce	5.10	5.40	2.50	3.31	7.45
Pr	0.93	0.91	0.44	0.56	1.30
Nd	5.53	5.57	3.06	3.36	7.52
Sm	1.79	1.65	1.13	1.31	2.14
Eu	0.66	0.61	0.42	0.48	0.84
Gd	2.13	1.94	1.47	1.64	2.69
Tb	0.35	0.30	0.22	0.24	0.39
Dy	1.94	1.82	1.46	1.57	2.37
Ho	0.35	0.35	0.23	0.29	0.41
Er	0.90	0.78	0.59	0.72	0.97
Tm	0.11	0.10	0.08	0.08	0.11
Yb	0.60	0.60	0.49	0.48	0.72
Lu	0.08	0.07	0.06	0.07	0.10
Hf	0.92	0.79	0.43	0.46	1.20
Pb					0.03
Th	0.02	0.02	0.01		0.02
U					

Table A5 (continued): Individual clinopyroxene major, trace, and volatile compositions

	RVV 310-G1a	RVV 310-H1a	RVV 310-I1a	RVV 316-B1a
SiO₂ (wt%)	51.78	49.01	49.50	46.17
TiO₂	0.70	1.60	1.36	2.13
Al₂O₃	4.50	6.31	6.07	8.20
Cr₂O₃	1.02	0.50	0.82	0.01
FeO	5.80	6.42	6.05	10.56
MnO	0.12	0.11	0.09	0.29
MgO	16.00	14.22	14.70	9.90
CaO	21.61	22.62	22.43	22.44
Na₂O	0.41	0.44	0.40	0.66
K₂O				
NiO	0.04	0.04	0.06	
Total	101.98	101.25	101.49	100.36
Mg#	0.83	0.80	0.81	0.63
Cr#	0.13	0.05	0.08	0.00
H₂O (ppm)	154.39	178.89	137.02	111.26
Sr	36.73	63.31	59.51	135.1
Y	7.74	12.53	9.32	15.78
Zr	14.1	53.5	33.16	144.4
Nb	0.09	0.35	0.24	2.49
Ba				1.74
La	0.88	2.94	2.08	9.24
Ce	3.84	12.06	8.51	34.50
Pr	0.70	2.05	1.43	5.42
Nd	4.29	12.09	8.49	26.80
Sm	1.47	3.63	2.52	6.67
Eu	0.57	1.21	0.89	1.99
Gd	1.76	3.68	2.50	5.44
Tb	0.28	0.56	0.38	0.75
Dy	1.78	3.18	2.27	4.19
Ho	0.32	0.55	0.40	0.69
Er	0.72	1.32	0.92	1.54
Tm	0.09	0.15	0.10	0.18
Yb	0.59	0.86	0.66	1.09
Lu	0.08	0.11	0.09	0.15
Hf	0.65	2.38	1.45	5.68
Pb				0.11
Th	0.01	0.03	0.03	0.15
U				0.03

Table A5 (continued): Individual clinopyroxene major, trace, and volatile compositions

	RVV 318-C1c	RVV 318-C1d	RVV 318-C1g	RVV 318-C1h
SiO₂ (wt%)	49.73	49.30	50.02	49.62
TiO₂	0.88	1.05	0.81	0.86
Al₂O₃	4.55	5.20	4.23	4.27
Cr₂O₃	0.97	0.67	0.74	0.73
FeO	4.95	5.10	4.63	4.73
MnO	0.08	0.08	0.11	0.09
MgO	15.49	15.11	15.70	15.73
CaO	23.15	23.18	23.43	23.23
Na₂O	0.31	0.38	0.42	0.32
K₂O				
NiO	0.01	0.07	0.04	0.02
Total	100.13	100.12	100.12	99.61
Mg#	0.85	0.84	0.86	0.86
Cr#	0.13	0.08	0.11	0.10
H₂O (ppm)	542.03	767.31	474.32	454.37
Sr	48.7	50.8	46.4	47.6
Y	6.68	7.72	5.81	6.07
Zr	23.61	28.4	20.36	21.26
Nb	0.21	0.43	0.16	0.18
Ba	0.05	0.06	0.05	0.00
La	2.30	2.67	2.04	2.17
Ce	9.16	9.88	8.09	8.31
Pr	1.49	1.65	1.32	1.31
Nd	7.74	8.69	7.13	7.37
Sm	1.99	2.21	1.83	1.85
Eu	0.60	0.68	0.58	0.59
Gd	2.04	2.23	1.73	1.74
Tb	0.27	0.32	0.25	0.25
Dy	1.60	1.74	1.45	1.40
Ho	0.28	0.33	0.25	0.25
Er	0.67	0.83	0.57	0.69
Tm	0.09	0.09	0.08	0.09
Yb	0.56	0.64	0.43	0.45
Lu	0.06	0.08	0.06	0.06
Hf	1.12	1.41	1.02	1.03
Pb	0.02	0.03	0.02	0.01
Th	0.02	0.03	0.01	0.01
U				0.00

Table A5 (continued): Individual clinopyroxene major, trace, and volatile compositions

	RVV 318-D1a	RVV 318-E1a	RVV 318-F1a	RVV 318-G1a
SiO₂ (wt%)	47.93	49.38	47.60	48.59
TiO₂	1.61	1.27	1.74	1.66
Al₂O₃	6.93	5.31	7.10	6.93
Cr₂O₃	0.28	0.93	0.14	0.26
FeO	5.99	5.79	6.70	6.06
MnO	0.12	0.11	0.10	0.11
MgO	14.38	15.54	13.33	13.94
CaO	22.72	21.86	23.52	23.06
Na₂O	0.43	0.54	0.37	0.45
K₂O				
NiO	0.05	0.06	0.01	0.02
Total	100.44	100.78	100.59	101.08
Mg#	0.81	0.83	0.78	0.80
Cr#	0.03	0.10	0.01	0.02
H₂O (ppm)	570.34	358.20	787.89	614.15
Sr	61.5	51.8	55.3	61.25
Y	11.72	9.87	11.41	12.81
Zr	47.1	29.75	53.44	51.72
Nb	0.49	0.22	0.60	0.51
Ba			0.00	
La	3.76	2.30	3.76	3.79
Ce	13.57	9.04	14.38	14.05
Pr	2.32	1.50	2.23	2.34
Nd	12.17	9.38	12.97	12.51
Sm	3.35	2.87	3.37	3.57
Eu	1.11	1.00	1.09	1.15
Gd	3.22	2.77	3.29	3.33
Tb	0.45	0.42	0.47	0.48
Dy	2.81	2.54	2.75	3.00
Ho	0.47	0.41	0.49	0.53
Er	1.19	0.96	1.09	1.38
Tm	0.15	0.12	0.15	0.17
Yb	0.98	0.69	0.90	1.05
Lu	0.12	0.08	0.13	0.12
Hf	2.21	1.35	2.55	2.36
Pb	0.02			
Th	0.05	0.02	0.06	0.05
U				

Table A5 (continued): Individual clinopyroxene major, trace, and volatile compositions

	RVV 318-H2a	RVV 318-H2b	RVV 318-H2c	RVV 318-H2d
SiO₂ (wt%)	46.81	49.20	48.54	49.22
TiO₂	1.58	1.21	1.41	1.26
Al₂O₃	6.28	5.72	6.33	5.83
Cr₂O₃	0.30	0.35	0.29	0.29
FeO	6.42	5.63	6.24	5.84
MnO	0.13	0.11	0.12	0.09
MgO	13.02	14.57	13.95	14.18
CaO	22.71	23.22	23.31	23.33
Na₂O	0.37	0.35	0.35	0.34
K₂O				
NiO	0.01	0.05	0.05	0.04
Total	97.63	100.41	100.60	100.44
Mg#	0.78	0.82	0.80	0.81
Cr#	0.03	0.04	0.03	0.03
H₂O (ppm)	873.60	876.04	1019.37	808.38
Sr	60.8		53.64	51.99
Y	9.69		10.65	8.89
Zr	42.1		48	36.62
Nb	1.54		0.47	0.39
Ba	3.05		0.05	0.07
La	4.11		3.39	2.92
Ce	13.73		12.85	10.74
Pr	2.04		2.13	1.78
Nd	10.71		11.73	9.62
Sm	2.72		3.10	2.54
Eu	0.88		1.02	0.89
Gd	2.70		2.72	2.50
Tb	0.37		0.41	0.35
Dy	2.23		2.72	2.18
Ho	0.42		0.45	0.38
Er	0.97		1.15	0.92
Tm	0.12		0.13	0.12
Yb	0.80		0.96	0.74
Lu	0.10		0.12	0.09
Hf	1.87		2.27	1.90
Pb				
Th	0.15		0.04	0.03
U				

Table A5 (continued): Individual clinopyroxene major, trace, and volatile compositions.

	RVV 318-H2f	RVV 318-I1a	RVV 321-A1a	RVV 321-A1b
SiO₂ (wt%)	50.18	47.75	46.46	46.15
TiO₂	1.12	1.73	1.67	1.62
Al₂O₃	5.23	7.36	8.62	9.04
Cr₂O₃	0.42	0.14	0.11	0.18
FeO	5.39	6.64	6.70	6.88
MnO	0.10	0.10	0.14	0.09
MgO	14.92	13.40	13.11	12.33
CaO	23.14	23.40	21.87	21.94
Na₂O	0.34	0.34	0.83	0.58
K₂O			0.01	0.01
NiO	0.00	0.03		
Total	100.83	100.89	99.52	98.82
Mg#	0.83	0.78	0.78	0.76
Cr#	0.05	0.01	0.01	0.01
H₂O (ppm)	689.63	638.69	918.87	809.93
Sr	47.84	55.84	74.9	58
Y	6.92	11.26	12.25	9.63
Zr	20.95	54.1	51.6	37.8
Nb	0.21	0.57	0.75	0.45
Ba	0.04	0.04		
La	2.35	3.68	4.43	3.00
Ce	8.24	14.08	16.96	11.55
Pr	1.35	2.32	2.61	1.85
Nd	6.97	11.76	13.98	10.12
Sm	1.86	3.40	3.94	2.94
Eu	0.61	1.08	1.25	0.92
Gd	1.98	3.33	3.65	2.80
Tb	0.26	0.43	0.51	0.40
Dy	1.60	2.58	3.03	2.38
Ho	0.28	0.46	0.54	0.40
Er	0.68	1.16	1.36	1.02
Tm	0.10	0.14	0.15	0.12
Yb	0.55	0.86	0.87	0.70
Lu	0.07	0.11	0.12	0.09
Hf	0.99	2.48	2.40	1.82
Pb			0.02	0.02
Th	0.02	0.05	0.08	0.04
U		0.01	0.01	0.01

Table A5 (continued): Individual clinopyroxene major, trace, and volatile compositions.

	RVV 321-C1a	RVV 321-D1a	RVV 321-E1a	RVV 321-F1a
SiO₂ (wt%)	45.87	47.35	45.55	46.01
TiO₂	2.19	1.45	2.29	2.39
Al₂O₃	9.11	7.59	9.35	9.72
Cr₂O₃	0.22	0.54	0.02	0.04
FeO	7.21	6.07	7.71	7.56
MnO	0.10	0.10	0.15	0.10
MgO	12.90	14.03	12.49	12.29
CaO	22.06	22.12	22.28	22.21
Na₂O	0.84	0.63	0.77	0.73
K₂O				
NiO	0.02	0.04		0.00
Total	100.52	99.92	100.61	101.06
Mg#	0.76	0.80	0.74	0.74
Cr#	0.02	0.05	0.00	0.00
H₂O (ppm)	713.44	682.57	577.32	744.00
Sr	83.1	64.3	82.4	78.6
Y	14.22	9.7	14.24	14.14
Zr	57.5	30.1	65.7	53.7
Nb	0.76	0.51	0.91	0.77
Ba	0.06	0.75		0.02
La	4.55	2.97	4.95	4.00
Ce	17.80	11.33	19.01	16.27
Pr	2.87	1.79	3.11	2.64
Nd	15.82	9.57	17.22	14.90
Sm	4.56	2.61	4.81	4.19
Eu	1.52	0.90	1.55	1.36
Gd	4.24	2.56	4.44	4.20
Tb	0.59	0.39	0.59	0.58
Dy	3.40	2.31	3.59	3.44
Ho	0.58	0.40	0.65	0.57
Er	1.46	0.98	1.56	1.38
Tm	0.17	0.12	0.17	0.17
Yb	1.04	0.63	0.99	0.96
Lu	0.13	0.09	0.14	0.13
Hf	2.64	1.49	3.08	2.57
Pb	0.05	0.03		
Th	0.05	0.05	0.08	0.06
U	0.01			

Table A5 (continued): Individual clinopyroxene major, trace, and volatile compositions.

	RVV 321-H1a	RVV 343-A1a	RVV 343-C1a	RVV 343-F1a
SiO₂ (wt%)	47.21	48.64	47.46	50.18
TiO₂	1.84	1.00	1.46	1.03
Al₂O₃	7.83	4.94	5.53	3.96
Cr₂O₃	0.16	0.24	0.16	0.19
FeO	7.48	8.51	8.56	7.97
MnO	0.13	0.20	0.19	0.15
MgO	12.75	14.57	14.48	14.89
CaO	22.20	21.05	20.64	21.10
Na₂O	0.73	0.48	0.40	0.43
K₂O				
NiO	0.01		0.02	0.01
Total	100.34	99.63	98.90	99.90
Mg#	0.75	0.75	0.75	0.77
Cr#	0.01	0.03	0.02	0.03
H₂O (ppm)	849.44	105.46	84.45	72.43
Sr	90.8	35.7	35	33.69
Y	14.33	11.47	15.49	10.25
Zr	70.5	24.5	35.1	19.34
Nb	0.89	0.11	0.20	0.10
Ba	0.03			
La	5.78	1.59	1.83	1.33
Ce	20.79	7.25	8.20	5.42
Pr	3.47	1.22	1.40	1.02
Nd	18.44	7.67	8.96	6.13
Sm	4.48	2.48	3.29	2.18
Eu	1.52	0.89	1.11	0.79
Gd	4.23	2.86	3.71	2.56
Tb	0.61	0.43	0.57	0.38
Dy	3.56	2.71	3.43	2.48
Ho	0.60	0.49	0.65	0.43
Er	1.47	1.26	1.57	1.05
Tm	0.18	0.14	0.18	0.11
Yb	1.11	0.82	1.08	0.85
Lu	0.12	0.11	0.14	0.10
Hf	3.08	1.18	1.61	0.95
Pb			0.01	
Th	0.06	0.01	0.02	0.01
U				

Table A5 (continued): Individual clinopyroxene major, trace, and volatile compositions.

	RVV 343-I1a	RVV 343-I1b	RVV 346-A1a	RVV 346-A1b
SiO₂ (wt%)	49.02	48.77	43.39	43.09
TiO₂	1.56	1.61	2.73	3.48
Al₂O₃	5.63	5.79	10.14	10.54
Cr₂O₃	0.22	0.22	0.02	0.03
FeO	8.79	8.93	8.00	7.96
MnO	0.18	0.17	0.13	0.14
MgO	14.07	14.12	11.42	11.35
CaO	21.02	20.80	22.53	22.38
Na₂O	0.47	0.49	0.44	0.46
K₂O			0.00	0.02
NiO	0.01	0.03		
Total	100.96	100.94	98.79	99.44
Mg#	0.74	0.74	0.72	0.72
Cr#	0.03	0.03	0.00	0.00
H₂O (ppm)	78.53	98.80	363.45	278.87
Sr	38.5	36.06	77.5	79.1
Y	13.13	14.7	22.46	23.58
Zr	27.11	35.73	145.3	172.5
Nb	0.18	0.23	1.81	2.48
Ba			0.06	0.78
La	1.68	1.92	9.03	9.64
Ce	7.30	8.01	31.54	34.41
Pr	1.26	1.44	4.96	5.38
Nd	7.84	9.06	25.78	27.04
Sm	2.91	2.96	6.77	7.15
Eu	0.95	1.10	2.13	2.27
Gd	3.08	3.60	6.41	6.86
Tb	0.46	0.53	0.94	0.99
Dy	2.99	3.49	5.23	5.60
Ho	0.54	0.60	0.91	1.04
Er	1.35	1.51	2.28	2.36
Tm	0.16	0.19	0.27	0.31
Yb	0.99	1.14	1.67	1.67
Lu	0.11	0.15	0.23	0.23
Hf	1.42	1.72	5.65	6.84
Pb			0.16	0.01
Th	0.02	0.01	0.18	0.20
U		0.01	0.02	0.01

Table A5 (continued): Individual clinopyroxene major, trace, and volatile compositions.

	RVV 346-B1b	RVV 346-C1a	RVV 346-D1a	RVV 346-E1a
SiO₂ (wt%)	48.58	46.74	51.14	49.34
TiO₂	1.39	1.63	0.71	1.10
Al₂O₃	6.69	6.72	3.80	5.69
Cr₂O₃	0.87	0.43	0.92	0.42
FeO	5.42	6.19	5.05	5.94
MnO	0.10	0.12	0.11	0.11
MgO	13.79	13.83	16.49	15.32
CaO	22.88	22.93	22.48	22.50
Na₂O	0.58	0.41	0.37	0.37
K₂O	0.01			
NiO			0.04	0.02
Total	100.31	98.99	101.12	100.80
Mg#	0.82	0.80	0.85	0.82
Cr#	0.08	0.04	0.14	0.05
H₂O (ppm)	200.07	301.11	225.42	205.07
Sr	66.9	58.2	34.9	57.2
Y	12.3	10.99	6.08	8.94
Zr	63.9	46.5	13.19	34.4
Nb	0.72	0.43	0.07	0.37
Ba				0.02
La	4.66	3.24	1.09	2.83
Ce	16.88	12.58	4.48	10.73
Pr	2.86	2.05	0.77	1.80
Nd	13.77	11.48	4.39	9.51
Sm	3.85	3.04	1.50	2.69
Eu	1.23	1.01	0.48	0.87
Gd	3.49	3.00	1.37	2.76
Tb	0.51	0.46	0.24	0.38
Dy	2.95	2.71	1.53	2.24
Ho	0.53	0.45	0.24	0.41
Er	1.30	1.12	0.66	0.93
Tm	0.16	0.14	0.07	0.11
Yb	0.92	0.85	0.42	0.62
Lu	0.11	0.10	0.06	0.09
Hf	2.62	2.14	0.66	1.69
Pb	0.01	0.01	0.02	
Th	0.06	0.04	0.01	0.03
U	0.01			

Table A5 (continued): Individual clinopyroxene major, trace, and volatile compositions.

	RVV 346-G1b	RVV 346-H1a	RVV 346-I1a	RVV 370-A1a
SiO₂ (wt%)	46.91	47.23	47.63	50.74
TiO₂	2.05	2.02	1.93	1.05
Al₂O₃	7.81	7.60	7.87	3.66
Cr₂O₃	0.52	0.50	0.36	0.90
FeO	6.49	6.45	6.53	5.22
MnO	0.10	0.08	0.10	0.14
MgO	13.16	13.16	13.34	16.20
CaO	23.41	23.12	23.03	21.68
Na₂O	0.48	0.44	0.49	0.34
K₂O				
NiO	0.05	0.03	0.02	
Total	100.99	100.61	101.30	99.91
Mg#	0.78	0.78	0.78	0.85
Cr#	0.04	0.04	0.03	0.14
H₂O (ppm)	279.36	363.98	300.29	458.14
Sr	71.5	60.02	71.7	42
Y	16.86	8.55	12.87	8.71
Zr	90.8	36.49	63.9	22.51
Nb	1.13	0.38	0.77	0.15
Ba	0.09	0.02		
La	6.46	3.26	4.86	1.69
Ce	23.35	11.68	17.62	6.96
Pr	3.65	1.86	2.84	1.21
Nd	19.50	9.68	15.04	7.00
Sm	5.22	2.58	4.00	2.33
Eu	1.68	0.84	1.37	0.80
Gd	4.65	2.33	3.91	2.52
Tb	0.67	0.37	0.53	0.35
Dy	4.06	2.04	3.18	2.20
Ho	0.72	0.38	0.55	0.37
Er	1.75	0.86	1.32	0.86
Tm	0.22	0.11	0.15	0.10
Yb	1.35	0.64	0.96	0.60
Lu	0.15	0.08	0.13	0.08
Hf	3.71	1.51	2.51	0.99
Pb				0.01
Th	0.09	0.04	0.06	0.02
U				

Table A5 (continued): Individual clinopyroxene major, trace, and volatile compositions.

	RVV 370-B1b	RVV 370-C1a	RVV 370-E1a	RVV 370-F1a
SiO₂ (wt%)	50.45	48.19	50.17	51.19
TiO₂	0.55	1.12	1.10	0.66
Al₂O₃	5.06	5.37	4.59	3.25
Cr₂O₃	0.96	0.92	1.01	1.20
FeO	5.38	5.77	5.64	4.99
MnO	0.15	0.14	0.10	0.12
MgO	15.60	15.44	16.05	16.27
CaO	21.12	21.73	21.81	21.71
Na₂O	0.34	0.37	0.50	0.38
K₂O	0.00			
NiO		0.04	0.02	0.02
Total	99.61	99.09	101.01	99.79
Mg#	0.84	0.83	0.84	0.85
Cr#	0.11	0.10	0.13	0.20
H₂O (ppm)	262.69	486.36	302.67	512.13
Sr	47.1	39.6	41.6	38.11
Y	9.96	9.99	7.44	8.33
Zr	27.7	24.2	17.14	19.26
Nb	0.18	0.16	0.14	0.09
Ba			0.02	
La	2.11	1.50	1.27	1.27
Ce	8.63	6.34	5.41	5.14
Pr	1.49	1.19	0.92	0.94
Nd	8.32	7.38	6.03	5.62
Sm	2.62	2.39	1.95	2.06
Eu	0.88	0.80	0.61	0.71
Gd	2.83	2.56	2.00	2.18
Tb	0.43	0.37	0.29	0.33
Dy	2.34	2.27	1.81	1.95
Ho	0.40	0.43	0.31	0.35
Er	1.05	1.00	0.79	0.86
Tm	0.12	0.12	0.09	0.10
Yb	0.69	0.77	0.52	0.61
Lu	0.10	0.10	0.07	0.07
Hf	1.23	1.15	0.81	0.84
Pb	0.01	0.03		
Th	0.02	0.02	0.02	0.01
U				

Table A5 (continued): Individual clinopyroxene major, trace, and volatile compositions.

	RVV 370-I1a	RPA 367-A1a	RPA 367-A1b	RPA 367-B1c
SiO₂ (wt%)	51.41	47.31	48.05	50.09
TiO₂	0.92	2.04	2.24	1.00
Al₂O₃	4.08	5.86	5.97	4.68
Cr₂O₃	1.05	0.03	-0.01	1.00
FeO	5.34	8.24	8.27	5.60
MnO	0.11	0.20	0.15	0.14
MgO	15.97	13.69	13.17	15.43
CaO	22.01	21.53	21.90	21.36
Na₂O	0.38	0.47	0.47	0.34
K₂O		0.00		
NiO	0.05			
Total	101.33	99.37	100.21	99.63
Mg#	0.84	0.75	0.74	0.83
Cr#	0.15	0.00		0.13
H₂O (ppm)	383.91	198.43	284.42	427.97
Sr	42.17	80.1	78.6	40.1
Y	7.1	19.49	19.6	8.6
Zr	17.32	99.4	98.9	18.46
Nb	0.10	0.61	0.55	0.39
Ba				0.59
La	1.35	5.56	5.54	1.37
Ce	5.80	22.69	22.49	5.50
Pr	1.00	4.00	3.88	0.93
Nd	5.77	22.09	21.46	5.36
Sm	1.95	6.57	6.48	1.85
Eu	0.64	2.04	2.05	0.63
Gd	2.00	6.38	6.52	2.06
Tb	0.30	0.89	0.82	0.31
Dy	1.78	4.95	4.77	2.01
Ho	0.29	0.79	0.81	0.36
Er	0.76	1.91	1.89	0.83
Tm	0.09	0.22	0.22	0.10
Yb	0.51	1.28	1.23	0.61
Lu	0.07	0.16	0.15	0.08
Hf	0.82	3.98	4.14	0.78
Pb		0.03	0.04	0.03
Th	0.01	0.07	0.05	0.02
U	0.01	0.01		

Table A5 (continued): Individual clinopyroxene major, trace, and volatile compositions.

	RPA 367-B1e	RPA 367-C1a	RPA 367-D1a	RPA 367-E1a
SiO₂ (wt%)	50.67	47.70	49.98	50.49
TiO₂	0.61	2.01	1.69	1.22
Al₂O₃	3.43	6.21	3.46	4.25
Cr₂O₃	1.13	0.69	0.00	1.26
FeO	4.66	5.82	7.88	4.96
MnO	0.14	0.10	0.15	0.09
MgO	15.81	14.70	14.78	16.09
CaO	21.91	22.07	22.00	21.93
Na₂O	0.29	0.45	0.43	0.43
K₂O				
NiO		0.01	0.01	0.09
Total	98.65	99.76	100.36	100.81
Mg#	0.86	0.82	0.77	0.85
Cr#	0.18	0.07		0.17
H₂O (ppm)	288.18	185.76	124.81	118.58
Sr	40.2	87.5	76.5	83.6
Y	7.2	12.81	14.76	7.91
Zr	16.38	67.7	63.3	34.3
Nb	0.09	0.42	0.26	0.20
Ba			0.01	0.01
La	1.49	3.81	4.00	2.45
Ce	5.80	15.80	16.22	10.34
Pr	0.95	2.71	2.90	1.76
Nd	6.07	15.00	16.61	9.82
Sm	1.73	4.46	5.25	3.07
Eu	0.58	1.47	1.59	0.97
Gd	1.92	4.45	4.79	2.69
Tb	0.29	0.58	0.69	0.36
Dy	1.65	3.38	3.82	2.12
Ho	0.29	0.53	0.64	0.32
Er	0.71	1.18	1.42	0.76
Tm	0.08	0.15	0.16	0.10
Yb	0.45	0.76	0.92	0.47
Lu	0.06	0.08	0.11	0.06
Hf	0.77	2.87	2.76	1.59
Pb		0.02	0.03	
Th	0.01	0.04	0.02	0.02
U				

Table A5 (continued): Individual clinopyroxene major, trace, and volatile compositions.

	RPA 367-H1a	RPA 367-I1a	RPA 414-A1a	RPA 414-A1b
SiO₂ (wt%)	48.73	52.15	50.78	50.53
TiO₂	1.95	0.75	0.54	1.04
Al₂O₃	5.95	3.92	3.95	4.88
Cr₂O₃	0.75	0.86	0.67	0.62
FeO	5.89	4.89	5.24	5.54
MnO	0.10	0.07	0.09	0.14
MgO	14.25	17.19	16.63	15.35
CaO	22.60	20.65	20.97	21.59
Na₂O	0.46	0.43	0.35	0.33
K₂O			0.00	
NiO	0.05	0.04		
Total	100.73	100.94	99.21	100.01
Mg#	0.81	0.86	0.85	0.83
Cr#	0.08	0.13	0.10	0.08
H₂O (ppm)	240.78	189.40	167.59	168.79
Sr	85.8	56.1	46.4	41.5
Y	14.91	6.88	6.44	5.55
Zr	72.9	16.75	16.73	11.96
Nb	0.43	0.08	0.08	0.07
Ba	0.04	0.03		
La	3.89	1.28	1.16	0.81
Ce	16.05	5.32	5.03	3.90
Pr	2.82	0.94	0.91	0.70
Nd	15.72	5.82	5.22	3.89
Sm	5.03	1.93	1.72	1.34
Eu	1.60	0.63	0.65	0.50
Gd	4.71	2.01	1.75	1.49
Tb	0.66	0.27	0.28	0.21
Dy	3.66	1.69	1.64	1.33
Ho	0.64	0.28	0.25	0.21
Er	1.40	0.67	0.64	0.59
Tm	0.17	0.08	0.08	0.05
Yb	1.10	0.48	0.42	0.41
Lu	0.12	0.05	0.05	0.05
Hf	2.97	0.67	0.75	0.52
Pb				
Th	0.04	0.01	0.01	0.01
U				

Table A5 (continued): Individual clinopyroxene major, trace, and volatile compositions.

	RPA 414-C1a	RPA 414-D1a	RPA 414-E1a	RPA 414-F1a
SiO₂ (wt%)	47.37	47.75	48.77	50.87
TiO₂	2.13	1.69	1.39	0.92
Al₂O₃	6.07	6.20	6.08	4.31
Cr₂O₃	0.37	0.98	0.59	0.76
FeO	6.28	5.90	5.45	5.63
MnO	0.12	0.09	0.11	0.11
MgO	14.58	14.85	14.81	15.98
CaO	21.90	22.27	23.09	21.69
Na₂O	0.54	0.30	0.35	0.42
K₂O				
NiO	0.02	0.01	0.03	0.03
Total	99.39	100.05	100.66	100.71
Mg#	0.81	0.82	0.83	0.84
Cr#	0.04	0.10	0.06	0.11
H₂O (ppm)	224.38	196.78	373.22	391.34
Sr	83.6	61.7	53.4	73.8
Y	13.04	10.55	9.72	10.83
Zr	54.6	41.9	39.1	43.66
Nb	0.30	0.23	0.79	0.26
Ba			0.37	
La	3.01	2.23	3.43	2.37
Ce	12.02	9.42	12.03	9.88
Pr	2.16	1.70	1.97	1.83
Nd	12.80	9.96	10.56	10.23
Sm	3.90	3.01	2.59	3.29
Eu	1.34	0.98	1.03	1.13
Gd	4.01	2.97	2.66	3.53
Tb	0.54	0.45	0.36	0.44
Dy	3.10	2.46	2.16	2.60
Ho	0.55	0.39	0.43	0.47
Er	1.27	0.94	1.13	1.02
Tm	0.15	0.11	0.13	0.12
Yb	0.86	0.69	0.74	0.69
Lu	0.09	0.09	0.10	0.10
Hf	2.39	1.97	1.73	2.02
Pb	0.08	0.01		
Th	0.02	0.03	0.07	0.02
U				

Table A5 (continued): Individual clinopyroxene major, trace, and volatile compositions.

	RPA 414-H1a	RPA 488-A1a	RPA 488-C1a	RPA 488-D1a
SiO₂ (wt%)	50.12	49.50	47.00	47.63
TiO₂	1.43	1.65	1.44	2.01
Al₂O₃	5.29	5.98	5.18	6.68
Cr₂O₃	0.63	0.76	1.23	0.35
FeO	5.57	5.74	5.48	6.70
MnO	0.09	0.14	0.10	0.10
MgO	15.29	15.05	15.31	14.61
CaO	22.03	21.74	21.89	21.51
Na₂O	0.40	0.38	0.39	0.42
K₂O		0.01		
NiO			0.05	0.06
Total	100.89	100.95	98.08	100.05
Mg#	0.83	0.82	0.83	0.80
Cr#	0.07	0.08	0.14	0.03
H₂O (ppm)	335.33	451.32	509.39	359.93
Sr	58.43	71.3	73.1	65
Y	7.47	8.69	9.46	11.09
Zr	22.1	33.9	36.6	44.9
Nb	0.13	0.20	0.23	0.24
Ba				
La	1.37	2.08	2.18	2.19
Ce	5.83	8.95	9.20	9.74
Pr	1.08	1.58	1.62	1.80
Nd	6.29	9.59	9.72	11.27
Sm	2.15	2.91	3.05	3.39
Eu	0.74	1.00	1.03	1.28
Gd	2.16	3.09	3.06	3.53
Tb	0.29	0.41	0.42	0.49
Dy	1.73	2.34	2.50	3.06
Ho	0.31	0.39	0.42	0.48
Er	0.70	0.87	0.91	1.03
Tm	0.08	0.10	0.09	0.12
Yb	0.53	0.59	0.51	0.62
Lu	0.06	0.06	0.08	0.08
Hf	0.97	1.50	1.62	2.35
Pb		0.02	0.02	0.02
Th	0.02	0.02	0.01	0.02
U		0.01	0.00	

Table A5 (continued): Individual clinopyroxene major, trace, and volatile compositions.

	RPA 488-G1a	RPA 488-H1a	RPA 488-I1a	RPA 502-C1a
SiO₂ (wt%)	48.76	49.81	49.24	46.32
TiO₂	1.94	1.54	1.70	2.20
Al₂O₃	6.95	5.58	6.25	6.15
Cr₂O₃	0.46	0.88	1.14	0.72
FeO	6.30	5.78	5.59	6.05
MnO	0.13	0.10	0.10	0.10
MgO	14.44	14.93	14.89	14.39
CaO	22.07	22.13	22.23	22.70
Na₂O	0.46	0.45	0.41	0.48
K₂O				
NiO	0.04	0.02	0.02	0.03
Total	101.56	101.22	101.58	99.14
Mg#	0.80	0.82	0.83	0.81
Cr#	0.04	0.10	0.11	0.07
H₂O (ppm)	548.15	624.86	461.56	431.70
Sr	81.64	72.4	70.8	81.2
Y	13.72	8.89	9.34	11.65
Zr	60.96	31.66	40.47	62.2
Nb	0.34	0.18	0.24	0.45
Ba				0.54
La	3.22	2.00	2.18	3.11
Ce	12.92	8.45	9.02	12.54
Pr	2.41	1.60	1.58	2.29
Nd	14.52	9.36	10.00	12.99
Sm	4.40	2.87	3.19	3.95
Eu	1.47	1.02	1.10	1.30
Gd	4.92	2.96	3.05	3.81
Tb	0.64	0.40	0.41	0.55
Dy	3.54	2.20	2.45	3.04
Ho	0.55	0.35	0.37	0.51
Er	1.36	0.84	0.96	1.23
Tm	0.14	0.09	0.10	0.14
Yb	0.87	0.52	0.59	0.72
Lu	0.11	0.06	0.07	0.09
Hf	2.68	1.40	1.92	2.79
Pb				0.03
Th	0.04	0.01	0.03	0.04
U			0.01	

Table A5 (continued): Individual clinopyroxene major, trace, and volatile compositions.

	RPA 502-E1a	RPA 502-G1a	RPA 502-I1a	MG1001-A1a
SiO₂ (wt%)	48.40	50.78	48.16	50.23
TiO₂	2.05	1.51	1.95	0.50
Al₂O₃	6.96	4.68	7.11	3.34
Cr₂O₃	0.78	0.57	0.55	0.72
FeO	6.18	5.67	6.24	5.11
MnO	0.13	0.09	0.08	0.14
MgO	14.44	15.31	14.07	15.86
CaO	21.82	22.62	21.70	22.10
Na₂O	0.46	0.46	0.50	0.39
K₂O				
NiO		0.04	0.04	
Total	101.20	101.71	100.40	98.38
Mg#	0.81	0.83	0.80	0.85
Cr#	0.07	0.08	0.05	0.13
H₂O (ppm)	245.84	397.43	389.31	495.19
Sr	80.8	80.7	84.3	41.7
Y	11.14	9.25	11.75	6.7
Zr	50.8	43.53	54.7	20.66
Nb	0.35	0.45	0.36	0.10
Ba		0.05	0.05	
La	2.86	2.45	2.91	1.46
Ce	11.86	10.02	11.56	6.29
Pr	2.10	1.79	2.06	1.09
Nd	12.41	10.33	12.30	6.30
Sm	3.83	3.23	3.85	1.82
Eu	1.36	1.10	1.29	0.63
Gd	3.78	3.11	3.72	2.03
Tb	0.50	0.42	0.52	0.28
Dy	2.95	2.31	2.75	1.62
Ho	0.48	0.36	0.48	0.28
Er	1.03	0.83	1.16	0.61
Tm	0.14	0.10	0.12	0.09
Yb	0.77	0.56	0.64	0.45
Lu	0.10	0.06	0.09	0.07
Hf	2.18	1.88	2.28	1.08
Pb				
Th	0.03	0.03	0.03	0.01
U				0.00

Table A5 (continued): Individual clinopyroxene major, trace, and volatile compositions.

	MG1001-B1a	MG1001-B1c	MG1001-C1a	MG1001-D1a
SiO₂ (wt%)	48.12	50.80	50.02	48.98
TiO₂	1.14	0.87	1.10	1.16
Al₂O₃	4.61	4.64	4.79	4.57
Cr₂O₃	0.81	1.06	0.33	1.11
FeO	5.40	5.26	5.47	5.47
MnO	0.14	0.05	0.10	0.10
MgO	14.06	14.84	15.44	15.24
CaO	22.59	22.90	23.44	22.97
Na₂O	0.41	0.34	0.37	0.33
K₂O				
NiO				0.04
Total	97.27	100.74	101.04	99.97
Mg#	0.82	0.83	0.83	0.83
Cr#	0.11	0.13	0.04	0.14
H₂O (ppm)	409.54	414.73	460.39	380.52
Sr	57.2	49.8	45.4	53
Y	7.56	6.72	7.96	6.75
Zr	29.5	19.85	27.5	23.13
Nb	0.19	0.11	0.32	0.14
Ba	0.02		1.10	
La	2.28	1.66	2.07	1.95
Ce	9.33	6.94	8.11	7.46
Pr	1.52	1.21	1.40	1.34
Nd	8.74	6.68	7.25	7.16
Sm	2.36	2.07	2.14	1.87
Eu	0.79	0.68	0.70	0.70
Gd	2.23	2.09	2.17	2.02
Tb	0.31	0.30	0.31	0.26
Dy	1.84	1.80	1.85	1.56
Ho	0.31	0.31	0.33	0.27
Er	0.71	0.70	0.85	0.66
Tm	0.10	0.08	0.09	0.09
Yb	0.56	0.51	0.58	0.46
Lu	0.06	0.07	0.08	0.06
Hf	1.28	1.02	1.28	1.05
Pb	0.03	0.01	0.07	0.02
Th	0.02	0.01	0.03	0.01
U		0.01		

Table A5 (continued): Individual clinopyroxene major, trace, and volatile compositions.

	MG1001-D1c	MG1001-D1d	MG1001-D1e	MG1001-E1a
SiO₂ (wt%)	49.57	49.96	49.23	49.65
TiO₂	0.88	0.87	1.16	1.06
Al₂O₃	3.82	3.64	4.23	4.33
Cr₂O₃	0.96	0.94	0.90	0.88
FeO	4.96	4.81	5.25	5.23
MnO	0.10	0.10	0.09	0.12
MgO	16.02	16.20	15.64	15.72
CaO	22.20	22.56	22.69	22.59
Na₂O	0.33	0.36	0.31	0.39
K₂O				
NiO	0.02	0.04	0.04	0.04
Total	98.86	99.47	99.55	100.01
Mg#	0.85	0.86	0.84	0.84
Cr#	0.14	0.15	0.13	0.12
H₂O (ppm)	303.84	286.18	338.49	369.32
Sr	40.26	41	54.7	47.4
Y	5.82	6.47	7.06	6.55
Zr	13.94	16.4	25.33	20.25
Nb	0.08	0.09	0.12	0.12
Ba				0.02
La	1.24	1.26	1.82	1.46
Ce	5.08	5.36	7.38	6.25
Pr	0.88	1.01	1.23	1.06
Nd	5.04	5.68	7.34	6.13
Sm	1.57	1.80	2.16	1.95
Eu	0.52	0.58	0.70	0.65
Gd	1.62	1.89	1.98	1.86
Tb	0.25	0.25	0.30	0.27
Dy	1.41	1.56	1.76	1.68
Ho	0.24	0.26	0.31	0.27
Er	0.59	0.65	0.73	0.63
Tm	0.07	0.07	0.09	0.09
Yb	0.42	0.40	0.47	0.42
Lu	0.06	0.06	0.07	0.05
Hf	0.59	0.82	1.20	1.03
Pb	0.02		0.01	
Th	0.01		0.01	0.01
U				

Table A5 (continued): Individual clinopyroxene major, trace, and volatile compositions.

	MG1001-E1c	MG1001-F1a	MG1001-G1a
SiO₂ (wt%)	50.14	49.40	49.41
TiO₂	1.29	1.43	1.59
Al₂O₃	4.71	5.13	5.43
Cr₂O₃	0.84	1.00	0.65
FeO	5.37	5.26	5.93
MnO	0.08	0.08	0.08
MgO	15.52	14.62	14.46
CaO	23.01	23.22	23.60
Na₂O	0.33	0.40	0.40
K₂O			
NiO	0.03	0.03	0.05
Total	101.31	100.57	101.61
Mg#	0.84	0.83	0.81
Cr#	0.11	0.12	0.07
H₂O (ppm)	356.03	498.03	451.03
Sr	53.4	55.1	62.7
Y	6.87	7.72	9.9
Zr	24.4	31.66	48.2
Nb	0.17	0.19	0.36
Ba	0.09		
La	1.82	2.15	3.15
Ce	7.35	8.31	12.06
Pr	1.20	1.49	2.01
Nd	6.77	7.85	10.30
Sm	2.05	2.51	3.51
Eu	0.73	0.79	0.99
Gd	2.07	2.31	3.37
Tb	0.31	0.34	0.37
Dy	1.63	1.98	2.22
Ho	0.26	0.34	0.40
Er	0.68	0.74	0.94
Tm	0.08	0.09	0.11
Yb	0.48	0.52	0.72
Lu	0.06	0.07	0.10
Hf	1.21	1.56	2.09
Pb			
Th	0.01	0.02	0.03
U			

Table A5 sample naming scheme: “RVV” stands for Raivavae Island, Austral Islands; “RPA” stands for Rapa Iti Island, Austral Islands; “MG” stands from Mangaia, Cook Islands; Numbers directly following island abbreviation and directly before “-“ refer to whole rock samples from Lassiter et al. [2003], Chan et al. [2009], and Workman et al. [2008]; the letters following the “-“ refer to the indium mount in which pyroxene grains are mounted; the number and letter directly following refer to the grain number of that sample and the spot analyses of that grain. For example: RVV 310-A1a refers to spot analyses a (1 of 2) from pyroxene 1, mounted in “Mount A”, and from whole rock sample RVV 310.

Mg# = $\frac{Mg}{(Mg+Fe)} * 100$; **Cr#** = $\frac{Cr}{(Cr+Al)} * 100$; **FeO*** refers to total iron content (FeO* = FeO + Fe₂O₃); **D_{H₂O}** refers to the calculated partition coefficient of H₂O via the methods from Hauri et al. [2006]: $D_{H_2O} = \left(0.326 * \frac{Al(IV)}{Total(IV)}\right) - 0.0016$

Table A6: Major, trace, and volatile compositions of melts calculated from individual pyroxene phenocrysts.

	RVV 310- A1a	RVV 310- A1b	RVV 310- B1a	RVV 310- C1a	RVV 310- D1a
SiO₂ (wt%)	45.6	45.7	45.5	45.6	45.6
TiO₂	2.7	2.8	2.6	2.7	2.7
Al₂O₃	14.9	15.6	14.7	14.9	15.2
FeO*	11.2	11.0	11.2	11.2	11.1
MnO	0.2	0.3	0.2	0.2	0.2
MgO	7.8	6.6	8.2	7.8	7.4
CaO	11.1	11.3	11.0	11.1	11.2
Na₂O	2.6	2.7	2.5	2.6	2.6
K₂O	0.9	0.9	0.9	0.9	0.9
P₂O₅	0.4	0.4	0.4	0.4	0.4
Mg#	0.6	0.5	0.6	0.6	0.6
H₂O	0.6	0.5	0.4	0.6	0.8
T (°C)	1236	1195	1252	1235	1217
Sr (ppm)	481.48	301.87	414.52	365.12	536.22
Y	20.19	17.89	48.54	28.97	40.15
Zr	110.62	104.18	242.78	115.86	282.72
Nb	8.44	9.06	15.56	7.35	24.17
Ba	0.00	0.00	0.03	0.00	4.37
La	18.54	18.06	29.95	18.93	45.23
Ce	41.43	41.57	74.18	46.95	104.49
Nd	23.53	22.44	48.49	25.23	55.83
Sm	5.63	4.91	13.42	7.31	11.81
Eu	1.86	1.62	4.42	2.39	4.10
Gd	5.59	4.82	14.29	7.61	12.35
Dy	4.68	4.15	12.47	6.63	9.90
Ho	0.81	0.78	1.85	1.16	1.64
Er	2.12	1.74	4.69	2.92	3.89
Tm	0.26	0.22	0.66	0.34	0.46
Yb	1.45	1.39	3.82	1.98	2.94
Lu	0.20	0.16	0.49	0.30	0.41
Hf	1.67	1.36	2.58	1.44	3.71
Pb					0.70
U					

Table A6 (continued): Major, trace, and volatile compositions of melts calculated from individual pyroxene phenocrysts.

	RVV 310- E1a	RVV 310- G1a	RVV 310- H1a	RVV 310- I1a	RVV 318- C1b
SiO₂ (wt%)	45.7	45.6	45.7	45.7	45.2
TiO₂	2.8	2.7	2.8	2.8	2.3
Al₂O₃	15.6	14.9	15.8	15.5	13.3
FeO*	11.0	11.2	11.0	11.1	9.6
MnO	0.3	0.2	0.3	0.2	0.3
MgO	6.6	7.8	6.1	6.8	7.7
CaO	11.3	11.1	11.4	11.3	15.9
Na₂O	2.7	2.6	2.7	2.6	2.0
K₂O	0.9	0.9	0.9	0.9	0.7
P₂O₅	0.4	0.4	0.4	0.4	0.3
Mg#	0.5	0.6	0.5	0.5	0.6
H₂O	0.4	0.7	0.5	0.4	2.6
T (°C)	1195	1232	1177	1203	1177
Sr (ppm)	440.49	432.63	386.04	495.92	356.06
Y	18.91	27.83	20.41	17.33	13.03
Zr	139.77	130.68	201.73	144.43	109.67
Nb	13.10	9.38	16.59	13.22	14.31
Ba	0.00	0.00	0.00	0.00	0.00
La	23.89	19.23	29.68	23.76	27.63
Ce	53.35	46.89	66.56	53.32	56.63
Nd	27.11	27.66	34.55	27.67	25.87
Sm	6.66	7.03	7.61	6.04	4.70
Eu	2.00	2.42	2.26	1.91	1.45
Gd	5.51	7.01	6.43	5.00	4.07
Dy	4.40	6.48	5.11	4.17	3.15
Ho	0.77	1.11	0.84	0.70	0.50
Er	1.84	2.54	2.07	1.66	1.38
Tm	0.21	0.32	0.24	0.18	0.16
Yb	1.31	2.13	1.41	1.23	1.01
Lu	0.16	0.27	0.19	0.18	0.13
Hf	2.01	1.77	2.92	2.04	1.72
Pb					0.15
U					

Table A6 (continued): Major, trace, and volatile compositions of melts calculated from individual pyroxene phenocrysts.

	RVV 318- C1c	RVV 318- C1d	RVV 318- C1g	RVV 318- C1h	RVV 318- C2a
SiO₂ (wt%)	45.2	45.2	45.1	45.1	45.3
TiO₂	2.2	2.3	2.2	2.2	2.4
Al₂O₃	12.9	13.1	12.6	12.6	14.1
FeO*	9.7	9.7	9.8	9.8	9.5
MnO	0.3	0.3	0.3	0.3	0.3
MgO	8.5	8.1	9.2	9.2	6.1
CaO	15.7	15.8	15.5	15.5	16.3
Na₂O	2.0	2.0	1.9	1.9	2.2
K₂O	0.7	0.7	0.7	0.7	0.8
P₂O₅	0.3	0.3	0.3	0.3	0.3
Mg#	0.6	0.6	0.6	0.6	0.6
H₂O	2.0	2.6	1.8	1.7	1.0
T (°C)	1210	1189	1233	1237	1148
Sr (ppm)	513.71	429.05	650.77	683.91	277.78
Y	14.93	16.31	14.63	13.52	17.57
Zr	126.05	142.36	124.30	113.09	159.49
Nb	13.62	26.65	11.91	11.83	21.00
Ba	1.41	1.59	1.24	0.11	1.21
La	31.34	34.45	31.21	29.44	36.31
Ce	68.77	70.12	68.39	62.15	71.15
Nd	30.38	32.19	31.60	28.81	32.33
Sm	5.76	6.04	6.00	5.34	7.11
Eu	1.56	1.67	1.69	1.51	1.79
Gd	4.93	5.08	4.73	4.19	4.74
Dy	3.55	3.64	3.63	3.10	3.99
Ho	0.59	0.66	0.60	0.53	0.70
Er	1.44	1.70	1.38	1.48	1.63
Tm	0.19	0.18	0.20	0.19	0.20
Yb	1.26	1.36	1.08	1.02	1.36
Lu	0.13	0.17	0.15	0.14	0.17
Hf	1.89	2.25	1.94	1.73	2.41
Pb	0.26	0.39	0.32	0.21	0.22
U				0.09	0.16

Table A6 (continued): Major, trace, and volatile compositions of melts calculated from individual pyroxene phenocrysts.

	RVV 318- D1a	RVV 318- E1a	RVV 318- F1a	RVV 318- G1a	RVV 318- H1a
SiO₂ (wt%)	45.3	45.3	45.4	45.3	45.3
TiO₂	2.4	2.4	2.5	2.5	2.5
Al₂O₃	14.0	14.0	14.7	14.5	14.5
FeO*	9.5	9.5	9.3	9.3	9.3
MnO	0.3	0.3	0.3	0.3	0.3
MgO	6.3	6.3	4.8	5.2	5.2
CaO	16.2	16.2	16.6	16.5	16.5
Na₂O	2.2	2.2	2.3	2.2	2.2
K₂O	0.8	0.8	0.8	0.8	0.8
P₂O₅	0.3	0.3	0.3	0.3	0.3
Mg#	0.6	0.6	0.5	0.5	0.5
H₂O	1.5	1.1	2.0	1.7	2.2
T (°C)	1151	1151	1078	1098	1090
Sr (ppm)	298.98	255.05	106.65	158.43	142.79
Y	16.29	16.92	15.63	17.67	16.40
Zr	149.90	118.57	167.37	163.26	180.45
Nb	20.00	11.16	24.07	20.77	26.70
Ba	0.00	0.00	0.07	0.00	0.90
La	32.87	24.34	32.44	32.90	39.64
Ce	64.59	52.38	67.54	66.43	80.96
Nd	29.81	28.19	31.31	30.42	34.91
Sm	6.00	6.34	5.95	6.35	6.78
Eu	1.77	1.98	1.71	1.83	1.85
Gd	4.80	5.10	4.83	4.93	5.02
Dy	3.85	4.30	3.71	4.07	3.63
Ho	0.62	0.67	0.64	0.70	0.69
Er	1.60	1.59	1.44	1.84	1.67
Tm	0.20	0.19	0.20	0.23	0.21
Yb	1.37	1.19	1.24	1.46	1.24
Lu	0.17	0.15	0.19	0.17	0.15
Hf	2.31	1.75	2.63	2.45	2.76
Pb	0.21				
U					

Table A6 (continued): Major, trace, and volatile compositions of melts calculated from individual pyroxene phenocrysts.

	RVV 318- H2a	RVV 318- H2b	RVV 318- H2c	RVV 318- H2d	RVV 318- H2e
SiO₂ (wt%)	45.4	45.3	45.3	45.3	45.2
TiO₂	2.5	2.4	2.5	2.4	2.3
Al₂O₃	14.7	14.1	14.5	14.3	13.3
FeO*	9.3	9.5	9.3	9.4	9.6
MnO	0.3	0.3	0.3	0.3	0.3
MgO	4.8	6.1	5.2	5.7	7.7
CaO	16.6	16.3	16.5	16.4	15.9
Na₂O	2.3	2.2	2.2	2.2	2.0
K₂O	0.8	0.8	0.8	0.8	0.7
P₂O₅	0.3	0.3	0.3	0.3	0.3
Mg#	0.5	0.6	0.5	0.5	0.6
H₂O	2.5	2.8	3.0	2.7	3.2
T (°C)	1069	1113	1079	1100	1160
Sr (ppm)	107.52		110.64	142.87	314.83
Y	13.67		17.72	15.24	19.71
Zr	136.03		185.26	145.95	160.74
Nb	64.17		22.89	19.55	18.91
Ba	75.68		1.33	1.71	1.51
La	36.40		34.91	30.90	37.68
Ce	66.23		72.39	62.22	79.45
Nd	26.60		34.24	28.91	37.46
Sm	4.94		6.65	5.61	7.88
Eu	1.43		1.96	1.76	2.09
Gd	4.08		4.86	4.60	5.56
Dy	3.10		4.47	3.69	4.76
Ho	0.56		0.72	0.62	0.76
Er	1.32		1.85	1.53	2.06
Tm	0.17		0.21	0.20	0.27
Yb	1.13		1.61	1.27	1.43
Lu	0.15		0.20	0.16	0.21
Hf	1.98		2.84	2.45	2.46
Pb					
U					

Table A6 (continued): Major, trace, and volatile compositions of melts calculated from individual pyroxene phenocrysts.

	RVV 318- H2f	RVV 318- I1a	RVV 321- A1a	RVV 321- A1b	RVV 321- B1a
SiO₂ (wt%)	45.3	45.4	41.9	41.8	41.8
TiO₂	2.4	2.5	3.2	3.3	3.3
Al₂O₃	13.9	14.7	15.6	15.9	16.2
FeO*	9.5	9.3	12.9	12.9	12.9
MnO	0.3	0.3	0.3	0.3	0.3
MgO	6.6	4.8	6.3	5.8	5.3
CaO	16.2	16.6	11.4	11.3	11.2
Na₂O	2.1	2.3	3.4	3.5	3.6
K₂O	0.8	0.8	1.2	1.2	1.3
P₂O₅	0.3	0.3	0.5	0.5	0.5
Mg#	0.6	0.5	0.5	0.5	0.4
H₂O	2.6	1.6	2.1	1.9	1.7
T (°C)	1131	1083	1180	1169	1155
Sr (ppm)	200.67	115.71	508.49	338.98	393.97
Y	14.00	15.48	21.25	18.13	20.05
Zr	100.10	170.13	208.40	166.81	191.10
Nb	12.44	23.16	38.37	24.75	32.12
Ba	0.99	1.07	0.00	0.00	0.00
La	29.05	31.86	47.43	34.65	41.40
Ce	56.02	66.35	99.41	73.24	86.02
Nd	24.72	28.50	42.53	33.39	39.76
Sm	4.86	6.03	8.81	7.14	8.07
Eu	1.42	1.71	2.50	2.00	2.34
Gd	4.32	4.91	6.80	5.67	6.45
Dy	3.21	3.49	5.19	4.43	4.79
Ho	0.54	0.60	0.89	0.71	0.85
Er	1.33	1.54	2.29	1.86	1.87
Tm	0.19	0.19	0.26	0.21	0.21
Yb	1.13	1.19	1.53	1.33	1.44
Lu	0.15	0.15	0.22	0.17	0.19
Hf	1.51	2.57	3.14	2.58	2.79
Pb			0.26	0.28	0.31
U		0.19	0.16	0.20	0.19

Table A6 (continued): Major, trace, and volatile compositions of melts calculated from individual pyroxene phenocrysts.

	RVV 321- C1a	RVV 321- D1a	RVV 321- E1a	RVV 321- F1a	RVV 321- G1a
SiO₂ (wt%)	41.8	42.1	41.8	41.8	41.9
TiO₂	3.3	3.1	3.3	3.3	3.2
Al₂O₃	15.9	14.8	16.2	16.2	15.6
FeO*	12.9	12.8	12.9	12.9	12.9
MnO	0.3	0.2	0.3	0.3	0.3
MgO	5.8	7.5	5.3	5.3	6.3
CaO	11.3	11.7	11.2	11.2	11.4
Na₂O	3.5	3.2	3.6	3.6	3.4
K₂O	1.2	1.1	1.3	1.3	1.2
P₂O₅	0.5	0.5	0.5	0.5	0.5
Mg#	0.5	0.5	0.4	0.4	0.5
H₂O	1.4	1.7	1.1	1.5	1.7
T (°C)	1178	1227	1167	1160	1189
Sr (ppm)	530.99	756.47	444.44	397.37	682.22
Y	19.85	19.71	19.06	18.17	19.96
Zr	183.76	144.57	200.73	157.25	200.82
Nb	31.23	30.72	36.01	29.17	34.93
Ba	1.40	18.47	0.00	0.49	0.13
La	39.91	36.89	41.84	32.63	42.63
Ce	85.05	77.39	87.40	72.09	91.30
Nd	38.90	34.09	40.65	33.84	41.00
Sm	8.20	6.85	8.30	6.95	8.29
Eu	2.44	2.11	2.39	2.01	2.54
Gd	6.35	5.61	6.37	5.79	6.68
Dy	4.67	4.65	4.73	4.35	4.97
Ho	0.76	0.78	0.82	0.69	0.77
Er	1.97	1.94	2.02	1.71	1.88
Tm	0.23	0.23	0.22	0.21	0.22
Yb	1.46	1.28	1.34	1.24	1.41
Lu	0.18	0.18	0.20	0.17	0.20
Hf	2.78	2.27	3.10	2.49	3.05
Pb	0.46	0.46			
U	0.25				

Table A6 (continued): Major, trace, and volatile compositions of melts calculated from individual pyroxene phenocrysts.

	RVV 321- H1a	RVV 343- A1a	RVV 343- C1a	RVV 343- F1a	RVV 343- H1a
SiO₂ (wt%)	41.8	47.2	47.2	47.2	47.2
TiO₂	3.3	3.0	3.0	2.9	2.9
Al₂O₃	16.1	14.0	14.0	13.7	13.8
FeO*	12.9	13.6	13.6	13.6	13.6
MnO	0.3	0.2	0.2	0.2	0.2
MgO	5.6	5.9	5.9	6.3	6.2
CaO	11.3	9.6	9.6	9.7	9.7
Na₂O	3.6	3.1	3.1	3.1	3.1
K₂O	1.3	0.8	0.8	0.8	0.8
P₂O₅	0.5	0.4	0.4	0.4	0.4
Mg#	0.5	0.5	0.5	0.5	0.5
H₂O	2.1	0.3	0.2	0.3	0.4
T (°C)	1158	1192	1196	1205	1200
Sr (ppm)	460.21	240.57	241.88	264.24	274.31
Y	24.31	31.57	28.21	27.28	23.82
Zr	277.89	165.65	149.49	125.83	112.29
Nb	44.70	9.03	10.91	7.73	8.55
Ba	0.68	0.00	0.00	0.00	0.00
La	60.59	26.52	20.49	21.49	18.46
Ce	119.28	67.07	50.37	48.44	43.92
Nd	54.86	37.27	28.61	28.77	24.30
Sm	9.79	8.92	7.73	7.57	6.52
Eu	2.96	2.85	2.33	2.45	2.07
Gd	7.71	8.58	7.26	7.42	6.00
Dy	5.96	7.46	6.18	6.59	5.27
Ho	0.96	1.30	1.12	1.10	0.86
Er	2.42	3.39	2.77	2.72	2.37
Tm	0.29	0.38	0.32	0.29	0.31
Yb	1.90	2.27	1.98	2.26	1.81
Lu	0.22	0.30	0.27	0.26	0.24
Hf	3.94	2.44	2.21	1.89	1.64
Pb			0.15		
U					

Table A6 (continued): Major, trace, and volatile compositions of melts calculated from individual pyroxene phenocrysts.

	RVV 343- I1a	RVV 343- I1b	RVV 346- A1a	RVV 346- A1b	RVV 346- B1a
SiO₂ (wt%)	47.2	47.2	43.8	43.8	43.7
TiO₂	3.0	3.0	2.8	2.8	2.7
Al₂O₃	14.3	14.3	17.0	17.0	16.2
FeO*	13.6	13.6	9.7	9.7	10.0
MnO	0.2	0.2	0.3	0.3	0.3
MgO	5.4	5.4	3.5	3.5	5.0
CaO	9.4	9.4	12.6	12.6	12.4
Na₂O	3.2	3.2	3.6	3.6	3.4
K₂O	0.9	0.9	1.1	1.1	1.1
P₂O₅	0.4	0.4	0.5	0.5	0.5
Mg#	0.4	0.4	0.4	0.4	0.5
H₂O	0.3	0.3	0.6	0.5	0.8
T (°C)	1178	1178	1071	1074	1133
Sr (ppm)	216.05	199.89	120.40	126.50	218.12
Y	22.88	25.59	21.46	17.50	13.28
Zr	110.02	144.83	311.67	285.08	127.05
Nb	9.38	11.95	51.13	54.51	14.56
Ba	0.00	0.00	1.35	17.22	0.00
La	18.06	20.63	57.26	50.31	29.72
Ce	42.97	47.12	107.57	95.42	59.93
Nd	23.95	27.66	44.31	37.01	25.20
Sm	6.53	6.64	8.43	7.02	4.93
Eu	1.91	2.20	2.37	1.99	1.47
Gd	5.77	6.73	6.59	5.52	4.08
Dy	5.15	6.00	4.91	4.09	3.19
Ho	0.90	0.99	0.82	0.72	0.50
Er	2.28	2.54	2.10	1.68	1.29
Tm	0.28	0.32	0.25	0.22	0.14
Yb	1.74	2.00	1.61	1.25	0.93
Lu	0.20	0.27	0.23	0.18	0.14
Hf	1.86	2.26	4.07	3.82	1.95
Pb			1.14	0.08	0.16
U		0.32	0.41	0.16	0.17

Table A6 (continued): Major, trace, and volatile compositions of melts calculated from individual pyroxene phenocrysts.

	RVV 346- B1b	RVV 346- C1a	RVV 346- D1a	RVV 346- E1a	RVV 346- G1a
SiO₂ (wt%)	43.6	43.7	43.5	43.6	43.7
TiO₂	2.6	2.6	2.4	2.6	2.6
Al₂O₃	15.3	15.8	14.1	15.3	15.8
FeO*	10.3	10.1	10.8	10.3	10.1
MnO	0.3	0.3	0.3	0.3	0.3
MgO	6.7	5.8	8.9	6.7	5.8
CaO	12.2	12.3	11.8	12.2	12.3
Na₂O	3.2	3.3	2.9	3.2	3.3
K₂O	1.0	1.0	0.9	1.0	1.0
P₂O₅	0.5	0.5	0.4	0.5	0.5
Mg#	0.6	0.5	0.6	0.6	0.5
H₂O	0.6	0.7	1.0	0.6	0.9
T (°C)	1205	1168	1270	1203	1164
Sr (ppm)	552.44	312.23	638.03	466.94	324.73
Y	21.20	16.43	19.45	19.82	15.77
Zr	256.21	159.96	106.29	181.91	163.10
Nb	36.70	19.12	6.07	24.09	23.20
Ba	0.00	0.00	0.00	0.45	0.72
La	49.57	30.25	21.15	38.24	32.02
Ce	98.37	64.09	48.38	79.84	64.19
Nd	41.63	30.18	24.99	36.99	28.60
Sm	8.55	5.86	6.33	7.72	5.92
Eu	2.43	1.75	1.82	2.23	1.72
Gd	6.46	4.81	4.82	6.61	4.67
Dy	5.02	3.99	4.93	4.93	3.61
Ho	0.86	0.64	0.74	0.87	0.64
Er	2.17	1.61	2.06	2.01	1.51
Tm	0.27	0.20	0.23	0.24	0.18
Yb	1.59	1.27	1.33	1.39	1.27
Lu	0.20	0.16	0.20	0.20	0.17
Hf	3.40	2.41	1.59	2.83	2.50
Pb	0.17	0.10	0.51		
U	0.16	0.00			

Table A6 (continued): Major, trace, and volatile compositions of melts calculated from individual pyroxene phenocrysts.

	RVV 346- G1b	RVV 346- H1a	RVV 346- I1a	RVV 370- A1a	RVV 370- B1a
SiO₂ (wt%)	43.7	43.7	43.7	46.8	46.9
TiO₂	2.7	2.7	2.7	2.5	2.5
Al₂O₃	16.2	16.2	16.2	14.0	14.6
FeO*	10.0	10.0	10.0	10.9	10.8
MnO	0.3	0.3	0.3	0.3	0.3
MgO	5.0	5.0	5.0	8.5	7.3
CaO	12.4	12.4	12.4	10.5	10.7
Na₂O	3.4	3.4	3.4	2.5	2.6
K₂O	1.1	1.1	1.1	0.8	0.9
P₂O₅	0.5	0.5	0.5	0.4	0.4
Mg#	0.5	0.5	0.5	0.6	0.6
H₂O	0.6	0.9	0.7	2.2	1.5
T (°C)	1137	1132	1134	1220	1196
Sr (ppm)	260.85	210.38	258.19	470.85	285.38
Y	20.35	10.79	17.26	19.93	15.97
Zr	248.84	104.74	195.71	123.41	77.97
Nb	40.21	14.28	30.55	10.13	5.65
Ba	2.15	0.53	0.00	0.00	0.00
La	49.88	26.14	41.15	23.57	13.02
Ce	97.78	50.87	81.16	53.46	32.58
Nd	41.72	21.60	35.58	28.14	17.61
Sm	8.14	4.20	6.92	6.91	4.62
Eu	2.35	1.22	2.11	2.11	1.40
Gd	6.02	3.15	5.62	6.24	4.10
Dy	4.82	2.53	4.20	5.00	3.52
Ho	0.82	0.45	0.70	0.80	0.60
Er	2.04	1.05	1.71	1.91	1.56
Tm	0.26	0.13	0.20	0.22	0.17
Yb	1.64	0.82	1.29	1.37	1.12
Lu	0.19	0.11	0.18	0.20	0.16
Hf	3.37	1.43	2.54	1.70	1.11
Pb				0.14	
U					

Table A6 (continued): Major, trace, and volatile compositions of melts calculated from individual pyroxene phenocrysts.

	RVV 370- B1b	RVV 370- C1a	RVV 370- E1a	RVV 370- F1a	RVV 370- H1a
SiO₂ (wt%)	46.8	46.9	46.8	46.7	46.9
TiO₂	2.5	2.5	2.5	2.4	2.5
Al₂O₃	14.2	14.6	14.2	13.8	14.6
FeO*	10.9	10.8	10.9	11.0	10.8
MnO	0.3	0.3	0.3	0.3	0.3
MgO	8.0	7.3	8.0	9.0	7.3
CaO	10.6	10.7	10.6	10.4	10.7
Na₂O	2.5	2.6	2.5	2.4	2.6
K₂O	0.8	0.9	0.8	0.8	0.9
P₂O₅	0.4	0.4	0.4	0.4	0.4
Mg#	0.6	0.6	0.6	0.6	0.6
H₂O	1.2	1.4	1.1	2.8	2.4
T (°C)	1227	1197	1231	1221	1180
Sr (ppm)	531.60	317.05	480.92	453.69	335.63
Y	45.65	20.71	15.74	26.08	19.14
Zr	347.12	118.80	86.04	151.30	138.06
Nb	23.47	10.00	8.82	8.53	10.85
Ba	0.00	0.00	0.43	0.00	0.00
La	59.77	19.01	16.36	24.23	24.70
Ce	136.77	44.18	38.45	54.28	55.50
Nd	69.86	26.83	22.37	31.26	31.01
Sm	16.38	6.40	5.33	8.49	6.87
Eu	4.90	1.92	1.50	2.62	2.03
Gd	14.69	5.72	4.57	7.49	6.02
Dy	11.01	4.67	3.79	6.14	4.58
Ho	1.80	0.86	0.63	1.05	0.72
Er	4.74	2.00	1.62	2.64	1.91
Tm	0.56	0.24	0.19	0.31	0.20
Yb	3.15	1.61	1.11	1.91	1.32
Lu	0.44	0.21	0.14	0.24	0.19
Hf	4.23	1.79	1.28	1.97	1.93
Pb	0.37	0.46			
U					

Table A6 (continued): Major, trace, and volatile compositions of melts calculated from individual pyroxene phenocrysts.

	RVV 370- I1a	RPA 367- A1a	RPA 367- A1b	RPA 367- B1c	RPA 367- B1d
SiO₂ (wt%)	46.8	47.3	47.3	46.9	46.9
TiO₂	2.5	3.9	3.9	3.5	3.6
Al₂O₃	14.1	16.8	16.9	15.3	15.4
FeO*	10.9	8.8	8.8	9.3	9.3
MnO	0.3	0.2	0.2	0.2	0.2
MgO	8.3	3.6	3.4	6.5	6.3
CaO	10.5	10.6	10.6	10.3	10.3
Na₂O	2.5	3.2	3.2	2.9	2.9
K₂O	0.8	1.5	1.5	1.4	1.4
P₂O₅	0.4	0.6	0.6	0.6	0.6
Mg#	0.6	0.4	0.4	0.6	0.6
H₂O	1.8	0.5	0.8	1.8	2.5
T (°C)	1221	1064	1051	1169	1135
Sr (ppm)	466.48	114.12	93.57	219.25	184.80
Y	18.32	35.04	32.32	30.30	50.68
Zr	108.73	417.30	377.91	166.91	387.87
Nb	7.73	32.06	26.84	40.21	32.19
Ba	0.00	0.00	0.00	13.11	1.06
La	21.13	61.50	56.59	29.51	62.67
Ce	50.22	137.68	125.64	65.71	144.53
Nd	26.23	69.62	62.08	33.80	73.57
Sm	6.55	15.23	13.76	8.66	17.81
Eu	1.92	4.23	3.88	2.61	5.44
Gd	5.61	12.33	11.54	8.03	15.25
Dy	4.59	8.80	7.76	7.16	13.39
Ho	0.72	1.35	1.26	1.23	2.19
Er	1.92	3.33	3.01	2.87	4.81
Tm	0.24	0.38	0.35	0.36	0.61
Yb	1.31	2.31	2.05	2.15	3.34
Lu	0.18	0.30	0.26	0.30	0.44
Hf	1.59	5.39	5.14	2.08	4.29
Pb		0.42	0.51	0.62	0.50
U	0.15	0.18			

Table A6 (continued): Major, trace, and volatile compositions of melts calculated from individual pyroxene phenocrysts.

	RPA 367- B1e	RPA 367- C1a	RPA 367- D1a	RPA 367- E1a	RPA 367- F1a
SiO₂ (wt%)	46.6	46.9	47.2	46.7	46.9
TiO₂	3.3	3.6	3.8	3.4	3.5
Al₂O₃	14.4	15.6	16.6	14.6	15.2
FeO*	9.7	9.2	8.9	9.6	9.4
MnO	0.2	0.2	0.2	0.2	0.2
MgO	8.2	6.0	4.1	7.9	6.7
CaO	10.1	10.3	10.6	10.1	10.3
Na₂O	2.7	3.0	3.2	2.8	2.9
K₂O	1.3	1.4	1.5	1.3	1.4
P₂O₅	0.5	0.6	0.6	0.5	0.6
Mg#	0.6	0.6	0.5	0.6	0.6
H₂O	1.6	0.5	0.5	0.5	1.2
T (°C)	1264	1173	1091	1243	1183
Sr (ppm)	566.20	478.67	150.83	1050.25	525.19
Y	14.32	21.21	30.66	20.64	38.40
Zr	76.79	259.88	311.52	218.05	429.04
Nb	5.09	20.29	15.67	15.27	30.00
Ba	0.00	0.00	0.27	0.16	0.31
La	18.18	39.04	50.76	38.83	58.56
Ce	38.80	88.57	113.19	90.54	133.45
Nd	21.16	43.57	60.51	45.15	70.68
Sm	4.44	9.51	14.10	10.44	16.50
Eu	1.34	2.80	3.80	2.94	4.83
Gd	4.11	7.91	10.73	7.63	13.36
Dy	3.24	5.52	7.87	5.52	9.47
Ho	0.54	0.83	1.27	0.80	1.49
Er	1.37	1.89	2.86	1.93	3.67
Tm	0.16	0.24	0.32	0.25	0.43
Yb	0.90	1.26	1.92	1.24	2.71
Lu	0.13	0.14	0.24	0.16	0.33
Hf	1.15	3.58	4.32	3.12	5.46
Pb		0.28	0.42		
U					

Table A6 (continued): Major, trace, and volatile compositions of melts calculated from individual pyroxene phenocrysts.

	RPA 367- H1a	RPA 367- I1a	RPA 488- A1a	RPA 488- C1a	RPA 488- D1a
SiO₂ (wt%)	47.0	46.6	44.5	44.5	44.6
TiO₂	3.6	3.3	3.7	3.6	3.8
Al₂O₃	15.8	14.3	14.5	14.3	15.1
FeO*	9.2	9.7	10.0	10.0	9.7
MnO	0.2	0.2	0.2	0.2	0.2
MgO	5.6	8.5	6.6	7.0	5.3
CaO	10.4	10.1	12.0	11.9	12.4
Na₂O	3.0	2.7	2.1	2.1	2.2
K₂O	1.4	1.3	1.2	1.2	1.2
P₂O₅	0.6	0.5	0.5	0.5	0.6
Mg#	0.5	0.6	0.6	0.6	0.5
H₂O	0.7	1.1	1.5	1.3	0.9
T (°C)	1154	1248	1171	1187	1133
Sr (ppm)	380.32	784.62	426.95	530.09	232.23
Y	24.87	30.04	17.99	22.39	19.99
Zr	282.12	197.29	166.18	208.31	189.05
Nb	21.03	10.38	12.38	16.11	12.65
Ba	0.81	0.70	0.00	0.00	0.00
La	40.14	34.27	26.30	31.41	24.31
Ce	90.63	80.00	62.24	73.07	59.21
Nd	45.99	46.34	34.81	40.42	35.61
Sm	10.81	11.43	7.78	9.37	7.88
Eu	3.08	3.32	2.38	2.83	2.65
Gd	8.43	9.88	6.90	7.84	6.84
Dy	6.02	7.55	4.80	5.89	5.45
Ho	1.01	1.21	0.77	0.95	0.82
Er	2.25	2.87	1.74	2.09	1.80
Tm	0.27	0.34	0.21	0.20	0.21
Yb	1.85	2.10	1.23	1.21	1.13
Lu	0.21	0.24	0.12	0.19	0.15
Hf	3.73	2.20	2.33	2.89	3.19
Pb			0.29	0.39	0.28
U			0.19	0.10	

Table A6 (continued): Major, trace, and volatile compositions of melts calculated from individual pyroxene phenocrysts.

	RPA 488- F1a	RPA 488- G1a	RPA 488- H1a	RPA 488- I1a	RPA 502- C1a
SiO₂ (wt%)	44.5	44.6	44.5	44.5	44.7
TiO₂	3.6	3.8	3.7	3.7	4.1
Al₂O₃	14.3	15.0	14.6	14.5	15.5
FeO*	10.0	9.8	9.9	10.0	11.7
MnO	0.2	0.2	0.2	0.2	0.2
MgO	7.0	5.5	6.4	6.6	6.9
CaO	11.9	12.3	12.1	12.0	9.9
Na₂O	2.1	2.2	2.1	2.1	2.9
K₂O	1.2	1.2	1.2	1.2	1.4
P₂O₅	0.5	0.6	0.5	0.5	0.6
Mg#	0.6	0.5	0.6	0.6	0.5
H₂O	1.6	1.5	2.1	1.4	1.0
T (°C)	1184	1130	1151	1172	1211
Sr (ppm)	483.24	292.30	347.41	429.35	755.35
Y	21.16	26.37	20.88	19.38	19.61
Zr	195.24	275.34	178.67	198.87	243.06
Nb	14.97	19.27	12.69	14.82	22.08
Ba	1.43	0.00	0.00	0.00	12.74
La	31.28	37.93	28.50	27.58	32.36
Ce	67.99	83.57	66.59	62.90	71.41
Nd	39.40	48.91	38.61	36.39	38.35
Sm	8.47	10.91	8.74	8.55	8.56
Eu	2.73	3.26	2.77	2.64	2.52
Gd	7.32	10.18	7.53	6.82	6.88
Dy	5.39	6.73	5.14	5.04	5.05
Ho	0.83	1.01	0.78	0.73	0.81
Er	2.02	2.53	1.93	1.93	2.00
Tm	0.22	0.26	0.20	0.20	0.23
Yb	1.35	1.69	1.22	1.23	1.22
Lu	0.15	0.21	0.16	0.15	0.15
Hf	3.00	3.88	2.48	3.00	3.54
Pb					0.34
U				0.17	

Table A6 (continued): Major, trace, and volatile compositions of melts calculated from individual pyroxene phenocrysts.

	RPA 502- D1a	RPA 502- E1a	RPA 502- G1a	RPA 502- I1a	MG1001- A1a
SiO₂ (wt%)	44.7	44.7	44.6	44.7	43.2
TiO₂	4.2	4.1	3.9	4.1	2.6
Al₂O₃	15.8	15.5	14.9	15.7	11.2
FeO*	11.7	11.7	11.8	11.7	12.8
MnO	0.2	0.2	0.2	0.2	0.2
MgO	6.4	6.9	8.0	6.6	10.1
CaO	9.9	9.9	9.9	9.9	14.8
Na₂O	3.0	2.9	2.8	2.9	2.3
K₂O	1.5	1.4	1.4	1.4	0.6
P₂O₅	0.6	0.6	0.6	0.6	0.3
Mg#	0.5	0.5	0.6	0.5	0.6
H₂O	1.0	0.7	1.6	1.1	2.5
T (°C)	1193	1219	1232	1197	1264
Sr (ppm)	638.97	798.42	992.62	666.93	887.23
Y	18.01	21.05	22.29	22.14	31.25
Zr	229.81	225.18	252.79	241.71	264.87
Nb	19.60	19.44	31.34	19.94	12.97
Ba	0.91	0.00	1.20	1.08	0.00
La	32.17	33.18	35.92	33.64	42.05
Ce	71.90	75.49	81.00	73.35	101.62
Nd	37.92	41.11	43.75	40.62	53.94
Sm	8.55	9.34	10.11	9.36	11.60
Eu	2.53	2.95	3.07	2.79	3.56
Gd	6.89	7.69	8.12	7.54	10.74
Dy	4.63	5.52	5.54	5.12	7.75
Ho	0.69	0.85	0.83	0.86	1.30
Er	1.63	1.89	1.94	2.12	2.80
Tm	0.18	0.25	0.23	0.23	0.39
Yb	1.04	1.46	1.34	1.21	2.10
Lu	0.13	0.20	0.15	0.17	0.32
Hf	3.22	3.10	3.41	3.24	3.78
Pb	0.30				
U					

Table A6 (continued): Major, trace, and volatile compositions of melts calculated from individual pyroxene phenocrysts.

	MG1001- A1b	MG1001- B1a	MG1001- B1c	MG1001- C1a	MG1001- D1a
SiO₂ (wt%)	43.2	43.1	43.1	43.1	43.1
TiO₂	2.6	2.8	2.7	2.7	2.7
Al₂O₃	11.3	11.9	11.7	11.7	11.7
FeO*	12.8	12.9	12.9	12.9	12.9
MnO	0.2	0.2	0.2	0.2	0.2
MgO	9.9	8.6	9.1	9.1	9.1
CaO	14.8	15.1	15.0	15.0	15.0
Na₂O	2.3	2.4	2.4	2.4	2.4
K₂O	0.6	0.7	0.7	0.7	0.7
P₂O₅	0.4	0.4	0.4	0.4	0.4
Mg#	0.6	0.6	0.6	0.6	0.6
H₂O	2.2	1.5	1.9	1.6	1.2
T (°C)	1265	1244	1249	1256	1265
Sr (ppm)	1132.35	890.97	852.74	822.46	1029.13
Y	22.32	17.02	18.37	18.04	13.76
Zr	242.31	158.77	133.13	149.13	111.42
Nb	24.62	12.65	9.04	21.07	8.26
Ba	3.35	0.55	0.00	29.18	0.00
La	41.85	31.28	27.64	28.56	24.31
Ce	91.79	70.52	63.73	61.67	51.10
Nd	41.66	34.55	32.22	28.85	25.58
Sm	8.64	6.88	7.39	6.28	4.92
Eu	2.74	2.06	2.16	1.83	1.65
Gd	7.61	5.43	6.22	5.32	4.44
Dy	5.33	4.12	4.92	4.17	3.15
Ho	0.85	0.68	0.81	0.72	0.52
Er	2.17	1.55	1.87	1.86	1.30
Tm	0.22	0.21	0.21	0.21	0.17
Yb	1.68	1.26	1.40	1.31	0.95
Lu	0.21	0.15	0.18	0.19	0.14
Hf	3.48	2.17	2.10	2.18	1.61
Pb	0.35	0.44	0.27	1.15	0.30
U			0.13		

Table A6 (continued): Major, trace, and volatile compositions of melts calculated from individual pyroxene phenocrysts.

	MG1001- D1b	MG1001- D1c	MG1001- D1d	MG1001- D1e	MG1001- E1a
SiO₂ (wt%)	43.2	43.2	43.3	43.2	43.2
TiO₂	2.6	2.6	2.5	2.6	2.6
Al₂O₃	11.2	11.1	10.9	11.3	11.3
FeO*	12.8	12.7	12.7	12.8	12.8
MnO	0.2	0.2	0.2	0.2	0.2
MgO	10.1	10.4	10.8	9.9	9.9
CaO	14.8	14.8	14.7	14.8	14.8
Na₂O	2.3	2.2	2.2	2.3	2.3
K₂O	0.6	0.6	0.6	0.6	0.6
P₂O₅	0.3	0.3	0.3	0.4	0.4
Mg#	0.6	0.6	0.6	0.6	0.6
H₂O	1.4	1.2	1.1	1.2	1.3
T (°C)	1289	1298	1311	1288	1284
Sr (ppm)	1321.24	1160.23	1357.62	1370.93	1161.76
Y	16.35	15.10	16.25	13.82	14.07
Zr	125.18	88.06	99.82	116.73	103.42
Nb	8.90	6.14	6.62	7.01	7.48
Ba	0.00	0.00	0.00	0.00	0.48
La	24.84	19.57	19.27	21.82	19.12
Ce	57.01	44.25	45.16	48.58	45.09
Nd	29.31	23.03	25.10	25.18	23.11
Sm	6.55	5.31	5.88	5.46	5.42
Eu	1.81	1.56	1.68	1.57	1.61
Gd	5.09	4.57	5.15	4.17	4.31
Dy	4.15	3.65	3.89	3.41	3.59
Ho	0.64	0.60	0.63	0.57	0.54
Er	1.84	1.50	1.58	1.39	1.31
Tm	0.18	0.18	0.18	0.16	0.19
Yb	1.28	1.09	1.02	0.93	0.91
Lu	0.15	0.15	0.15	0.13	0.12
Hf	1.98	1.14	1.54	1.76	1.67
Pb	0.27	0.36		0.17	
U					

Table A6 (continued): Major, trace, and volatile compositions of melts calculated from individual pyroxene phenocrysts.

	MG1001-E1b	MG1001-E1c	MG1001-F1a	MG1001-G1a
SiO₂ (wt%)	43.2	43.1	43.1	43.0
TiO₂	2.6	2.7	2.7	2.8
Al₂O₃	11.2	11.6	11.7	12.2
FeO*	12.8	12.8	12.9	13.0
MnO	0.2	0.2	0.2	0.2
MgO	10.1	9.4	9.1	8.0
CaO	14.8	14.9	15.0	15.2
Na₂O	2.3	2.3	2.4	2.5
K₂O	0.6	0.7	0.7	0.7
P₂O₅	0.3	0.4	0.4	0.4
Mg#	0.6	0.6	0.6	0.5
H₂O	1.7	1.3	1.7	1.4
T (°C)	1281	1271	1255	1229
Sr (ppm)	1088.45	1117.15	987.46	802.82
Y	16.39	13.12	13.55	16.05
Zr	124.82	109.42	129.44	180.86
Nb	9.77	9.27	9.90	17.32
Ba	0.00	2.49	0.00	0.00
La	21.33	21.30	23.28	31.66
Ce	53.09	47.27	49.26	66.30
Nd	28.05	22.66	24.15	29.30
Sm	5.94	5.05	5.68	7.33
Eu	1.88	1.61	1.59	1.85
Gd	5.13	4.25	4.35	5.86
Dy	3.88	3.09	3.43	3.55
Ho	0.62	0.48	0.56	0.62
Er	1.65	1.25	1.26	1.47
Tm	0.22	0.15	0.15	0.17
Yb	1.11	0.93	0.92	1.18
Lu	0.15	0.12	0.12	0.17
Hf	1.75	1.73	2.06	2.55
Pb				
U				

Sample naming for **Table A6** follows the same scheme as for Table A5, however compositions presented in Table A6 refer to compositions of melts calculated from pyroxene phenocrysts.

Melt major element compositions calculated by subtracting olivine and pyroxene phenocryst in their observed abundances from whole rock compositions.

Melt trace element compositions calculated using pyroxene/melt partition coefficients calculated from the program BigD.

Melt H₂O concentrations calculated using parameters outlined in Hauri et al. [2006] (see Table A5 information).

References

- Aubaud, C., Withers, A. C., Hirschmann, M. M., Guan, Y., Leshin, L. A., Mackwell, S. J., & Bell, D. R. (2007). Intercalibration of FTIR and SIMS for hydrogen measurements in glasses and nominally anhydrous minerals. *American Mineralogist*, 92(5-6), 811-828.
- Berlo, K., Stix, J., Roggensack, K., & Ghaleb, B. (2012). A tale of two magmas, Fuego, Guatemala. *Bulletin of volcanology*, 74(2), 377-390.
- Bizimis, M., & Peslier, A. H. (2015). Water in Hawaiian garnet pyroxenites: Implications for water heterogeneity in the mantle. *Chemical Geology*, 397, 61-75.
- Bucholz, C. E., Gaetani, G. A., Behn, M. D., & Shimizu, N. (2013). Post-entrapment modification of volatiles and oxygen fugacity in olivine-hosted melt inclusions. *Earth and Planetary Science Letters*, 374, 145-155.
- Cabral, R. A., Jackson, M. G., Koga, K. T., Rose-Koga, E. F., Hauri, E. H., Whitehouse, M. J., ... & Kelley, K. A. (2014). Volatile cycling of H₂O, CO₂, F, and Cl in the HIMU mantle: A new window provided by melt inclusions from oceanic hot spot lavas at Mangaia, Cook Islands. *Geochemistry, Geophysics, Geosystems*, 15(11), 4445-4467.
- Cabral, R. A., Jackson, M. G., Rose-Koga, E. F., Koga, K. T., Whitehouse, M. J., Antonelli, M. A., ... & Hauri, E. H. (2013). Anomalous sulphur isotopes in plume lavas reveal deep mantle storage of Archaean crust. *Nature*, 496(7446), 490-493.
- Cervantes, P., & Wallace, P. J. (2003). Role of H₂O in subduction-zone magmatism: new insights from melt inclusions in high-Mg basalts from central Mexico. *Geology*, 31(3), 235-238.
- Chan, L. H., Lassiter, J. C., Hauri, E. H., Hart, S. R., & Blusztajn, J. (2009). Lithium isotope systematics of lavas from the Cook–Austral Islands: constraints on the origin of HIMU mantle. *Earth and Planetary Science Letters*, 277(3), 433-442.
- Chase, C. G. (1981). Oceanic island Pb: two-stage histories and mantle evolution. *Earth and Planetary Science Letters*, 52(2), 277-284.
- Chauvel, C., Hofmann, A. W., & Vidal, P. (1992). HIMU-EM: the French Polynesian connection. *Earth and Planetary Science Letters*, 110(1-4), 99-119.
- Chen, Y., A. Provost, P. Schiano, and N. Cluzel (2011), The rate of water loss from olivine-hosted melt inclusions, *Contrib. Mineral. Petrol.*, 162(3), 625–636, doi:10.1007/s00410-011-0616-5.
- Coombes, C. J. (1972). The melting of small particles of lead and indium. *Journal of Physics F: Metal Physics*, 2(3), 441.

- Danyushevsky, L. V., S. M. Eggins, T. J. Falloon, and D. M. Christie (2000), H₂O abundance in depleted to moderately enriched mid-ocean ridge magmas. Part I: Incompatible behaviour, implications for mantle storage, and origin of regional variations, *J. Petrol.*, **41**, 1329–1364.
- Dasgupta, R., Hirschmann, M. M., & Stalker, K. (2006). Immiscible transition from carbonate-rich to silicate-rich melts in the 3 GPa melting interval of eclogite+CO₂ and genesis of silica-undersaturated ocean island lavas. *Journal of Petrology*, *47*(4), 647-671.
- Demouchy, S., Jacobsen, S. D., Gaillard, F., & Stern, C. R. (2006). Rapid magma ascent recorded by water diffusion profiles in mantle olivine. *Geology*, *34*(6), 429-432.
- Dixon, J. E., & Stolper, E. M. (1995). An experimental study of water and carbon dioxide solubilities in mid-ocean ridge basaltic liquids. Part II: applications to degassing. *Journal of Petrology*, *36*(6), 1633-1646.
- Dixon, J. E., Clague, D. A., Wallace, P., & Poreda, R. (1997). Volatiles in alkalic basalts from the North Arch Volcanic Field, Hawaii: extensive degassing of deep submarine-erupted alkalic series lavas. *Journal of Petrology*, *38*(7), 911-939.
- Dixon, J. E., & Clague, D. A. (2001). Volatiles in basaltic glasses from Loihi Seamount, Hawaii: Evidence for a relatively dry plume component. *Journal of Petrology*, *42*(3), 627-654.
- Dixon, J. E., Leist, L., Langmuir, C., & Schilling, J. G. (2002). Recycled dehydrated lithosphere observed in plume-influenced mid-ocean-ridge basalt. *Nature*, *420*(6914), 385-389.
- Dixon, J. E., Clague, D. A., Wallace, P., & Poreda, R. (1997). Volatiles in alkalic basalts from the North Arch Volcanic Field, Hawaii: extensive degassing of deep submarine-erupted alkalic series lavas. *Journal of Petrology*, *38*(7), 911-939.
- Douglass, J., Schilling, J. G., Kingsley, R. H., & Small, C. (1995). Influence of the Discovery and Shona mantle plumes on the southern Mid-Atlantic Ridge: Rare earth evidence. *Geophysical research letters*, *22*(21), 2893-2896.
- Douglass, J., J.-G. Schilling, and D. Fontignie (1999), Plume-ridge interactions of the discovery and Shona mantle plumes with the southern Mid-Atlantic Ridge (40 – 55 S), *J. Geophys. Res.*, *104*, 2941–2962.
- Dupuy, C., Liotard, J. M., & Dostal, J. (1992). Zr/Hf fractionation in intraplate basaltic rocks: carbonate metasomatism in the mantle source. *Geochimica et Cosmochimica Acta*, *56*(6), 2417-2423.
- Farquhar, J., Zerkle, A. L., & Bekker, A. (2011). Geological constraints on the origin of oxygenic photosynthesis. *Photosynthesis research*, *107*(1), 11-36.
- Farquhar, J., Bao, H., & Thiemens, M. (2000). Atmospheric influence of Earth's earliest sulfur cycle. *Science*, *289*(5480), 756-758.

- Ford, C. E., Russell, D. G., Groven, J. A., & Fisk, M. R. (1983). Distribution coefficients of Mg²⁺, Fe²⁺, Ca²⁺ and Mn²⁺ between olivine and melt. *J. Petrol*, *24*, 256-265.
- Gao, R., Lassiter, J. C., & Ramirez, G. (2017). Origin of temporal compositional trends in monogenetic vent eruptions: Insights from the crystal cargo in the Papoose Canyon sequence, Big Pine Volcanic Field, CA. *Earth and Planetary Science Letters*, *457*, 227-237.
- Hart, S. R., & Zindler, A. (1986). In search of a bulk-Earth composition. *Chemical Geology*, *57*(3-4), 247-267.
- Hauri, E. H., & Hart, S. R. (1993). ReOs isotope systematics of HIMU and EMII oceanic island basalts from the south Pacific Ocean. *Earth and Planetary Science Letters*, *114*(2-3), 353-371.
- Hauri, E. H., Shimizu, N., Dieu, J. J., & Hart, S. R. (1993). Evidence for hotspot-related carbonatite metasomatism in the oceanic upper mantle. *Nature*, *365*(6443), 221-227.
- Hauri, E. H. (1996). Major-element variability in the Hawaiian mantle plume. *Nature*, *382*(6590), 415.
- Hauri, E. H. (2002). Osmium isotopes and mantle convection. *Philosophical Transactions of the Royal Society of London A: Mathematical, Physical and Engineering Sciences*, *360*(1800), 2371-2382.
- Hauri, E. H., Gaetani, G. A., & Green, T. H. (2006). Partitioning of water during melting of the Earth's upper mantle at H₂O-undersaturated conditions. *Earth and Planetary Science Letters*, *248*(3), 715-734.
- Herzberg, C., Cabral, R. A., Jackson, M. G., Vidito, C., Day, J. M. D., & Hauri, E. H. (2014). Phantom Archean crust in Mangaia hotspot lavas and the meaning of heterogeneous mantle. *Earth and Planetary Science Letters*, *396*, 97-106.
- Hirschmann, M. M., Aubaud, C., & Withers, A. C. (2005). Storage capacity of H₂O in nominally anhydrous minerals in the upper mantle. *Earth and Planetary Science Letters*, *236*(1), 167-181.
- Hirth, G., & Kohlstedt, D. L. (1996). Water in the oceanic upper mantle: implications for rheology, melt extraction and the evolution of the lithosphere. *Earth and Planetary Science Letters*, *144*(1-2), 93-108.
- Hofmann, A. W., & White, W. M. (1982). Mantle plumes from ancient oceanic crust. *Earth and Planetary Science Letters*, *57*(2), 421-436.
- Hofmann, A. W., Jochum, K. P., Seufert, M., & White, W. M. (1986). Nb and Pb in oceanic basalts: new constraints on mantle evolution. *Earth and Planetary Science Letters*, *79*(1-2), 33-45.

- Hofmann, A. W. (1988). Chemical differentiation of the Earth: the relationship between mantle, continental crust, and oceanic crust. *Earth and Planetary Science Letters*, 90(3), 297-314.
- Jackson, M. G., Hart, S. R., Koppers, A. A., Staudigel, H., Konter, J., Blusztajn, J., ... & Russell, J. A. (2007). The return of subducted continental crust in Samoan lavas. *Nature*, 448(7154), 684-687.
- Jackson, M. G., & Dasgupta, R. (2008). Compositions of HIMU, EM1, and EM2 from global trends between radiogenic isotopes and major elements in ocean island basalts. *Earth and Planetary Science Letters*, 276(1), 175-186.
- Jackson, M. G., Weis, D., & Huang, S. (2012). Major element variations in Hawaiian shield lavas: Source features and perspectives from global ocean island basalt (OIB) systematics. *Geochemistry, Geophysics, Geosystems*, 13(9).
- Jackson, M. G., Koga, K. T., Price, A., Konter, J. G., Koppers, A. A. P., Finlayson, V. A., ... & Kendrick, M. A. (2015). Deeply dredged submarine HIMU glasses from the Tuvalu Islands, Polynesia: Implications for volatile budgets of recycled oceanic crust. *Geochemistry, Geophysics, Geosystems*, 16(9), 3210-3234.
- Jarosewich, E., Nelen, J. A., & Norberg, J. A. (1980). Reference samples for electron microprobe analysis. *Geostandards Newsletter*, 4(1), 43-47.
- Johnston, D. T. (2011). Multiple sulfur isotopes and the evolution of Earth's surface sulfur cycle. *Earth-Science Reviews*, 106(1), 161-183.
- Kelley, K. A., Plank, T., Newman, S., Stolper, E. M., Grove, T. L., Parman, S., & Hauri, E. H. (2010). Mantle melting as a function of water content beneath the Mariana Arc. *Journal of Petrology*, 51(8), 1711-1738.
- Kendrick, M. A., M. G. Jackson, A. J. R. Kent, E. H. Hauri, P. J. Wallace, and J. Woodhead (2014), Contrasting behaviours of CO₂, S, H₂O and halogens (F, Cl, Br, and I) in enriched-mantle melts from Pitcairn and Society seamounts, *Chem. Geol.*, 370, 69–81, doi:10.1016/j.chemgeo.2014.01.019.
- Kendrick, M. A., Hémond, C., Kamenetsky, V. S., Danyushevsky, L., Devey, C. W., Rodemann, T., ... & Perfit, M. R. (2017). Seawater cycled throughout Earth's mantle in partially serpentinized lithosphere. *Nature Geoscience*.
- Klein, E. M., & Langmuir, C. H. (1987). Global correlations of ocean ridge basalt chemistry with axial depth and crustal thickness. *Journal of Geophysical Research: Solid Earth*, 92(B8), 8089-8115.
- Koleszar, A. M., Saal, A. E., Hauri, E. H., Nagle, A. N., Liang, Y., & Kurz, M. D. (2009). The volatile contents of the Galapagos plume; evidence for H₂O and F open system behavior in melt inclusions. *Earth and Planetary Science Letters*, 287(3), 442-452.

- Lassiter, J. C., Hauri, E. H., Nikogosian, I. K., & Barszczus, H. G. (2002). Chlorine–potassium variations in melt inclusions from Raivavae and Rapa, Austral Islands: constraints on chlorine recycling in the mantle and evidence for brine-induced melting of oceanic crust. *Earth and Planetary Science Letters*, 202(3), 525-540.
- Lassiter, J. C., Blichert-Toft, J., Hauri, E. H., & Barszczus, H. G. (2003). Isotope and trace element variations in lavas from Raivavae and Rapa, Cook–Austral islands: constraints on the nature of HIMU-and EM-mantle and the origin of mid-plate volcanism in French Polynesia. *Chemical Geology*, 202(1), 115-138.
- Lloyd, A. S., Plank, T., Ruprecht, P., Hauri, E. H., & Rose, W. (2013). Volatile loss from melt inclusions in pyroclasts of differing sizes. *Contributions to Mineralogy and Petrology*, 165(1), 129-153.
- Mackwell, S. J., & Kohlstedt, D. L. (1990). Diffusion of hydrogen in olivine: implications for water in the mantle. *Journal of Geophysical Research: Solid Earth*, 95(B4), 5079-5088.
- McDonough, W. F., & Sun, S. S. (1995). The composition of the Earth. *Chemical geology*, 120(3-4), 223-253.
- McKenzie, D., & O'nions, R. K. (1983). Mantle reservoirs and ocean island basalts. *Nature*, 301, 229-231.
- McKenzie, D. A. N., & O'nions, R. K. (1991). Partial melt distributions from inversion of rare earth element concentrations. *Journal of Petrology*, 32(5), 1021-1091.
- Métrich, N., Allard, P., Bertagnini, A., Di Muro, A. (2011). Comment on 'Conduit convection, magma mixing, and melt inclusion trends at persistently degassing volcanoes' by F. Witham EPSL (2011) 301, 345-352. *Earth and Planetary Science Letters*, 306, 306-308, doi:10.1016/j.epsl.2010.11.017
- Métrich, N., Zanon, V., Créon, L., Hildenbrand, A., Moreira, M., & Marques, F. O. (2014). Is the 'Azores hotspot' a wet spot? Insights from the geochemistry of fluid and melt inclusions in olivine of Pico basalts. *Journal of Petrology*, 55(2), 377-393.
- Michael, P. J., and Schilling, J.-G. (1989), Chlorine in mid-ocean ridge magmas: Evidence for assimilation of seawater-influenced components, *Geochim. Cosmochim. Acta*, 53, 3131–3143.
- Michael, P. (1995). Regionally distinctive sources of depleted MORB: Evidence from trace elements and H₂O. *Earth and Planetary Science Letters*, 131(3-4), 301-320.
- Mosenfelder, J. L., & Rossman, G. R. (2013). Analysis of hydrogen and fluorine in pyroxenes: I. Orthopyroxene. *American Mineralogist*, 98(5-6), 1026-1041.
- Mosenfelder, J. L., & Rossman, G. R. (2013). Analysis of hydrogen and fluorine in pyroxenes: II. Clinopyroxene. *American Mineralogist*, 98(5-6), 1042-1054.

- Neumann, E. R., Wulff-Pedersen, E., Pearson, N. J., & Spencer, E. A. (2002). Mantle xenoliths from Tenerife (Canary Islands): evidence for reactions between mantle peridotites and silicic carbonatite melts inducing Ca metasomatism. *Journal of Petrology*, *43*(5), 825-857.
- Nielsen, R. L. (1992). BIGD. FOR: a FORTRAN program to calculate trace-element partition coefficients for natural mafic and intermediate composition magmas. *Computers & Geosciences*, *18*(7), 773-788.
- Putirka, K. (1999). Melting depths and mantle heterogeneity beneath Hawaii and the East Pacific Rise: Constraints from Na/Ti and rare earth element ratios. *Journal of Geophysical Research: Solid Earth*, *104*(B2), 2817-2829.
- Putirka, K. D., Perfit, M., Ryerson, F. J., & Jackson, M. G. (2007). Ambient and excess mantle temperatures, olivine thermometry, and active vs. passive upwelling. *Chemical Geology*, *241*(3), 177-206.
- Saal, A. E., Hart, S. R., Shimizu, N., Hauri, E. H., & Layne, G. D. (1998). Pb isotopic variability in melt inclusions from oceanic island basalts, Polynesia. *Science*, *282*(5393), 1481-1484.
- Sandwell, D. T., & Smith, W. H. (1997). Marine gravity anomaly from Geosat and ERS 1 satellite altimetry. *Journal of Geophysical Research: Solid Earth*, *102*(B5), 10039-10054.
- Simons, K., Dixon, J., Schilling, J. G., Kingsley, R., & Poreda, R. (2002). Volatiles in basaltic glasses from the Easter-Salas y Gomez Seamount Chain and Easter Microplate: Implications for geochemical cycling of volatile elements. *Geochemistry, Geophysics, Geosystems*, *3*(7), 1-29.
- Spilliaert, N., Allard, P., Métrich, N., & Sobolev, A. V. (2006). Melt inclusion record of the conditions of ascent, degassing, and extrusion of volatile-rich alkali basalt during the powerful 2002 flank eruption of Mount Etna (Italy). *Journal of Geophysical Research: Solid Earth*, *111*(B4).
- Staudigel, H., T. Plank, B. White, and H. Schmincke (1996). Geochemical fluxes during seafloor alteration of the basaltic upper oceanic crust: DSDP Sites 417 and 418: Subduction: Top to Bottom, *Geophys. Monogr.*, *96*, 19-38.
- Szramek, L. A. (2010). Basaltic Volcanism: Deep mantle recycling, plinian eruptions, and cooling-induced crystallization (PhD Dissertation). The University of Texas at Austin, USA.
- Wade, J. A., Plank, T., Hauri, E. H., Kelley, K. A., Roggensack, K., & Zimmer, M. (2008). Prediction of magmatic water contents via measurement of H₂O in clinopyroxene phenocrysts. *Geology*, *36*(10), 799-802.

- Wallace, P. J. (2005). Volatiles in subduction zone magmas: concentrations and fluxes based on melt inclusion and volcanic gas data. *Journal of Volcanology and Geothermal Research*, 140(1), 217-240.
- Warren, J. M., & Hauri, E. H. (2014). Pyroxenes as tracers of mantle water variations. *Journal of Geophysical Research: Solid Earth*, 119(3), 1851-1881.
- Watson, E. B. (1994). Diffusion in volatile-bearing magmas. *Reviews in Mineralogy and Geochemistry*, 30(1), 371-411.
- Weaver, B. L. (1991). The origin of ocean island basalt end-member compositions: Trace element and isotopic constraints, *Earth Planet. Sci. Lett.*, 104, 381-397.
- White, W. M., Dupré, B., & Vidal, P. (1985). Isotope and trace element geochemistry of sediments from the Barbados Ridge-Demerara Plain region, Atlantic Ocean. *Geochimica et cosmochimica acta*, 49(9), 1875-1886.
- Woodhead, J. D. (1996). Extreme HIMU in an oceanic setting: The geochemistry of Mangaia Island (Polynesia), and temporal evolution of the Cook—Austral hotspot. *Journal of Volcanology and Geothermal Research*, 72(1-2), 1-19.
- Workman, R. K., Hauri, E., Hart, S. R., Wang, J., & Blusztajn, J. (2006). Volatile and trace elements in basaltic glasses from Samoa: Implications for water distribution in the mantle. *Earth and Planetary Science Letters*, 241(3), 932-951.
- Workman, R. K., Eiler, J. M., Hart, S. R., & Jackson, M. G. (2008). Oxygen isotopes in Samoan lavas: Confirmation of continent recycling. *Geology*, 36(7), 551-554.
- Zhao, Y. H., Ginsberg, S. B., & Kohlstedt, D. L. (2004). Solubility of hydrogen in olivine: dependence on temperature and iron content. *Contributions to Mineralogy and Petrology*, 147(2), 155-161.
- Zindler, A., Jagoutz, E., & Goldstein, S. (1982). Nd, Sr and Pb isotopic systematics in a three-component mantle: a new perspective. *Nature*, 298, 519-523.